Handbook of Magnetic Materials

Edited by

K.H.J. Buschow

VOLUME

24

Chapter 3

Advances in Magnetoelectric Materials and Their Application

L.E. Fuentes-Cobas,[1,*] J.A. Matutes-Aquino,[1] M.E. Botello-Zubiate,[1] A. González-Vázquez,[1] M.E. Fuentes-Montero[2] and D. Chateigner[3]

[1]*Advanced Materials Research Center, Chihuahua, Mexico;* [2]*Autonomous University of Chihuahua, Chihuahua, Mexico;* [3]*CRISMAT-ENSICAEN, IUT-Caen, Université de Caen Normandie, Caen, France*

**Corresponding author: E-mail: luis.fuentes@cimav.edu.mx*

Chapter Outline

Handbook of Magnetic Materials, Volume 24. http://dx.doi.org/10.1016/bs.hmm.2015.10.001

1. INTRODUCTION

The present contribution is an updated supplement to the review "Magnetoelectricity" published in Chapter 3 of Volume 19 of the series Handbook of Magnetic Materials (Fuentes-Cobas et al., 2011).

As a rule, the reader might orient himself by consulting the above review to find definitions, methods, and results. For the ease of reading, a minimum overlap with the previous article has been tolerated especially in cases where updating, generalization, or refinement is necessary.

The combined research area of magnetoelectric/multiferroic materials continues to show, as general tendency, an exponential growth. The basic science of magnetoelectricity is as charming as challenging. Particularly for single-phase magnetoelectric multiferroics, quantum theory has already provided answers to important questions, but several (old and new) open issues demand attention. Magnetoelectricity has just started to show its potentialities as a physical effect useful for applications. Currently, magnetoelectric composites lead the performance indexes and are the materials mostly used in the real world to develop practical applications.

Figure 1, based on a Scopus search, represents the behavior of the numbers of publications per year for the mentioned topics since the beginnings of the present century. Besides the general upward trend, a few details may be noteworthy.

- The time interval 2004−2010 was the takeoff moment for our materials, the occasion to grow from the order of a 100 to the vicinity of 1000 articles per year.
- During this same period, attention moved from "magnetoelectric" to "multiferroic". "Multiferroics" became a hot topic and the keyword

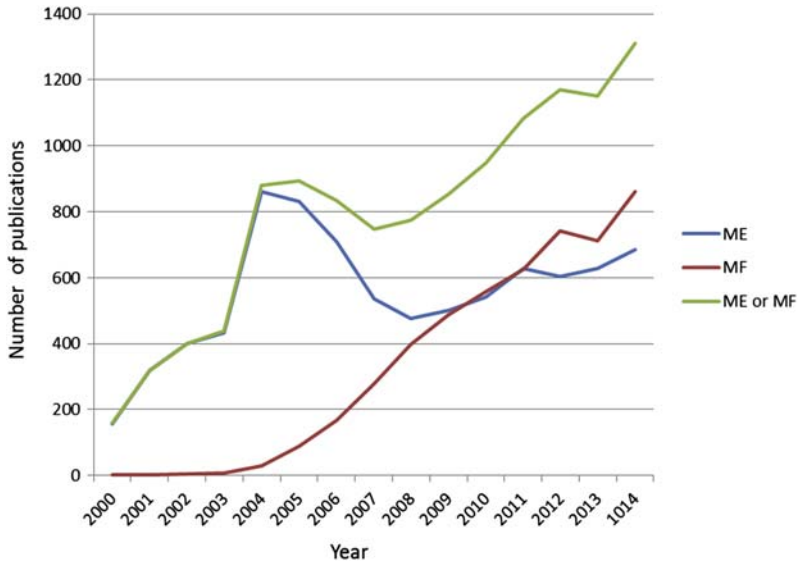

FIGURE 1 Numbers of articles published per year. ME, magnetoelectricity; MF, multiferroics. *Source: Scopus.*

"magnetoelectricity" lost popularity. Researchers searched, basically, the coexistence of ferroelectricity and ferro- (ferri-, antiferro-) magnetism. But they also required that both kinds of ordering interacted. Deeply, they also searched for significant magnetoelectricity.

- In the years 2013–2014 small reductions in the numbers of publications may be observed. A clear tendency to recovery is now apparent. These variations may be statistical fluctuations. Or maybe not. The discovery of new promising fields for applications may be awakening a new magnetoelectric era.

Figures 2 and 3, also from Scopus, represent the distributions per subject area of publications containing the keywords "application AND magnetoelectric". (A given paper may belong to more than one field, so the populations sums are higher than 100%.) Figure 2 describes the scenario during the years 2011–2013 and Figure 3 shows the situation from 2014 to present time.

The three major fields are basic physics, materials science, and engineering. Energy conversion, sensors, actuators, and information storage devices occupy a large proportion of articles in these fields. Materials science relative population is approximately constant around half of the total of published papers. Physics and astronomy, as well as engineering (considered a whole), show decrements. Last-mentioned decrease is due to emerging application fields, now identifying themselves.

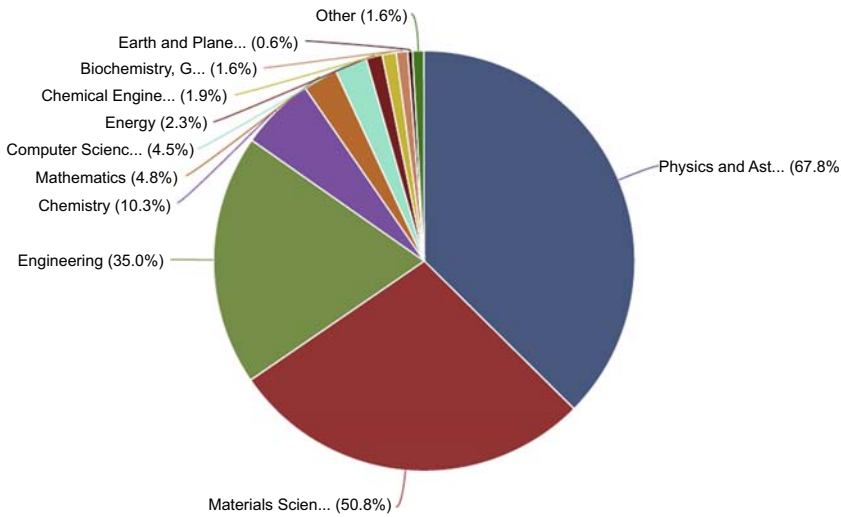

FIGURE 2 Relative population of disciplines in published papers about applications of magnetoelectricity. Time interval 2011–2013.

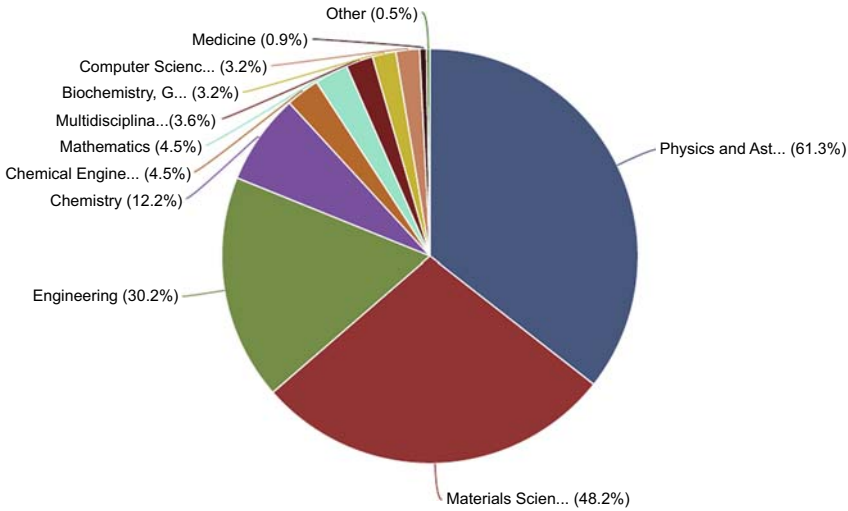

FIGURE 3 Relative population of disciplines in published papers about applications of magnetoelectricity. Time interval 2014–2015.

In Figure 3, the research fields that show significant tendencies to grow in importance are chemical engineering (1.9% → 4.5%), multidisciplinary (not considered → 3.6%), biochemistry (1.6% → 3.2%), and medicine (very small → 0.9%). One common characteristic of the rising fields is that they relate magnetoelectricity with complex systems. Recent developments on biochemistry and medicine, for example the role of magnetoelectricity in the targeted delivery of life-saving drugs, show the particular feature of being contributions with a remarkable social impact. In the Applications section of the present chapter, a brief presentation of representative findings will be given.

A number of excellent reviews on Magnetoelectric multiferroics have been published during the last few years. With pleasure we recommend the following ones Scott (2013), Kleemann and Binek (2013), Ma et al. (2011), Yoshinori et al. (2014), Bichurin and Viehland (2011), Bichurin and Petrov (2014), and Lu et al. (2015), Matsukura et al. (2015).

In the article (Fuentes-Cobas et al., 2011), Magnetoelectricity was represented as a young and gorgeous princess (awakening from a one-century sleep), with plenty of mysteries and promises. In 2015, our princess has grown from her teens and she is preparing herself to work as a Queen. She already visualizes her contributions in the utilization of relatively simple systems and now she feels attracted by challenges from highly complex objects. Who knows, maybe she finds her way to participate actively in the cure of some cancers.

2. PHYSICS OF CRYSTAL MAGNETOELECTRICITY

2.1 Summary of Constitutive Equations and Units

We summarize some fundamental relationships representing the magnetoelectric effect. A detailed treatment can be found in the earlier review mentioned above.

Electromagnetic linear and bilinear constitutive equations, SI units:

$$P_m = \varepsilon_0 \chi^P_{mn} E_n + \alpha_{mn} H_n + \gamma_{mni} H_n E_i + \frac{1}{2}\beta_{mni} H_n H_i \tag{1}$$

$$\mu_0 M_m = \mu_0 \chi^M_{mn} H_n + \alpha_{mn} E_n + \beta_{mni} E_n H_i + \frac{1}{2}\gamma_{mni} E_n E_i \tag{2}$$

The symbols have the usual meaning of texts on electromagnetism. Coefficients α_{mn} form the linear magnetoelectric (axial, 2nd rank) tensor $\boldsymbol{\alpha}$. β_{mni} and γ_{mni} are the bilinear magnetoelectric coefficients.

The SI units for α are second/meter (sm^{-1}). Single-phase magnetoelectrics usually show α values of the order of 10^{-12} sm^{-1} (ps/m). Several variants to the given definition of the magnetoelectric tensor $\boldsymbol{\alpha}$ are used.

The "practical" coefficient $\alpha^{EH} = \delta E/\delta H$, in SI, is given in VA^{-1}. Gaussian (dimensionless) and mixed ($\mathrm{V}\cdot\ \mathrm{m}^{-1}\cdot\ \mathrm{Oe}^{-1}$) units are also utilized.

The vacuum permeability μ_0 does not appear in Eqn (2) when it is written in Gaussian units (α^{Gauss}). Neither it is included in the definition variant proposed by Rivera (2009). This author suggests selecting (**E**, **B**) as independent variables, instead of (**E**, **H**).

Some conversion equations, related with $\alpha^{SI} \equiv \alpha$, are the following:

$$\alpha^{SI} = \varepsilon\alpha^{EH} = \varepsilon_0 \varepsilon^{rel} \alpha^{EH} \tag{3}$$

$$c\alpha^{SI} = \alpha^{\mathrm{Gauss}} = 4\pi\alpha^{\mathrm{Gauss-rationalized}} \tag{4}$$

c is the speed of light in vacuum.

2.2 Properties and Magnetic Symmetry

For a given crystal, the possibility and characteristics of magnetoelectric effect is determined by its crystallographic and electronic structures. In this relationship, so-called "color" or "magnetic" structural symmetry plays a decisive role. The axial nature and characteristic behavior under time inversion of magnetic magnitudes must be taken into account. A basic law to be applied is the Neumann Principle and the mathematical tool for its implementation is the Group Theory, with consideration of irreducible and complementary irreducible representations. The previous version (Fuentes-Cobas et al., 2011) of the present contribution contains detailed explanations of the mentioned concepts and methods. Below we deliver extended tables and a refined graphical

representation characterizing several electromagnetic properties. The 122 crystallographic magnetic point groups (including "grey," "classical," and "B&W" groups), as well as the 21 limiting Curie groups, are considered. Table 1A gives the properties that are allowed by symmetry according to the magnetic point group. Table 1B gives the same for the Curie limiting Groups. Table 2 presents the structure of the magnetoelectric matrices for all the considered cases. Figure 4 is a polished Venn diagram of the properties distribution among the color symmetry groups.

Data for creating Tables 1 and 2, as well as Figure 4, were obtained by consulting the following articles Newham (2005), Schmid (2008), Litvin and Janovec (2014), Borovik-Romanov and Grimmer (2003).

2.3 Magnetoelectric Longitudinal Surfaces

Tensor properties may be represented in a partial but friendly manner by their longitudinal surfaces. The distance from the coordinate origin to the magnetoelectric longitudinal surface is proportional to the longitudinal magnetoelectric modulus $\alpha(\mathbf{h})$. The relationship between $\alpha(\mathbf{h})$ and the magnetoelectric tensor α_{ij} is given by

$$\begin{aligned}\alpha(\mathbf{h}) = {} & \alpha_{11}\sin^2\phi\cos^2\beta + \alpha_{22}\sin^2\phi\sin^2\beta + \alpha_{33}\cos^2\phi \\ & + (\alpha_{12} + \alpha_{21})\sin^2\phi\cos\beta\sin\beta + (\alpha_{13} + \alpha_{31})\sin\phi\cos\phi\cos\beta \\ & + (\alpha_{23} + \alpha_{32})\sin\phi\cos\phi\sin\beta\end{aligned} \tag{5}$$

Observation direction $\mathbf{h}$ is described by its polar and azimuthal angles (ϕ, β).

$\alpha(\mathbf{h})$ represents the susceptibility of a given material to reveal *a component of electric (magnetic) polarization in the direction of an applied magnetic (electric) field*. It gives an intuitive vision of magnetoelectric anisotropy. The partial nature of $\alpha(\mathbf{h})$ resides in that it does not show the transverse component of the magnetoelectric effect.

2.4 Magnetoelectricity and the Material Properties Open Database

In the past five years researchers begun an open collection of single crystal data, for quick and free accessibility: the Material Properties Open Database, MPOD (http://mpod.cimav.edu.mx) (Pepponi et al., 2012). Measured as well as computer-simulated tensor properties are considered.

Inspired by the Crystallography Open Database COD (http://www.crystallography.net/) (Gražulis et al., 2009), MPOD aims at collecting and making publicly available, free of charge, tensor properties (including scalar properties) of phases and linking such properties to structural information of the COD when available. MPOD files are written with the STAR file syntax,

TABLE 1 Electromagnetic Properties Permitted by Symmetry (* → Property Allowed)

A) Crystallographic Magnetic Point Groups							
	Magnetic Group		PZM	FM	ME	FE	PZE
System	Schoenflies	International	Piezomag	Ferromag	Magnetoelec	Ferroelec	Piezoelec
Triclinic	C_1	*1*	*	*	*	*	*
	C_{1R}	*11′*				*	*
	C_i	*−1*	*	*			
	C_{iR}	*−11′*					
	$C_i(C_1)$	*−1′*			*		
Monoclinic	C_s	*m*	*	*	*	*	*
	C_{sR}	*m1′*				*	*
	$C_s(C_1)$	*m′*	*	*	*	*	*
	C_2	*2*	*	*	*	*	*
	C_{2R}	*21′*				*	*
	$C_2(C_1)$	*2′*	*	*	*	*	*
	C_{2h}	*2/m*	*	*			
	C_{2hR}	*2/m1′*					
	$C_{2h}(C_s)$	*2′/m*			*		
	$C_{2h}(C_2)$	*2/m′*			*		
	$C_{2h}(C_i)$	*2′/m′*	*	*			

Orthorhombic	C_{2v}	*2 mm*	*		*	*	*
	C_{2vR}	*2mm1′*				*	*
	$C_{2v}(C_s)$	*2′m′m*	*	*	*	*	*
	$C_{2v}(C_2)$	*2m′m′*	*	*	*	*	*
	D_2	*222*	*		*		*
	D_{2R}	*2221′*					*
	$D_2(C_2)$	*22′2′*	*	*	*		*
	D_{2h}	*mmm*	*				
	D_{2hR}	*mmm1′*					
	$D_{2h}(C_{2v})$	*mmm′*			*		
	$D_{2h}(D_2)$	*m′m′m′*			*		
	$D_{2h}(C_{2h})$	*mm′m′*	*	*			
Tetragonal	C_4	*4*	*	*	*	*	*
	C_{4R}	*41′*				*	*
	$C_4(C_2)$	*4′*	*		*	*	*
	S_4	*−4*	*	*	*		*
	S_{4R}	*−41′*					*
	$S_4(C_2)$	*−4′*	*		*		*
	C_{4h}	*4/m*	*	*			
	C_{4hR}	*4/m1′*					
	$C_{4h}(S_4)$	*4′/m′*			*		

Continued

TABLE 1 Electromagnetic Properties Permitted by Symmetry (* → Property Allowed)—cont'd

A) Crystallographic Magnetic Point Groups							
	Magnetic Group		PZM	FM	ME	FE	PZE
System	Schoenflies	International	Piezomag	Ferromag	Magnetoelec	Ferroelec	Piezoelec
	$C_{4h}(C_4)$	*4/m′*			*		
	$C_{4h}(C_{2h})$	*4′/m*	*				
	C_{4v}	*4 mm*	*		*	*	*
	C_{4vR}	*4mm1′*				*	*
	$C_{4v}(C_4)$	*4m′m′*	*	*	*	*	*
	$C_{4v}(C_{2v})$	*4′mm′*	*		*	*	*
	D_{2d}	*−42m*	*		*		*
	D_{2dR}	*−42m1′*					*
	D_{2d} (D_2)	*−4′2m′*	*		*		*
	$D_{2d}(C_{2v})$	*−4′2′m*	*		*		*
	$D_{2d}(S_4)$	*−42′m′*	*	*	*		*
	D_4	*422*	*		*		*
	D_{4R}	*4221′*					*
	$D_4(C_4)$	*42′2′*	*	*	*		*

	$D_4(D_2)$	*4′22′*	*		*		*
	D_{4h}	*4/mmm*	*				
	D_{4hR}	*4/mmm1′*					
	$D_{4h}(D_{2d})$	*4′/m′m′m*			*		
	$D_{4h}(C_{4v})$	*4/m′mm*			*		
	$D_{4h}(C_{4h})$	*4/mm′m′*	*	*			
	$D_{4h}(D_4)$	*4/m′m′m′*			*		
	$D_{4h}(D_{2h})$	*4′/mmm′*	*				
Trigonal	C_3	*3*	*	*	*	*	*
	C_{3R}	*31′*				*	*
	S_6	*−3*	*	*			
	S_{6R}	*−31′*					
	$S_6(C_3)$	*−3′*			*		
	C_{3v}	*3m*	*		*	*	*
	C_{3vR}	*3m1′*				*	*
	$C_{3v}(C_3)$	*3m′*	*	*	*	*	*
	D_3	*32*	*		*		*
	D_{3R}	*321′*					*
	$D_3(C_3)$	*32′*	*	*	*		*

Continued

TABLE 1 Electromagnetic Properties Permitted by Symmetry (* → Property Allowed)—cont'd

A) Crystallographic Magnetic Point Groups							
	Magnetic Group		PZM	FM	ME	FE	PZE
System	Schoenflies	International	Piezomag	Ferromag	Magnetoelec	Ferroelec	Piezoelec
	D_{3d}	$-3m$	*				
	D_{3dR}	$-3m1'$					
	$D_{3d}(S_6)$	$-3m'$	*	*			
	$D_{3d}(C_{3v})$	$-3'm$			*		
	$D_{3d}(D_3)$	$-3'm'$			*		
	C_{3h}	-6	*	*			*
	C_{3hR}	$-61'$					*
	$C_{3h}(C_3)$	$-6'$	*		*		*
Hexagonal	C_6	6	*	*	*	*	*
	C_{6R}	$61'$				*	*
	$C_6(C_3)$	$6'$	*			*	*
	C_{6h}	$6/m$	*	*			
	C_{6hR}	$6/m1'$					
	$C_{6h}(C_6)$	$6/m'$			*		
	$C_{6h}(C_{3h})$	$6'/m$					
	$C_{6h}(S_6)$	$6'/m'$	*				

	D_{3h}	$-6m2$	*				*
	D_{3hR}	$-6m21'$					*
	$D_{3h}(C_{3h})$	$-6m'2'$	*	*			*
	$D_{3h}(C_{3v})$	$-6'm2'$	*		*		*
	$D_{3h}(D_3)$	$-6'2m'$	*		*		*
	C_{6v}	$6\ mm$	*		*	*	*
	C_{6vR}	$6mm1'$				*	*
	$C_{6v}(C_6)$	$6m'm'$	*	*	*	*	*
	$C_{6v}(C_{3v})$	$6'mm'$	*			*	*
	D_6	622	*		*		*
	D_{6R}	$6221'$					*
	$D_6(C_6)$	$62'2'$	*	*	*		*
	$D_6(D_3)$	$6'22'$	*				*
	D_{6h}	$6/mmm$	*				
	D_{6hR}	$6/mmm1'$					
	$D_{6h}(C_{6v})$	$6/m'mm$			*		
	$D_{6h}(C_{6h})$	$6/mm'm'$	*	*			
	$D_{6h}(D_6)$	$6/m'm'm'$			*		
	$D_{6h}(D_{3h})$	$6'/mmm'$					
	$D_{6h}(D_{3d})$	$6'/m'mm'$	*				

Continued

TABLE 1 Electromagnetic Properties Permitted by Symmetry (* → Property Allowed)—cont'd

A) Crystallographic Magnetic Point Groups							
	Magnetic Group		PZM	FM	ME	FE	PZE
System	Schoenflies	International	Piezomag	Ferromag	Magnetoelec	Ferroelec	Piezoelec
Cubic	T	*23*	*		*		*
	T_R	*231′*					*
	T_h	*m-3*	*				
	T_{hR}	*m-31′*					
	$T_h(T)$	*m′−3′*			*		
	T_d	*−43m*					*
	T_{dR}	*−43m1′*					*
	$T_d(T)$	*−4′3m′*	*		*		*
	O	*432*			*		
	O_R	*4321′*					
	O(T)	*4′32′*	*				
	O_h	*m−3m*					
	O_{hR}	*m−3m1′*					
	$O_h(O)$	*m′−3′m′*			*		

	$O_h(T_h)$	$m-3m'$	*				
	$O_h(T_d)$	$m'-3'm$					
Total	122		66	31	58	31	66
			PZM	FM	ME	FE	PZE

B) Curie Limiting Magnetic Point Groups

Limiting Group	PZM	FM	ME	FE	PZE
$\infty\infty m$					
$\infty\infty m1'$					
$\infty\infty m'$			*		
∞/mm					
$\infty/mm1'$					
$\infty/m'm$			*		
∞/mm'	*	*			
$\infty/m'm'$			*		
∞m				*	*
$\infty m1'$				*	*
$\infty m'$		*	*	*	*
$\infty 2$	*		*		*
$\infty 21'$					*

Continued

TABLE 1 Electromagnetic Properties Permitted by Symmetry (* → Property Allowed)—cont'd

B) Curie Limiting Magnetic Point Groups					
Limiting Group	**PZM**	**FM**	**ME**	**FE**	**PZE**
$\infty 2'$	*	*	*		*
$\infty \infty$			*		
$\infty \infty 1'$					
∞/m	*	*			
$\infty/m1'$					
∞/m'			*		
∞	*	*	*	*	*
$\infty 1'$				*	*
Total	5	5	9	5	8

TABLE 2 Magnetoelectric Matrices for Crystallographic and Curie Limiting Magnetic Point Groups

1, −1′	$\begin{bmatrix} \alpha_{11} & \alpha_{12} & \alpha_{13} \\ \alpha_{21} & \alpha_{22} & \alpha_{23} \\ \alpha_{31} & \alpha_{32} & \alpha_{33} \end{bmatrix}$
2, m′, 2/m′	$\begin{bmatrix} \alpha_{11} & 0 & \alpha_{13} \\ 0 & \alpha_{22} & 0 \\ \alpha_{31} & 0 & \alpha_{33} \end{bmatrix}$
2′, m, 2′/m	$\begin{bmatrix} 0 & \alpha_{12} & 0 \\ \alpha_{21} & 0 & \alpha_{23} \\ 0 & \alpha_{32} & 0 \end{bmatrix}$
222, 2m′m′, m′m′m′	$\begin{bmatrix} \alpha_{11} & 0 & 0 \\ 0 & \alpha_{22} & 0 \\ 0 & 0 & \alpha_{33} \end{bmatrix}$
2′2′2, mm2, 2′mm′, mmm′	$\begin{bmatrix} 0 & \alpha_{12} & 0 \\ \alpha_{21} & 0 & 0 \\ 0 & 0 & 0 \end{bmatrix}$
3, −3′, 4, −4′, 4/m′, 6, −6′, 6/m′, ∞, ∞/m′	$\begin{bmatrix} \alpha_{11} & \alpha_{12} & 0 \\ -\alpha_{12} & \alpha_{11} & 0 \\ 0 & 0 & \alpha_{33} \end{bmatrix}$
4′, −4, 4′/m′	$\begin{bmatrix} \alpha_{11} & \alpha_{12} & 0 \\ \alpha_{12} & -\alpha_{11} & 0 \\ 0 & 0 & 0 \end{bmatrix}$
32, 3m′, −3′m′, 422, 4 mm′, −4′2m′, 4/m′m′m′, 622, 6m′m′, −6′m′2, 6/m′m′m′, ∞2, ∞/m′m′, ∞m′	$\begin{bmatrix} \alpha_{11} & 0 & 0 \\ 0 & \alpha_{11} & 0 \\ 0 & 0 & \alpha_{33} \end{bmatrix}$
4′22, 4′mm′, −42m, −42′m′, 4′/m′mm′	$\begin{bmatrix} \alpha_{11} & 0 & 0 \\ 0 & -\alpha_{11} & 0 \\ 0 & 0 & 0 \end{bmatrix}$
32′, 3m, −3′m, 42′2′, 4mm, −4′2′m, 4/m′mm, 62′2′, 6mm, −6′m2′, 6/m′mm, ∞2, ∞/m′m′, ∞m′	$\begin{bmatrix} 0 & \alpha_{12} & 0 \\ -\alpha_{12} & 0 & 0 \\ 0 & 0 & 0 \end{bmatrix}$
23, m′3, 432, −4′3m′, m′3m′, 32, 3m′, −3′m′, 422, 4 mm′, −4′2m′, 4/m′m′m′, 622, 6m′m′, −6′m′2, 6/m′m′, ∞∞, ∞∞m′	$\begin{bmatrix} \alpha_{11} & 0 & 0 \\ 0 & \alpha_{11} & 0 \\ 0 & 0 & \alpha_{11} \end{bmatrix}$

used and developed for the Crystallographic Information Files CIF (Hall et al., 1991). A dictionary containing all tensors definitions has been written according to the Dictionary Definition Language. The data set in constant evolvement includes elastic stiffness and compliance, internal friction, electrical resistivity, dielectric permittivity and stiffness, heat capacity, thermal

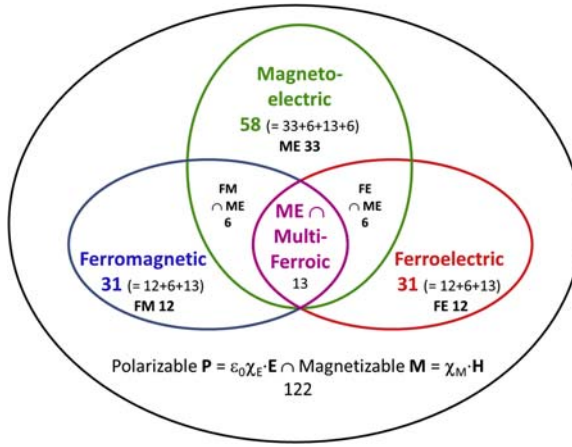

FIGURE 4 Venn diagram for electromagnetic properties of insulator materials. Under a magnetic field, any material is magnetizable. Under an electric field, a conductor (or semiconductor) is harbor of electric currents; an insulator is polarizable. Magnetoelectrics show direct and coupling effects. All electromagnetic multiferroics (ferroelectric ∩ ferromagnetic) are magnetoelectric.

conductivity, diffusivity and expansion, piezoelectricity, electrostriction, electromechanical coupling, optic indexes; piezooptic, photoelastic superconducting critical fields, penetration and coherence lengths, and magnetoelectric properties (see http://mpod.cimav.edu.mx/data/properties/ for a complete list). Properties are reported in MPOD files where the original published paper containing the data is cited and structural and experimental information is also given. One MPOD file contains information relative to only one publication and one phase.

Recent advances have been the implementation of online 3D plots of tensor longitudinal surfaces, and their exports of files usable in 3D printers (Fuentes-Cobas et al., 2014).

Although the MPOD database still remains skewed toward polar (dielectric, piezoelectric, elastic and so on) tensors, some ME tensors are already included, which we use as examples here:

Equations (6) and (7) show the ME tensors for Cr_2O_3 at 4.2 and 270 K, respectively. Values are in ps/m:

$$\propto = \begin{bmatrix} 0.73 & 0 & 0 \\ 0 & 0.73 & 0 \\ 0 & 0 & 0.23 \end{bmatrix} \quad (Cr_2O_3, \ T = 4.2 \ K) \tag{6}$$

$$\propto = \begin{bmatrix} 0.73 & 0 & 0 \\ 0 & 0.73 & 0 \\ 0 & 0 & 4.14 \end{bmatrix} \quad (Cr_2O_3, \ T = 270 \ K) \tag{7}$$

Cr_2O_3 adopts the -3′m′ (D_{3d}:D_3) magnetic point group symmetry under low static magnetic fields. It can be seen that α_{33} strongly increases with

temperature from helium to near room temperature (Wiegelmann et al., 1994), while α_{11} remains practically constant in this temperature range. Because of the symmetry, no anisotropy is present perpendicular to the three axis (c-axis of the crystal indexed in the hexagonal lattice). A large c-axis component develops at larger temperatures, clearly visible as a strong lobe in the longitudinal surface. In order to benefit from stronger ME effects in this phase, the c-axes of the crystals have to be used at larger temperatures, while a perpendicular direction should be favored for lower temperatures. From the point of view of the Neumann Principle, this is a case where the property's symmetry (axial) is higher than that of the structure (rhombohedral) (Figure 5).

Next we consider $LiCoPO_4$. According to (Rivera, 1994), single crystals of $LiCoPO_4$ at 4.2 K show magnetic point group mmm′ (D_{2h}:C_{2v}). Due to the off-diagonal type of the ME tensor, Eqn (8), the axial symmetry of the ME effect along the c-axis is lost (Figure 6). ME effect in this case is mostly transverse. The maximum ME effect appears in the **b**-axis under an excitation along the

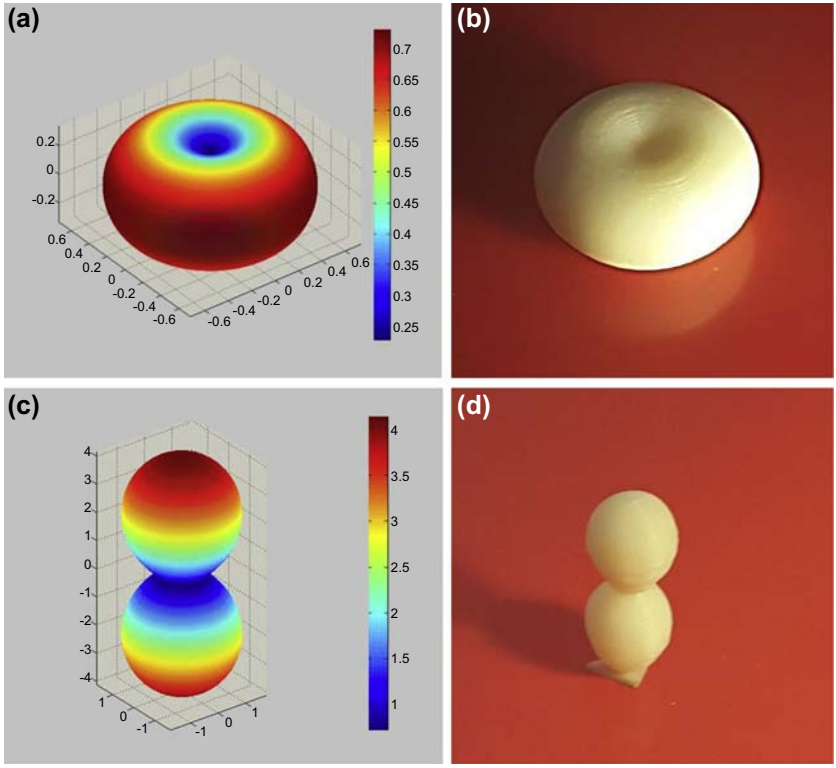

FIGURE 5 Magnetoelectricity in Cr_2O_3 under low magnetic field. (a) and (b) longitudinal ME surfaces at 4.2 K (computer display and 3D printing); (c) and (d) corresponding figures at 270 K.

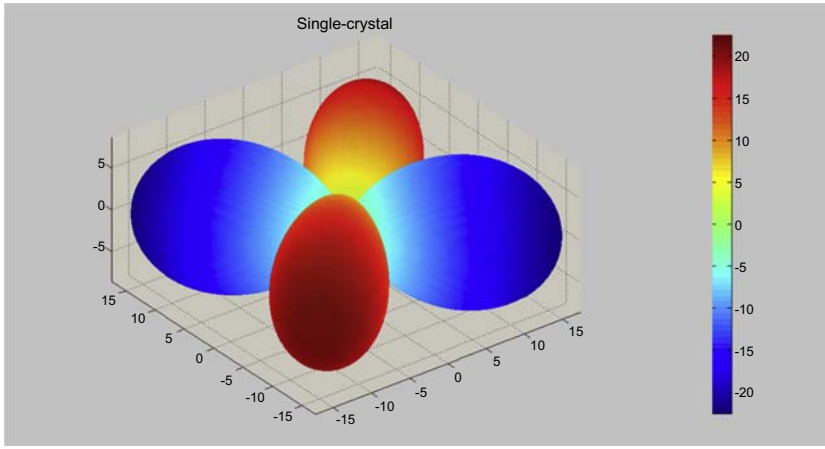

FIGURE 6 $LiCoPO_4$ Single crystal ME longitudinal surface. An interesting "detail": The two vertical planes of ordinary symmetry (0, *y*, *z*) and (*x*, 0, *z*) invert the sign of $\alpha(\mathbf{h})$ while the horizontal plane of antisymmetry (*x*, *y*, 0) does not. That is the curious manner how axial magnitudes and magnetic symmetry work.

a-axis. The maximum components of the longitudinal effect are aligned with the diagonals of the (*a, b*) planes of the crystals.

$$\propto = \begin{bmatrix} 0 & 18.4 & 0 \\ 30.6 & 0 & 0 \\ 0 & 0 & 0 \end{bmatrix} \text{ps/m} \quad (LiCoPO_4, \ T = 4.2 \ \text{K}) \tag{8}$$

Our last MPOD example is $K_2[FeCl_5(H_2O)]$, with data from (Ackermann et al., 2014). The tensor matrix is Eqn (9) and the longitudinal surface is Figure 7. The magnetic point group is m′m′m′, so the property surface is reflected in the antisymmetry planes (0, *y*, *z*), (*x*, 0, *z*), and (*x*, *y*, 0). The ME effect shows a very low value along the **b**-axis, typically 10 times lower than along **a** and **c**. The mentioned features are clearly revealed on the representative surface.

$$\propto = \begin{bmatrix} 0.71 & 0 & 0 \\ 0 & 0.08 & 0 \\ 0 & 0 & 1.17 \end{bmatrix} \tag{9}$$

2.5 Superexchange Interaction

Many oxides are insulators, where electrons are localized. In insulating transition-metal oxides there is little, if any, direct 3d−3d overlap; however, the

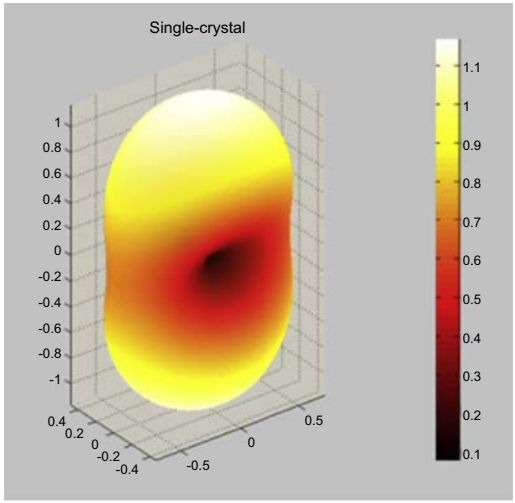

FIGURE 7 ME longitudinal surface of $K_2FeCl_5H_2O$ at 11 K. MPOD graphic output. Values in ps/m.

3d-orbitals are hybridized with the oxygen 2p-orbitals: $\varphi_{3d} = \alpha\psi_{3d} + \beta\psi_{2p}$ with $|\alpha|^2 + |\beta|^2 = 1$, where φ_{3d} is the hybridized orbital, and α and β are coefficients expressing the 3d and 2p contributions, respectively. The superexchange interaction, between magnetic ions, is transmitted via the oxygen bridges, and it can be described by the Heisenberg Hamiltonian. Figure 8 shows a typical superexchange bond, where for the case of a singly occupied 3d-orbital or a half-filled d shell (Fe^{3+}, Mn^{2+}), the configuration (b) is lower in energy than configuration (a) because both electrons in an oxygen 2p-orbital

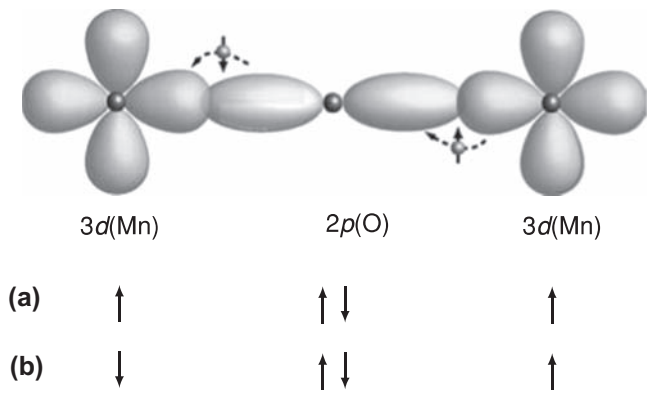

FIGURE 8 A typical superexchange bond. Configuration (b) is lower in energy than configuration (a). *Reprinted with permission from Coey (2009),* Magnetism and Magnetic Materials, *Copyright 2009 Cambridge University Press.*

can then spread out into unoccupied 3d-orbitals. The superexchange interaction, J, involves a simultaneous virtual transfer of two electrons with the instantaneous formation of a $3d^{n+1}2p^5$ excited state; the interaction is of order $2t^2/U$, where t is the so-called p−d transfer integral and U is the onsite 3d Coulomb interaction. The transfer integral is of order 0.1 eV and the onsite Coulomb interaction is in the range 3−5 eV. J depends sensitively on the interatomic separation, but also on the M−O−M bond angle, varying as $\cos^2\theta_{12}$. The critical factors in determining the strength and sign of superexchange are the occupancy and the orbital degeneracy of the 3d states. There are many possible cases of superexchange interactions to consider, and the results were summarized in the Goodenough−Kanamori rules, which were reformulated by Anderson, in a simpler way that makes it unnecessary to consider the oxygen. Superexchange interaction is more commonly antiferromagnetic than ferromagnetic, because the overlap integrals are more likely to be larger than zero (Coey, 2009).

2.6 Ferroelectricty in Spiral Magnets

The mechanisms that give rise to cross-coupling between polarization and magnetization are very similar to those that lead to the linear magnetoelectric effect. On a phenomenological level, this coupling is determined solely by symmetry arguments. In particular, spatial inversion reverses the sign of electric polarization P, while magnetization M is left unchanged. Time reversal, in turn, will reverse the sign of M, while the sign of P remains unaffected. This topic is explained in detail in Fuentes-Cobas et al. (2011).

The fourth-order coupling proportional to P^2M^2 is generally allowed by symmetry. It gives rise to small anomalies in dielectric constants at the magnetic transition, as this fourth-order term is typically rather weak. On the contrary, third-order couplings of the form $PM\partial M$ can have interesting consequences. The third order coupling is linear in P and since it contains a single spatial derivative, it is called Lifshitz invariant. The inhomogeneous coupling allows for two scenarios depending on whether ferroelectric or magnetic order occurs first in the material. If ferroelectricity occurs first, this term favors an incommensuration of a magnetic ordering. $BiFeO_3$, for example, is an antiferromagnetic ferroelectric with a Néel temperature of $\sim$643 K and a ferroelectric Curie temperature of $\sim$1103 K. It is a very rare example of a multiferroic with both magnetic and ferroelectric ordering temperatures above room temperature. The primary magnetic order in $BiFeO_3$ is G-type antiferromagnetism, but, in addition, it has been reported that bulk single crystals exhibit a superimposed cycloidal spiral magnetic ordering. Due to the relativistic origin of the Lifshitz invariant $-\lambda PL\partial L$, that couples the Néel vector L and the polarization P, the period of rotation is very long, namely $\lambda = 620$ Å. If an inhomogeneous magnetic ordering sets in first, then a Lifshitz term in the free energy can induce polarization (Vegte, 2010).

What kind of magnetic order can induce polarization? For example, the sinusoidal ordering, described by $\vec{M}_n = M_0 \vec{e}_1 \cos(\vec{Q} \cdot \vec{x}_n)$ where $\vec{e}_1$ is a unit vector and $\vec{Q}$ is the wave vector of the spiral, cannot give rise to polarization. This can be seen by substituting this expression in the free energy that describes the coupling between polarization and a nonuniform distribution of magnetization in a cubic environment. On the contrary, a spiral magnetic state, described by $\vec{M}_n = M_0[\vec{e}_1 \cos(\vec{Q} \cdot \vec{x}_n) + \vec{e}_2 \sin(\vec{Q} \cdot \vec{x}_n)]$, gives rise to polarization, and the induced electric polarization is orthogonal to the propagation vector and lies in the spiral plane (Vegte, 2010).

2.7 Dzyaloshinskii–Moriya (DM) Interaction

A special category of magnetic structures consists of those in which the periods of the "magnetic lattice" are incommensurate with the periods of the original crystal lattice. Various mechanisms are possible for the formation of such structures; here we shall present the mechanism considered by Landau (2009).

A few materials with low symmetry exhibit a weak antisymmetric coupling, the Dzyaloshinskii–Moriya (DM) interaction (Dzyaloshinskii, 1958, 1964; Moriya, 1960). This is a higher-order effect, occurring between ions already coupled by superexchange; $|D/J| \approx 10^{-2}$. In an antiferromagnet, the spins may be canted away from the antiferromagnetic axis by about 1°. Antisymmetric exchange is the reason why antiferromagnets with a uniaxial crystal structure such as MnF_2, $MnCO_3$, and α-Fe_2O_3 may exhibit a weak ferromagnetic moment. In the older literature, the term parasitic ferromagnetism is encountered for this kind of intrinsic weak ferromagnetism, because it was thought to be due to ferromagnetic impurities. A moment only appears when the antiferromagnetic axis is perpendicular to the crystallographic axis of symmetry, along which D is constrained to lie. It disappears when the axes are parallel (Coey, 2009).

The antisymmetric DM interaction is also the microscopic mechanism involving magnetically induced ionic displacements in spiral ferroelectrics. The DM interaction resembles the form of antisymmetric superexchange interaction that appears in addition to the symmetric Heisenberg exchange, $(\vec{S}_i \times \vec{S}_j)$, due to relativistic spin–orbit coupling. The DM interaction is expressed by

$$H_{DM} = \sum_{ij} \vec{D}_{ij} \cdot \left(\vec{S}_i \times \vec{S}_j \right) \tag{10}$$

$\vec{D}_{ij} \propto \lambda \vec{x} \times \vec{r}_{ij}$ is the so-called Dzyaloshinskii-vector, where $\vec{r}_{ij}$ is the unit vector connecting the magnetic ions i and j, and $\vec{x}$ is the distance between the ligand (mostly oxygen) mediating the superexchange and this line as can be seen in Figure 9. Here λ is the spin–orbit coupling constant. To some

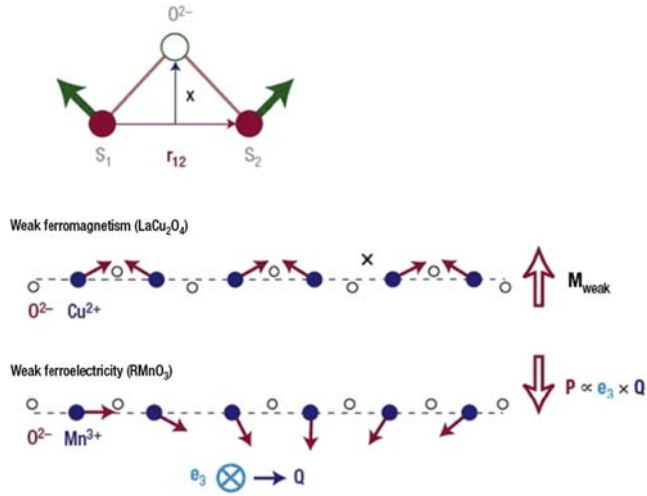

FIGURE 9 Effects of the antisymmetric Dzyaloshinskii–Moriya interaction. The interaction $H_{DM} = \mathbf{D}_{12} \cdot (\mathbf{S}_1 \times \mathbf{S}_2)$. The Dzyaloshinskii vector $\mathbf{D}_{12}$ is proportional to spin–orbit coupling constant λ, and depends on the position of the oxygen ion (open circle) between two magnetic transition metal ions (filled circles), $\mathbf{D}_{12} \propto \lambda \mathbf{x} \times \mathbf{r}_{12}$. Weak ferromagnetism in antiferromagnets (e.g., $LaCu_2O_4$ layers) results from the alternating Dzyaloshinskii vector, whereas (weak) ferroelectricity can be induced by the exchange striction in a magnetic spiral state, which pushes negative oxygen ions in one direction transverse to the spin chain formed by positive transition metal ions. *Reprinted with permission from Macmillan Publishers Ltd: Nature Materials (Cheong and Mostovoy, 2007), Copyright 2007.*

extent, the further away is the ligand from the axis connecting the magnetic ions, the larger is the DM interaction. Being proportional to the vector product of spins, the DM interaction favors non-collinear spin ordering (Vegte, 2010).

The DM interaction leads to several phenomena. For example, a common feature of antiferromagnetic oxides, including the parent compound of high-temperature superconductors La_2CuO_4, is the presence of canted spins on the transition metal sublattice. With the help of the schematic picture shown in Figure 9 we can easily explain how such a weak ferromagnetism arises from the DM interaction (Cheong and Mostovoy, 2007).

Consider a chain of Cu^{2+} spins with nearest-neighbor interactions arising from superexchange interactions via intermediate oxygen ions. The oxygen ions are distorted from the plane formed by the Cu ions, forming a buckled sheet, which results in an alternating Dzyaloshinskii-vector. As a consequence, the low-temperature spin arrangement corresponds to canted antiferromagnet order rather than a pure Néel state. At the same time, the inverse Dzyaloshinskii–Moriya mechanism can give rise to ferroelectricity in spiral magnets such as $RMnO_3$. For the spiral spin structure $\vec{M}_n = M_0[\vec{e}_1 \cos(\vec{Q} \cdot \vec{x}_n) + \vec{e}_2 \sin(\vec{Q} \cdot \vec{x}_n)]$, the vector product $(\vec{S}_i \times \vec{S}_j)$ is equal for each pair of spins. Therefore, the DM

interaction pushes the O^{2-} in one direction transverse to the chain of magnetic ions, as a result of which electric polarization is induced.

2.8 A Note on the Modern Theory of Polarization

A particular concept that has regained focus in the representation of multiferroicity is that of *electric polarization*. In a qualitative description, the polarization of a classic ferroelectric, say $BaTiO_3$, is easy to understand if one follows the schematic transformation shown in Figure 10. This figure shows the transition from the nonpolar centrosymmetric structure of $BaTiO_3$ to its tetragonal non-centrosymmetric ferroelectric phase. From simple symmetry considerations, one can ascertain that the opposite shifts of the Ti cations with respect to those of the O anions lead to a global polarization.

The quantitative treatment of this subject, on the other hand, is not as intuitive. The concept of electric dipole moment *of a molecule* is widely used and can be defined as: $\mathbf{p} = \Sigma q_i \mathbf{r}_i$. On the other hand, for *a periodic array of atoms or ions* (multiferroic crystals included), there is no way to consider the material as a single molecule.

The problems start when one asks: Where would you consider the structure starts and ends? Does the polarization depend on the boundaries, or is there certain magnitude owed to the atomic structure of the material itself? It is common, for example, to evaluate the magnitude of certain property in a unit cell and dividing it by its volume. Shouldn't it be defined a quantity that was computed per volume unit or per weight, for the polarization as well?

The difficulty of describing the polarization of a periodic solid is described in classic books like the one by Purcell and Morin (2013). We summarize it, following the explanation given by Spaldin (2012), by examining the one-dimensional case depicted in Figure 11.

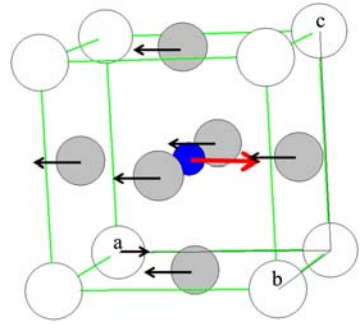

FIGURE 10 Structure of cubic perovskite compounds, such as $BaTiO_3$. Atoms Ba, Ti, and O are represented by gray, dark blue (dark gray in print versions), and white circles, respectively. The vectors indicate the magnitudes of the displacements in a polarized state along **x**.

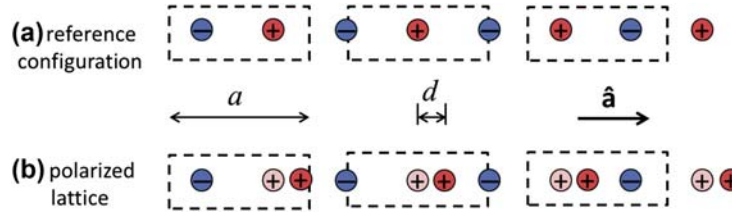

FIGURE 11 (a) One-dimensional chain of alternating anions and cations, spaced a distance $a/2$ apart. a is the lattice constant and $\hat{\mathbf{a}}$ is a unit vector. The dashed lines indicate three representative unit cells that are equally valid for calculating the polarization. (b) Under the action of an electric field, the cations are shifted distances d to the right. Cation initial positions are colored pink. The dipole moment change is the same in all cells.

In Figure 11(a) the contribution of the cations from the linear lattice to the polarization depends on the chosen unit cell. By simple inspection, one can assert that the dipole moments of the left and right rectangles are of the same magnitude and opposite directions. The left rectangle has a moment per unit length of $\mathbf{p} = \Sigma q_i \mathbf{r}_i / a = q \cdot \hat{\mathbf{a}}/2$ and the cell at the right has a moment per unit length of $-q \cdot \hat{\mathbf{a}}/2$. The central rectangle has a zero polarization due to its centrosymmetricity.

This paradox is addressed by the so-called *Modern Theory of Polarization*, the basic concepts of which are presented below.

Let us first go to the macroscopic experimental world and revisit the classical Sawyer–Tower (ST) method for polarization measurement (Figure 12).

The basic idea of the ST method is simple. A series circuit with the sample under observation (capacitor C_E) and a reference capacitor ($C_0 >> C_E$) is activated by an AC power supply. The X and Y inputs of a measuring oscilloscope are respectively the voltages on the ferroelectric sample V_E and on the reference capacitor V_P. V_E is proportional to the electric field intensity on the ferroelectric, and $V_P = Q/C_0$ is a measurement of the polarization in the ferroelectric. Q is the free charge in C_0, numerically equal to that in C_E. According to electrostatics, the surface charge density $\sigma = \text{charge/area} = Q/A = C_0 V_P/A$ equals the polarization density of the investigated ferroelectric. This way, measuring V_P leads to knowledge of the ferroelectric polarization condition. This experimental observation, performed on an AC circuit, does not give absolute values of the polarization, but the amplitudes of the alternating variations of this is observable. On the other hand, The ST method is free from the ambiguities of the mentioned "molecular dipoles" representation.

Now back to the microscopic word. Figure 11(b) represents the relative shift of the ions under the action of an electric field. For simplicity, the anions are considered as fixed and all the displacements are associated with the cations. If the cations move a distance d the change in polarization per unit of

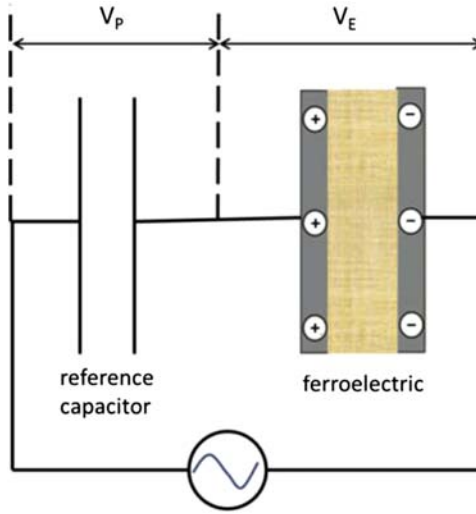

FIGURE 12 Scheme of the Sawyer–Tower method for measuring ferroelectric polarization. The electric charges in the capacitor containing the ferroelectric represent the polarizing condition of Figure 2(b).

length is $\delta\mathbf{p} = d\cdot\hat{\mathbf{a}}/a$. If the electric field is inverted, the cations reverse their displacements and the dipoles variations change to $\delta\mathbf{p} = -d\hat{\mathbf{a}}/a$. These contributions to the material polarization, associated to the movements of the ions, are independent of the cell choice and are properly comparable with the experimental results from an ST measurement.

A more exact microscopic description of polarization requires consideration of the contribution from the valence electrons. Here, again the periodical nature of crystals requires careful analysis. Consider the following. In the same linear lattice from Figure 11(a), let a collective transfer of one valence electron between all horizontal anions occur. In that case, an anion from the left—for example— becomes neutral and his neighboring anion, which is at a distance of a at his right, remains charged with the same charge as before the shift. Of course, because of the periodicity condition, the same has happened to the rest of the anions. This will bring a change in the dipole moment of magnitude $electron\ charge\cdot distance = -\mathrm{e}\cdot a$. per unit length and adopting the electronic charge as unitary, the change in dipole linear density is $-a/a = -1$.

If this same hypothetical experiment is performed several times, one comes to the conclusion that the polarization can change an entire number of times in both directions. Nevertheless, the change in polarization from shifting an electron a distance a is always -1. This quantity is called "the polarization quantum" (P_q).

The bulk polarization resulting from the part associated with the off-center movement of the ions and the electronic contribution, the change of total

polarization between two opposite configurations, is the one that can be compared with the experiment.

The *Modern Theory of Polarization* allows the computation of the quantities corresponding to three dimensions. For the explanation of the exact methodology, we refer to the original articles Van Aken et al. (2004), Resta (1993), Vanderbilt and King-Smith (1993) and to the excellent review by Resta and Vanderbilt (2007). The central quantities in the mentioned theory are the ionic and electronic contributions to the polarization. According to the preceding discussion, they are defined modulo the polarization quantum P_q:

$$\boldsymbol{p} = \frac{1}{\Omega}\sum i(q_i \boldsymbol{x}_i)^{\text{ions}} + \frac{1}{\Omega}\sum_n (q_n \overline{r}_n)^{WF} \tag{11}$$

The first term is associated to the ion shifts and the second one to the electronic contribution (the sum is referred to the occupied electronic states only). $\overline{r}_n$ is the so-called Wannier centers, which represent the average position of the electrons using localized Wannier orbitals (Marzari and Vanderbilt, 1997) and Ω is the volume of the chosen cell.

The polarization thus defined has a direct and predictive relationship to the surface charge which accumulates at the electrodes in Figure 3, independently from the choice of ionic basis.

2.9 Magnetoelectricity and the Electron Electric Dipole

One hot topic in particle physics is that of the electric dipole moment of the electron. Measuring a non-null value for this magnitude would imply a violation of the time-reversal symmetry and consequently charge-parity (CP) violation in the universe would also be demonstrated. Mentioned issues are related with the validation of the standard model and with the explanation of the observed matter–antimatter asymmetry. One line of research recently initiated in the stated problem has its basis in the analogy of underlying physics with the magnetoelectric effect.

Figure 13 (Rushchanskii et al., 2010) describes schematically the fundamentals of an experiment for the search of the electron electric dipole moment.

Up to the time of this writing, performed experiments define an upper limit for the EDM of 6.05×10^{-25} *e*cm (Eckel et al., 2012).

3. REPRESENTATIVE MAGNETOELECTRIC CRYSTALS

3.1 $BiFeO_3$ and Related Perovskites

In recent decades, the bismuth ferrite $BiFeO_3$, also known as BFO, has received a great deal of attention. BFO is the only single-phase material that presents a multiferroic behavior at room temperature. Its Curie temperature is 1093 K and its Neel temperature is 643 K (Petit, 2013). Every year,

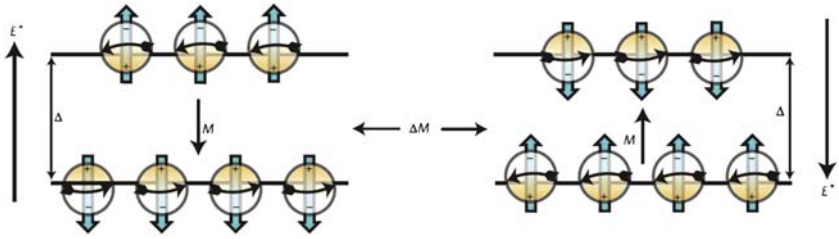

FIGURE 13 Schematic of the physics underlying the experiment to search for the electron electric dipole moment (EDM). The energy of electrons with EDMs parallel to the effective electric field E_{-} is lower than that for electrons with antiparallel EDMs by an amount $\Delta E = E^{*} \cdot d_e$. As a result, there is a population imbalance and, as the magnetic moments are oriented along the EDM directions, a corresponding net magnetization, M. When the electric field is reversed there is a magnetization reversal, ΔM, which can be detected using a sensitive magnetometer. *Reprinted by permission from Macmillan Publishers Ltd: Nature Materials (Rushchanskii et al., 2010). Copyright 2010.*

thousands of articles related with BFO are published worldwide. A recent review by Ramesh (2014) delivers a vivid story of BFO's present and future perspectives. Fresh points of view regarding peculiarities of the Dzyaloshinskii−Moriya interaction in BFO have been motivated by interesting experiments showing a negative magnetostrictive magnetoelectric coupling in BFO (Lee et al., 2013).

The structure of BFO is characterized by two distorted perovskite unit cells (Figure 14) which are connected along its main diagonal, denoted by the pseudocubic <111> direction to form a rhombohedral R3c unit cell (Reyes et al., 2007).

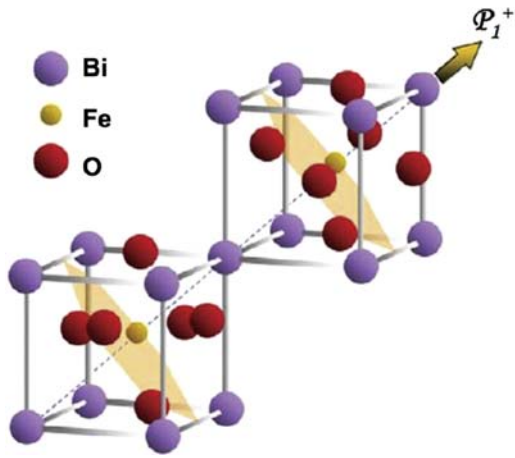

FIGURE 14 Structure, magnetization planes, and polarization direction of $BiFeO_3$. *Reprinted from Chu et al. (2007). Copyright 2007, with permission from Elsevier.*

The ferroelectric behavior of $BiFeO_3$ comes from the 6s electron pair of bismuth, while the magnetic behavior arises from the partially filled *d* orbital of iron atoms.

The Bi^{3+} ion has six electrons in the valence shell, thus covalent bonds with oxygen ions occur. The 6sp hybrid bond orbital of bismuth with oxygen is the one that generates the mentioned 6s pairs. These pairs are isolated and shifted off center, resulting in a spontaneous polarization, while the superexchange interaction between Fe^{3+} ions accounts for the magnetic behavior.

Leakage currents in BFO limit its applicability. These currents are generated by impurity phases, multiple valence states of iron ions, and oxygen vacancies. For example, $Bi_2Fe_4O_9$, $Bi_{25}FeO_{40}$, Bi_2O_3, Fe_2O_3 secondary phases are frequently generated. Cited problems can be solved by introducing dopants into the sites A and B (Rojas-George et al., 2015; Silva et al., 2011, 2012).

To obtain pure phases, trivalent lanthanides such as La^{3+}, Nd^{3+}, Gd^{3+}, Pr^{3+}, Sm^{3+}, and divalent cations (Sr^{2+}, Pb^{2+}, Ba^{2+}) can be used as dopants (Jaffari et al., 2015) When doping with La^{+3} y Pb^{+2}, the formation of a secondary phase is suppressed. Particularly, when doping with Pb^{2+}, there is a tendency to an arrangement from an R3c structure to a cubic Pm-3m; while doping with La^{+3} does not affect the space group. This difference is due to the differences in the ionic radii of Pb^{2+} and Bi^{3+}.

When introducing titanium in site B, the tendency to form a rhombohedral crystal phase increases. The Ti^{4+} has a higher oxidation state than Fe^{+3}, thus the substitution at these sites reduces the concentration of oxygen vacancies and hence its conductivity.

With respect to magnetic properties, BFO exhibits a type G antiferromagnetic behavior, plus a small net magnetization resulting from the Dzyaloshinskii−Moriya interaction (Chu et al., 2007).

Doping with Ti has resulted in disruption of the antiferromagnetic structure, leading to a larger overall magnetic moment. Cobalt has also been used to destroy the antiferromagnetic order. This is due to the hypothesis of an increment in magnetization from the superexchange interaction in the row of ions Fe^{+3}−O^{-2}−Co^{+3}. According to Sui et al. (2015) the R3c structure remains unchanged and ferromagnetic until an atomic cobalt concentration of 0.2.

Table 3 summarizes the magnetic properties of representative doped BFOs.

The physical issues related with the magnetoelectric nature of BFO are not exhausted. A recent single crystal neutron diffraction study of $BiFeO_3$ (Lee et al., 2013) leads to an alternative microscopic model for the magnetically induced electric polarization of this key material. Figure 15 shows the BFO structure, as observed by a neutron diffraction analysis. The most important finding in the experiment by Lee et al. (2013) is that the magnetostrictive coupling suppresses the electric polarization at the Fe site below the Neel temperature.

Figure 16 compares different models that were applied to explain the relationship between the electric polarization and the intensity of a

TABLE 3 Effect of Selected Dopants on BFO

Dopant	Effect on Properties	References
Pure BFO	Slightly canted antiferromagnetic	Lebeugle et al. (2008)
Sr^{2+}	Magnetization enhanced by modification of the spin spiral	Naik and Mahendiran (2009)
Ba^{+2}		
Sr^{2+}– Ba^{2+}		
Co^{+3}	Magnetically induced increase of polarization and dielectric constant	Sui et al. (2015)
Pb^{+2}	Volatilization and leakage current control	Jaffari et al. (2015)
La^{+3}– Pb^{+2}	Stabilization of the crystal structure	
Ti^{+4}	Increase of the magnetic coercitivity and remnant magnetization	

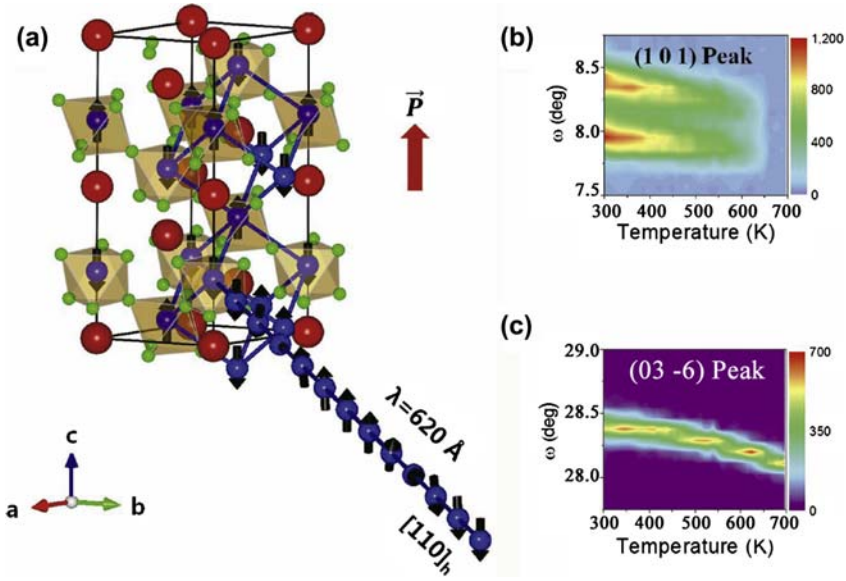

FIGURE 15 (a) Cycloid magnetic structure of $BiFeO_3$ with the propagation vector Q along the [110] direction. In this hexagonal setting, the total ferroelectric polarization (P) is pointing along the c-axis. (b) and (c) show the temperature dependence of magnetic (101) and nuclear (03−6) Bragg peaks. *Reprinted with permission from Lee et al. (2013). Copyright 2013 by the American Physical Society.*

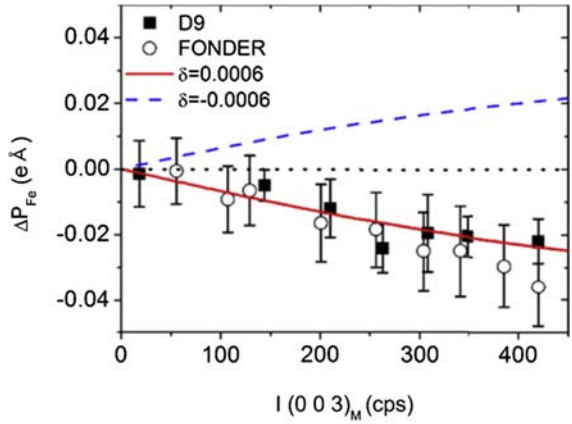

FIGURE 16 Plot of the induced electric polarization of Fe (ΔP_{Fe}) against the measured intensity of the (003) ± Q magnetic superlattice peaks. The solid line represents the theoretical calculation results based on the Ginzburg–Landau free energy analysis with a negative magnetoelectric coupling, while the dashed line shows the theoretical results expected for the case with the opposite sign for the magnetoelectric coupling. *Reprinted with permission from Lee et al. (2013). Copyright 2013 by the American Physical Society.*

representative magnetic superlattice peak. The experiment results support a model in which magnetostriction overweights Dzyaloshinskii–Moriya effect as cause of magnetoelectricity in BFO.

3.1.1 Magnetic Phase Diagram of Strained BFO Films

The contribution by Sando et al. (2013) on strained $BiFeO_3$ is worth being presented. Authors perform an interesting study of the magnetic response of strain-engineered $BiFeO_3$ films. Using Mössbauer and Raman spectroscopies combined with Landau–Ginzburg theory and effective Hamiltonian calculations, they show that the bulk-like cycloidal spin modulation that exists at low-compressive strain is driven toward pseudo-collinear antiferromagnetism at high strain, both tensile and compressive. For moderate tensile strain, Sando and collaborators observe indications of a new cycloid. The magnonic response is thus modified, with low-energy magnon modes being suppressed as strain increases. Strain progressively drives the average spin angle from in-plane to out-of-plane, a property that can be used to tune the exchange bias and giant-magnetoresistive response of spin valves (Figure 17).

3.1.2 Particle versus Spin Spiral Sizes

The peculiar magnetic behavior of $BiFeO_3$ nanoparticles with size approaching the period of the spiral spin structure (62 nm) has been characterized by Huang et al. (2013). Figures 18 and 19 describe the findings of this investigation.

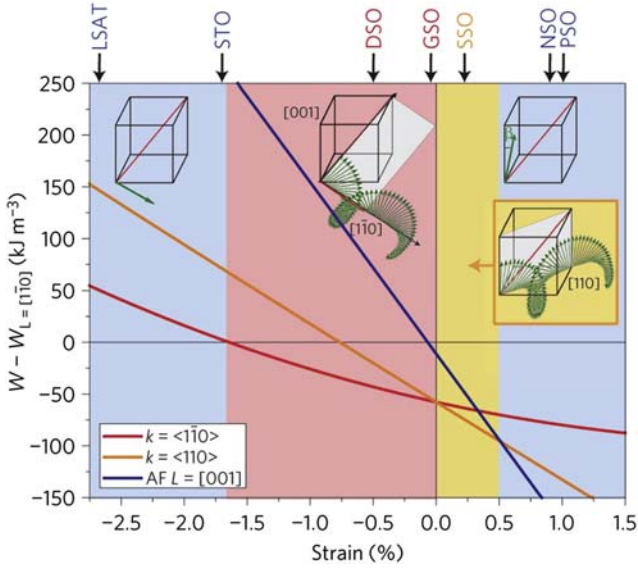

FIGURE 17 Magnetic phase diagram of strained BFO films. The energy of three magnetic states (bulk-like 'type-1' cycloid with propagation vector along $\langle 1, -1, 0\rangle$ directions, 'type-2' cycloid with propagation vector along $\langle 1, 1, 0\rangle$ directions, and collinear antiferromagnetic order with antiferromagnetic vector close to [0, 0, 1]), relative to a fourth magnetic state, corresponding to a collinear antiferromagnetic order with antiferromagnetic vector along in-plane [1, −1, 0] directions. The stability regions of the different states are shown in colors (blue (black in print versions): antiferromagnetic; red (dark gray in print versions): type-1 cycloid; orange (light gray in print versions): type-2 cycloid). The different substrates used are located on top of the diagram at their corresponding strain. Their color corresponds to the magnetic state determined from the Mössbauer measurements. The sketches represent the different magnetic states, with spins shown in green (gray in print versions). *Reprinted with permission from Macmillan Publishers Ltd: Nature Materials (Sando et al., 2013). Copyright 2013.*

Figure 19 shows the magnetization of investigated BFO nanoparticles as a function of temperature, measured at 200 Oe after zero-field cooling (ZFC) and also with 200 Oe field cooling (FC). There are three features worth mentioning: (1) The splitting in the ZFC and FC magnetization curves are observed for all the BFO nanoparticles. (2) With temperature decreasing from 300 K to 10 K, the ZFC magnetization value (MZFC) monotonically decreases for the 170 and 83 nm BFO particles, while it first increases and then decreases, as a result, a broad peak appears in the ZFC curves for the BFO particles with size less than 62 nm. (3) Except for the absence in 62 nm particles, a sharp cusp (shown in the Figure by arrows) is observed in the ZFC and FC curves for other BFO nanoparticles.

For the particles with size close to the spiral spin period of BFO, a structural anomaly arises, which improves the multiferroic and magnetoelectric coupling properties of the material.

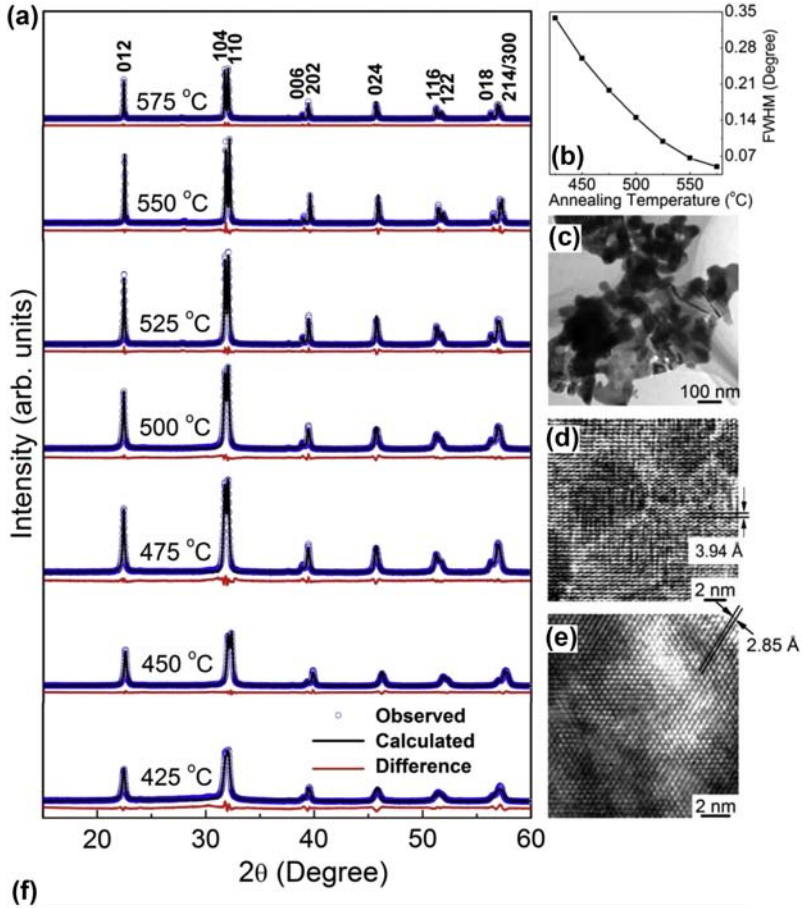

(f)

d	18 nm	31 nm	45 nm	62 nm	83 nm	170 nm	248 nm
R_p (%)	6.22	2.36	4.26	2.03	3.56	4.95	3.70
R_{wp} (%)	7.89	3.06	5.91	2.80	4.66	6.77	5.04
a (Å)	5.573	5.561	5.578	5.578	5.579	5.572	5.578
c (Å)	13.838	13.819	13.868	13.871	13.870	13.852	13.869

FIGURE 18 (a) X-ray diffraction patterns of BFO nanoparticles annealed at various temperatures. (b) Annealing temperature-dependent full width at half maximum (FWHM) of (0, 1, 2) peak. (c) The TEM image and (d−e) high resolution TEM images of the 62 nm BFO particles. (f) Parameters obtained from Rietveld refinement. *Reprinted with permission from Macmillan Publishers Ltd: Scientific Reports (Huang et al., 2013). Copyright 2013.*

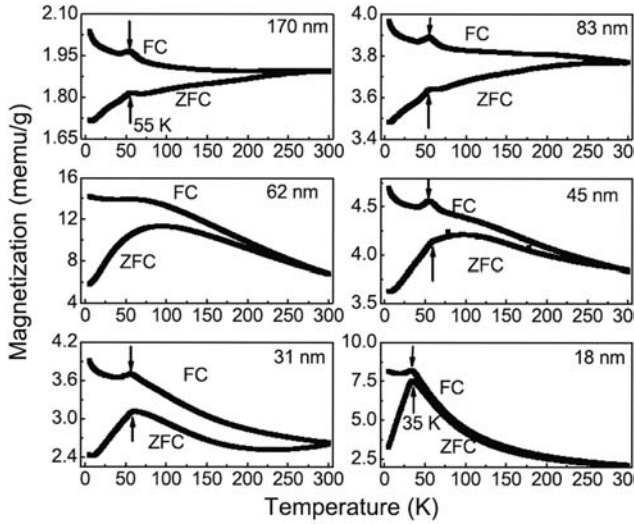

FIGURE 19 Magnetization as a function of temperature measured under ZFC and 200 Oe FC conditions for BFO nanoparticles with various sizes. *Reprinted with permission from Macmillan Publishers Ltd: Scientific Reports (Huang et al., 2013). Copyright 2013.*

3.2 $RFeO_3$ Orthoferrites

Orthoferrites, with generic formula $RFeO_3$ (R being a Rare Earth atom), have had significant attention in the quest for multiferroics. Recent reports by Ye and Vanderbilt (2015) and Disseler et al. (2015) are representative of the state of the art. Here we cite in some detail the work by Ghosh et al. (2014). Considered materials have an orthorhombic structure belonging to *Pbnm* space group and show antiferromagnetic behavior, together with weak ferromagnetism. As they entail non-centrosymmetric cells, they are also good candidates as ferroelectrics.

$LaFeO_3$ is a promising type-G antiferromagnetic material which has been doped with Gd for such purpose; resulting in $La_{0.9}Gd_{0.1}FeO_3$.

It is known that, in the case of these perovskites, the rotation of FeO_6 octahedra promotes buckling in the bonds Fe−O−Fe. This type of distortion generates a trend toward orbital ordering on the site of the Fe^{3+}, which induces a competition between σ ferromagnetic orbitals and π antiferromagnetic orbitals. This controversy is solved by the exchange interaction between neighboring spins along the Fe−O−Fe direction.

Structural investigation of LGFO suggests a distortion of the orthorhombic perovskite at room temperature and the introduction of Rare Earths generates a tilting of the FeO_6 octahedra (see Figure 20(a)).

In this structure, the octahedra are separated from each other by layers of Rare Earth ions. Therefore, the displacement of oxygen ions in the Fe−O−Fe

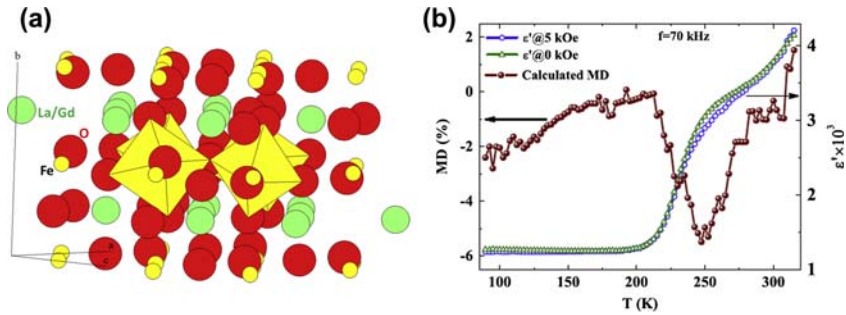

FIGURE 20 Magnetoelectric effect in $La_{0.9}Gd_{0.1}FeO_3$: (a) crystal structure; (b) change of the magnetodielectric coefficient with temperature. *Figure 20(b) reprinted from Ghosh et al. (2014). Copyright 2014, with permission from Elsevier.*

line generates a smaller crystal symmetry and, subsequently, generates an electric dipole moment; so that the magnetic exchange interaction here leads to a magnetic equivalent of the Jahn−Teller effect.

The dependence of the electric polarization with the magnetic field can be attributed to the Dzyaloshinskii−Moriya (DM) antisymmetrical interaction, in which the electric dipoles are induced by the antiferromagnetic exchange between nearest neighbors. This can be considered as a dipolar relaxation in an ordered magnetic state. In other words, the DM interaction induces a movement of the Oxygen ions *perpendicularly* to the chain of magnetic ions, providing for a perpendicular polarization as well.

To investigate the relationship between electrical and magnetic properties, the dependence of the polarization with the magnetic field was measured. Figure 20(b) shows the study of the magnetodielectric effect with respect to the temperature. A very large value of −5.5% was found at 247 K and 70 kHz. This response is a manifestation of the coupling between the spin and the structure, as it can be interpreted as the influence of the magnetic field on the DM interaction at the point where the inversion symmetry is broken. As a result, a change in the charge distribution of the Fe−O−Fe bond, generating an electric dipole, is induced.

3.3 A Magnetoelectric *Cubic* Perovskite

A recent article (Wang et al., 2015) describes an interesting case of magnetoelectric multiferroicity in the compound $LaMn_3Cr_4O_{12}$, which exhibits crystallographic cubic symmetry, space group *Im*-3. Figure 21 shows the atomic distribution and also the orientations of atomic magnetic moments in the investigated material. As discussed by Wang, the magnetoelectric effect is linked with the magnetic symmetry group. The performed structural and magnetic characterization shows that in $LaMn_3Cr_4O_{12}$ the

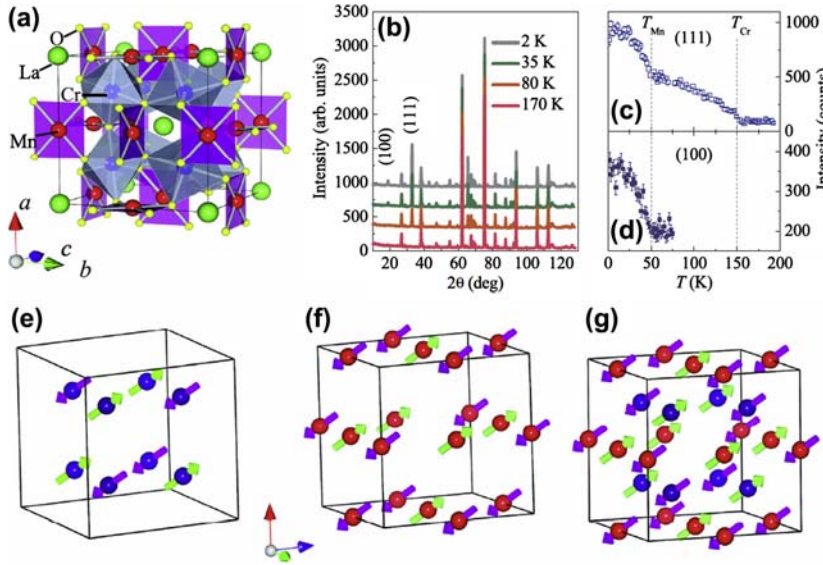

FIGURE 21 (a) Schematics of crystal structure of LMCO with space group *Im*-3. (b) NPD patterns at selected temperatures. The indexed (111) and (100) peaks arise from the AFM ordering of the B-site Cr sublattice and the A'-site Mn sublattice, respectively. (c) and (d) Temperature dependence of the integrated NPD intensities of (111) and (100) peaks, respectively. (e) and (f) G-type AFM structure of the B-site Cr sublattice and the A'-site Mn sublattice with spin orientation along the [111] direction, respectively. (g) A complete set of spin alignment composed of Cr and Mn spins below T_{Mn}. For clarity, La and O atoms are omitted in the structures. Blue (black in print versions) ball, Cr atom; red (gray in print versions) ball, Mn atom. *Reprinted with permission from Wang et al. (2015). Copyright 2015 by the American Physical Society.*

interaction between two magnetic sublattices plays a crucial role. The magnetic point group of the low-temperature configuration is *3*, compatible with magnetoelectric-multiferroicity (Table 1, present review).

3.4 Double Perovskites

The recent reports by Masud et al. (2015) and Yi et al. (2015) exemplify the international research effort that is being performed in relation with the family of double perovskites. The multiferroic behavior in the double-perovskite Lu_2MnCoO_6 has been investigated in detail by (Yáñez-Vilar et al., 2011). This material possesses a net electric polarization strongly coupled to a net magnetization below 35 K.

The reported investigation demonstrates that Lu_2MnCoO_6 is a multiferroic oxide, showing magnetic order below 43 K, and ferroelectricity below 35 K that is strongly coupled to a net magnetism (Figures 22–24).

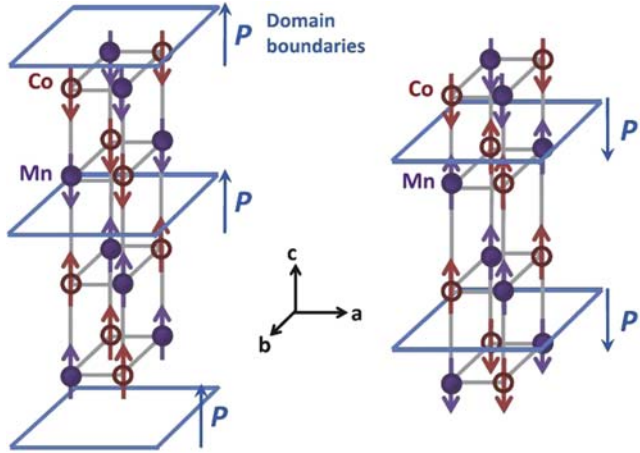

FIGURE 22 Derived $\uparrow\uparrow\downarrow\downarrow$ Mn^{4+} $S = 3/2$ and Co^{2+} $S = 3/2$ spin orientations along the c-axis at $T = 4$ K. Domain boundaries refer to the boundary between $\uparrow\uparrow$ and $\downarrow\downarrow$. Two scenarios (left and right) for the location of domain boundaries are shown, along with possible resulting electric polarizations *P*. In the *a*-*b* plane, an additional slow and incommensurate modulation of the spins occurs such that $\boldsymbol{k} = (0.0223(8),0.0098(7),0.5)$. *Reprinted with permission from Yáñez-Vilar et al. (2011). Copyright 2011 by the American Physical Society.*

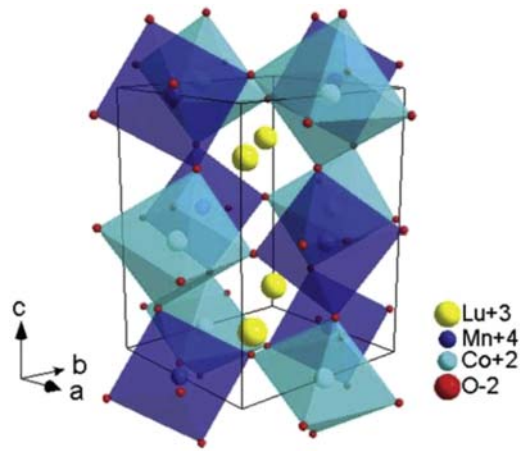

FIGURE 23 Monoclinic crystal structure of Lu_2MnCoO_6 showing the tilted oxygen octahedra surrounding alternating Mn^{4+} (dark blue (dark gray in print versions)) and Co^{2+} (light blue (light gray in print versions)) ions. Yellow (white in print versions) Lu ions are also shown. Oxygen ions are small red (gray in print versions) dots at the corners of the octahedra, and Lu ions are the largest yellow (white in print versions) balls interstitial between the octahedra. *Reprinted with permission from Yáñez-Vilar et al. (2011). Copyright 2011 by the American Physical Society.*

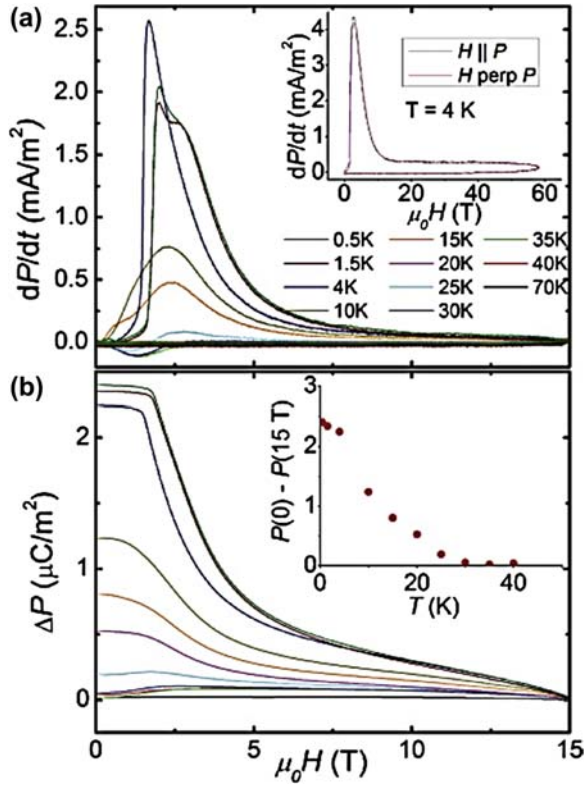

FIGURE 24 (a) Measured change in electric polarization with time, *dP/dt* as a function of magnetic field H for various temperatures "T" during a rapid magnetic-field pulse for the geometry $P \Uparrow H$. Before measuring *dP/dt*, the sample was poled by applying an electric field of 2 MV/m in zero magnetic field while cooling from 70 K to the intended measuring temperature, at which point the electric field was removed and both sides of the sample were shorted. The inset shows data up to 60 T for P parallel and perpendicular to H at 4 K, with a 2 MV/m poling voltage. (b) $P(H)$ determined by integrating the data in (a). The inset shows $P(H = 0\ \text{T}) - P(H = 15\ \text{T})$ as a function of temperature. *Reprinted with permission from Yáñez-Vilar et al. (2011). Copyright 2011 by the American Physical Society.*

3.5 Aurivillius Phases

Aurivillius phases, crystals formed by perovskite octahedra "sandwiched" among bismuth oxide layers, continue under scrutiny as promising candidates for room-temperature magnetoelectric multiferroics. Recent reports on neodymium and cobalt co-doped four-layer Aurivillius phase (Zhang et al., 2015), $Bi_4LaTi_3FeO_{15}$ (Ti et al., 2015) and $Bi_4NdTi_3Fe_{0.7}Co_{0.3}O_{15}$ (Chen et al., 2015b), illustrate current tendencies in this branch. Here we divulge the characteristic results obtained by Chen et al., 2015b.

$Bi_4NdTi_3Fe_{0.7}Co_{0.3}O_{15}$ is a four-layer Aurivillius phase with orthorhombic symmetry. The electric and magnetic hysteresis loops in Figure 25(a) and (b)

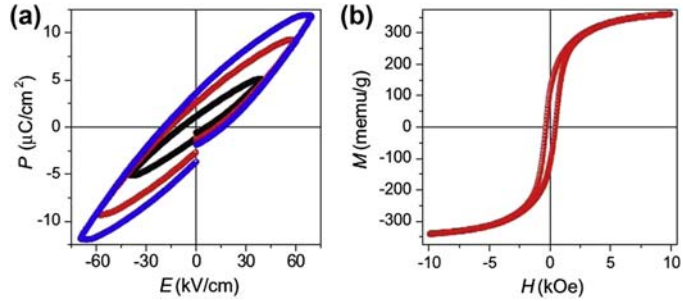

FIGURE 25 (a) P–E hysteresis loops and (b) magnetic hysteresis loop of BNTFC ceramic measured at room temperature. *Reprinted from Chen et al. (2015b). Copyright 2015, with permission from Elsevier.*

demonstrate the multiferroic nature of the considered material. Figure 26(a) and (b) present the nonlinear magnetization curves with insets that show the dependence of the magnetodielectric (MD) effect as a function of the magnetization. An interesting result of this experiment is the finding that the MD coefficient is linear with M^4.

3.6 Doped ZnO

Zinc oxide is a well-known n-type semiconductor with a wide band gap of 3.5 eV. When ZnO is doped with transition metals (TM), it is considered a part of a group of materials known as "diluted magnetic semiconductors" (DMS). They have several degrees of freedom in their charge and spin, thus they deserve ample interest in the scientific community.

A recent, interesting report by Sharma et al. (2014) describes the ferroelectric, ferromagnetic, and magnetoelectric properties of pure and doped ZnO. Applied dopants were Ni, Li, and Mg. Here we summarize the magnetoelectric results.

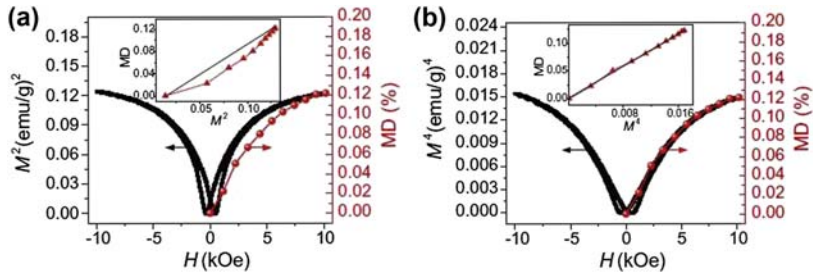

FIGURE 26 Behavior of the magnetodielectric coefficient, as a function of the magnetization, for BNTFC ceramic measured at room temperature. *Reprinted from Chen et al. (2015b). Copyright 2015, with permission from Elsevier.*

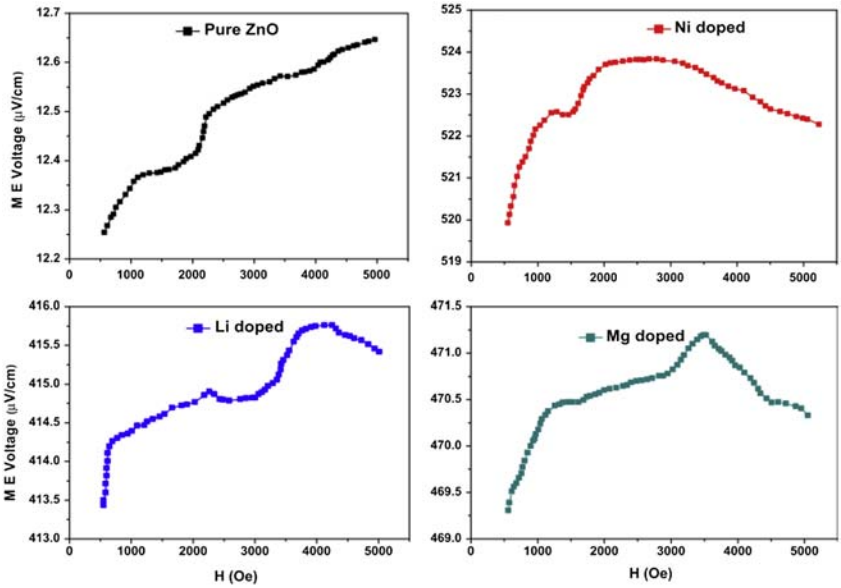

FIGURE 27 Magnetoelectric coupling for pure and doped ZnO. *Reprinted from Sharma et al. (2014). Copyright 2014, with permission from Elsevier.*

Magnetoelectric measurements were realized by a dynamic method. The results obtained for the *practical* magnetoelectric coefficient α are presented in Figure 27. It is seen that the samples doped with Ni and Mg showed plots that were closer to the ideal parabolic shape.

3.7 $TbMnO_3$ and Its Cycloidal Spin Ordering

$TbMnO_3$ (TMO) is representative of cycloidal spin ordering. At low temperatures, collinear sinusoidal antiferromagnetic spin ordering arises. Further cooling causes a *bc*-plane cycloidal (transverse-spiral) spin ordering with magnetically induced spontaneous polarization along the c-axis. A schematic drawing of the spin configuration and the temperature-dependent evolution of physical properties in TMO are presented in Figure 28, originally from (Kimura et al., 2003) and divulged in the review by Lu et al. (2015).

4. SINGLE-PHASE POLYCRYSTAL MAGNETOELECTRICS

4.1 Macroscopic Anisotropy of Magnetoelectric Polycrystals

The physical properties of a polycrystalline material are similar to those of a single crystal, modulated by a combination of factors. Among these factors, crystallographic texture is one of the most important ones (Bunge, 2013; Chateigner, 2013; Wenk and Van Houtte, 2004). Connectivity (Behera et al., 2015),

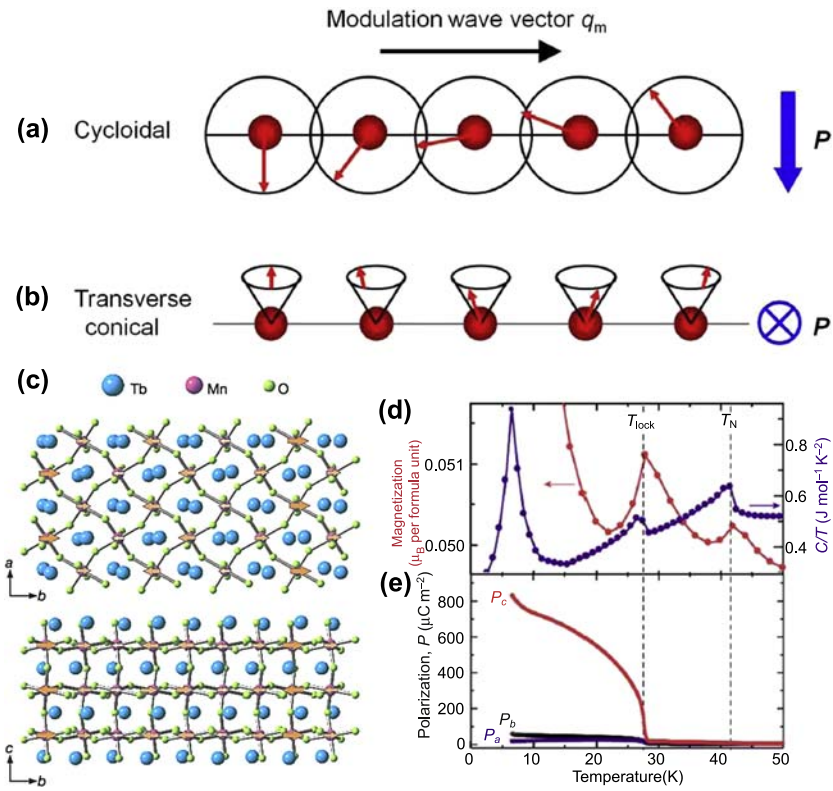

FIGURE 28 Schematic drawings of (a) cycloidal and (b) transverse conical spin ordering. (c) Collinear sinusoidal spin ordering as $T_C < T < T_N$ (up), and spiral-spin-ordering as $T < T_C$ in multiferroic $TbMnO_3$. Temperature-dependent magnetization and specific heat (d), and spontaneous polarization (e) along different axes in TbMnO3. *Reprinted with permission from Macmillan Publishers Ltd: Nature (Kimura et al., 2003). Copyright 2003.*

morphologic texture (Ahmed et al., 2015), and stereography (Bunge et al., 2000) are recognized (and linked among them) factors that can also exert a decisive influence on polycrystal properties. The structure and physical properties of textured polycrystals are analyzed in an Appendix to the present chapter.

In order for a given sample to exhibit anisotropic macroscopic ME properties, two necessary conditions must be fulfilled. The first one is that the individual crystallites possess intrinsically an anisotropic ME property tensor. But, in a polycrystalline aggregate, this intrinsic anisotropy of the crystals can be revealed at the macroscopic scale of the specimen only in the presence of texture. We can then distinguish four different types of samples:

- Randomly oriented specimen with isotropic ME crystallites (isotropic sample).

- Textured specimen with isotropic ME crystallites (textured isotropic sample).
- Randomly oriented specimen with anisotropic ME crystallites (isotropized sample).
- Textured specimen with anisotropic ME crystallites (anisotropic sample).

The idea of texture includes both morphological and crystallographic textures, since a specimen with randomly oriented crystals but with anisotropically aligned grain shapes (morphological texture) can still be macroscopically anisotropic. For instance, in an isotropized sample, with a strong morphological texture and in absence of crystallographic texture, the interaction between neighboring grains can result in mechanically anisotropic properties. The term quasi-isotropic is sometimes used for isotropized samples (Welzel et al., 2005) but the term "quasi" tends to suggest would let imagine that anisotropy is quite eliminated but not entirely. The latter term has the advantage, to our opinion, not to mislead the interpretation, but to clearly state that the elaboration method has given the specimen a full isotropic character. In the case of ME properties, demagnetization effects due to crystallite shapes might also influence the ME tensor.

As a general trend, theoretical simulation aims at providing some methodology to model the macroscopic ME property, $\boldsymbol{\alpha}^{\mathbf{M}}$, from the microscopic, intrinsic properties of the individual (meso- or nano-) crystallites, $\boldsymbol{\alpha}$, described above. The former tensor is obviously of the same rank as the latter (Fuentes-Cobas and Fuentes-Montero, 2008; Nye, 1985). The link between these two quantities is largely influenced by preferred orientations, in a general meaning, that is including crystallographic and morphological textures.

Next we present a representative experimental investigation of textured single-phase magnetoelectric multiferroics and a set of simulated studies of textured magnetoelectric polycrystals. We try to deliver a bird's eye view of the diversity of effects that texture introduces in polycrystal magnetoelectricity.

4.2 Experimental Investigation of Textured Magnetoelectric Thin Films

Here we describe the results obtained by Raymond et al. (2014) on $Pb(Fe_{0.5}Nb_{0.5})O_3$ thin films. Mentioned authors have successfully grown highly textured single-phase multiferroic PFN thin films on SRO/Si substrates by RF magnetron sputtering. So-obtained PFN thin films exhibit ferroelectric properties comparable with those reported for epitaxial PFN thin films grown by PLD. Ferroelectricity coexists with a new ferromagnetic structure typical of spin-glass-like materials at temperatures below 50 K. Obtained ferroelectric and magnetic properties are exploitable (Figures 29–31).

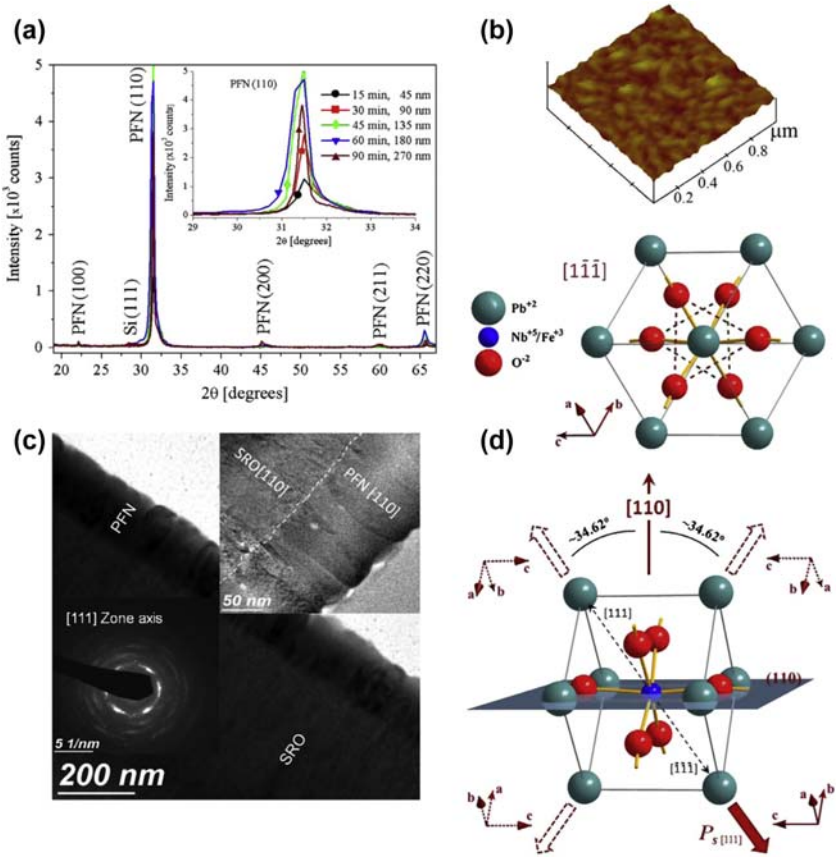

FIGURE 29 Structural and morphological characterization of a PFN(110)/SRO(110)/SiOx/Si(111) film system: (a) XRD patterns of PFN films of different thicknesses (inset: a zoom of the (110) reflection); (b) a representative AFM topography image of the top surface; (c) a representative cross-sectional TEM micrograph (inset: a zoom of the PFN/SRO interface is shown on the right, where the white line is a visual guide; an electron diffraction pattern of the PFN film is shown on the left). (d) PFN structural simulation of a [1, −1, −1] projection (bottom), and of the four possibilities where the spontaneous polarization Ps[111] can be located (top), with respect to the out-of-plane [110] preferential orientation. *Reprinted from Raymond et al. (2014). Copyright 2014, with permission from Elsevier.*

4.3 Single-Phase Polycrystal Magnetoelectrics: In Silico Case Studies

In this section we model hypothetical textures and simulate the orientation-dependent ME tensors of the textured polycrystals using several averaging techniques. The objective of the presentation is to divulge the interesting spectrum of effects that texture exerts in the magnetoelectricity of polycrystalline materials.

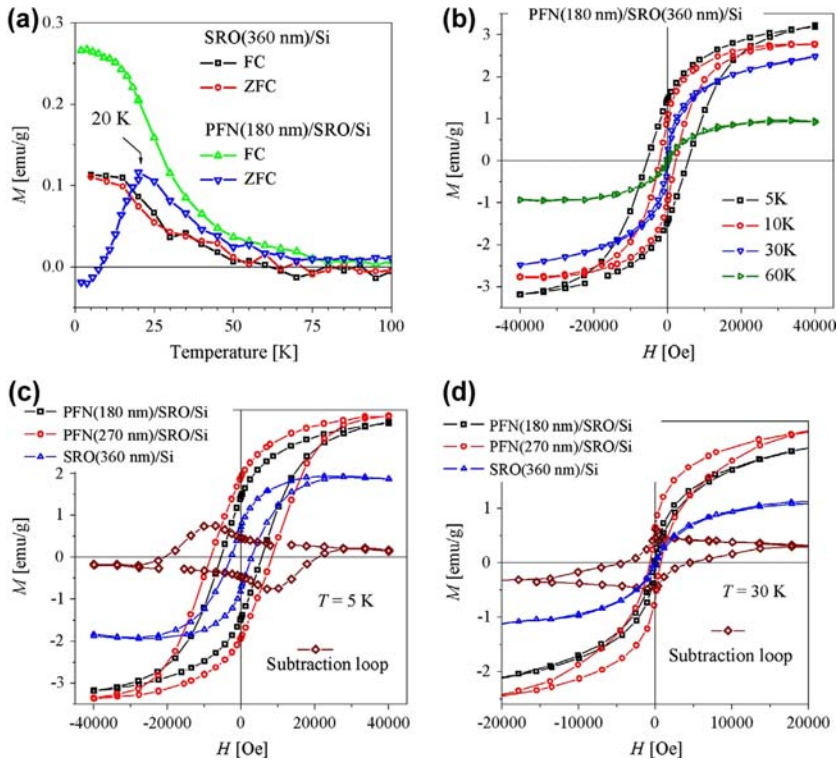

FIGURE 30 Magnetic properties: (a) field cooled (FC) and zero-field cooled (ZFC) magnetization curves of SRO/Si and PFN/SRO/Si systems; (b) magnetization versus magnetic field (M−H) loops of the PFN/SRO/Si system at different temperatures around 20 K; and (c,d) M−H loops at 5 and 30 K, respectively, of the PFN/SRO/Si system with PFN films of 180 and 270 nm thickness compared with the M−H loop of the SRO/Si substrate. The loop marked by diamond symbols is a subtraction of the PFN(180 nm)/SRO/Si sample loop from that corresponding to the PFN(270 nm)/SRO/Si sample. *Reprinted from Raymond et al. (2014). Copyright 2014, with permission from Elsevier.*

The following software packages are applied:

- SAMZ (Fuentes-Cobas et al., 2013) http://crystal.cimav.edu.mx/samz/

  SAMZ represents axially symmetric textures by means of inverse pole figures (IPFs) and calculates the Voigt, Reuss, and Hill approximations. IPFs are represented by March−Dollase and by Gaussian distributions. Considered properties are those associated to second, third, and fourth rank tensors. It displays the IPF and the longitudinal properties surfaces for the investigated single- and textured polycrystals.

- MAUD (Lutterotti et al., 2004) http://www.ing.unitn.it/∼maud/

  MAUD started as a diffraction/reflectivity analysis program mainly based on the Rietveld method. Nowadays it has grown to solve a great

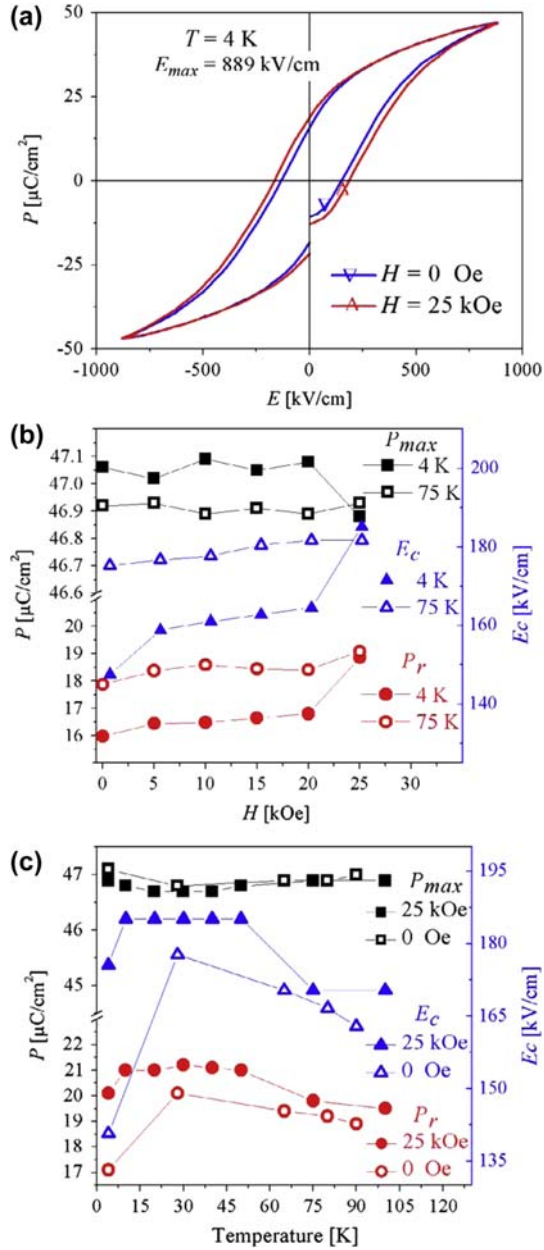

FIGURE 31 Magnetoelectric coupling (MEC) effects in the Au/PFN/SRO/Si system (PFN film 135 nm thick): (a) a representative full P–E loop measured without and with an out-of-plane applied magnetic field of 25 kOe at 4 K; hysteresis parameters *Pmax, Pr, Ec* behavior as functions of (b) the applied magnetic field at 4 and 75 K and (c) the temperature under a magnetic field of 0 and 25 kOe. All P–E loops were measured at $E_{max} = 889$ kV cm^{-1} (12 V). *Reprinted from Raymond et al. (2014). Copyright 2014, with permission from Elsevier.*

diversity of crystallographic problems, including the calculation of average properties for textured polycrystals. MAUD applies the Reuss−Voigt, arithmetic, and geometric mean models. The texture of the simulated samples is represented by means of their (direct) pole figures (PFs). The 1 (rolling), 2 (transverse), and 3 (normal) directions of the sample being respectively the vertical and horizontal axes of the pole figure planes, and the centers of the pole figures. Texture components are modeled using standard functions (Matthies et al., 1987).

Our first case study refers to a textured Cr_2O_3 polycrystal at 4.2 K, with different orientation distributions. The single-crystal case was presented in the section about the MPOD web application.

Figure 32(a) and (b) represent the results of simulations for a fiber texture with crystal c-axes aligned preferentially along sample direction 3, with a (relatively sharp) Gaussian distribution of 30° FWHM. As shown in the calculated matrices, as well as in the Voigt−Reuss−Hill (VRH) plots (Figure 32(b)), the polycrystal exhibits practically the same axially symmetric magnetoelectric behavior as the single crystal. The different approximations and computer treatments produce similar results.

The following matrices compare the magnetoelectric tensors of a Cr_2O_3 single crystal with the ones corresponding to a [crystal 001 ⇑ sample 3direction] texture, with FWHM = 30° (values in ps/m). Calculations performed by MAUD.

Single crystal

$$\begin{bmatrix} 0.73 & 0 & 0 \\ 0 & 0.73 & 0 \\ 0 & 0 & 0.23 \end{bmatrix}$$

Voigt average

$$\begin{bmatrix} 0.71 & 0 & 0 \\ 0 & 0.71 & 0 \\ 0 & 0 & 0.28 \end{bmatrix}$$

Geometric average

$$\begin{bmatrix} 0.69 & 0 & 0 \\ 0 & 0.69 & 0 \\ 0 & 0 & 0.26 \end{bmatrix}$$

Figure 33 represents selected pole figures for a Cr_2O_3 textured polycrystal with crystal **a-**, **b-**, and **c**-axes preferentially oriented along the 1, 2, and 3 sample axes respectively and keeping the same Gaussian distribution width

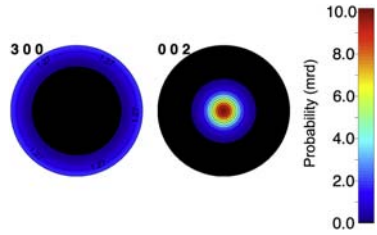

FIGURE 32(a) MAUD modeled 300 and 002 pole figures. Cr_2O_3 polycrystal. Axial Gaussian [crystal 001 ⇑ sample 3direction] texture, FWHM = 30°.

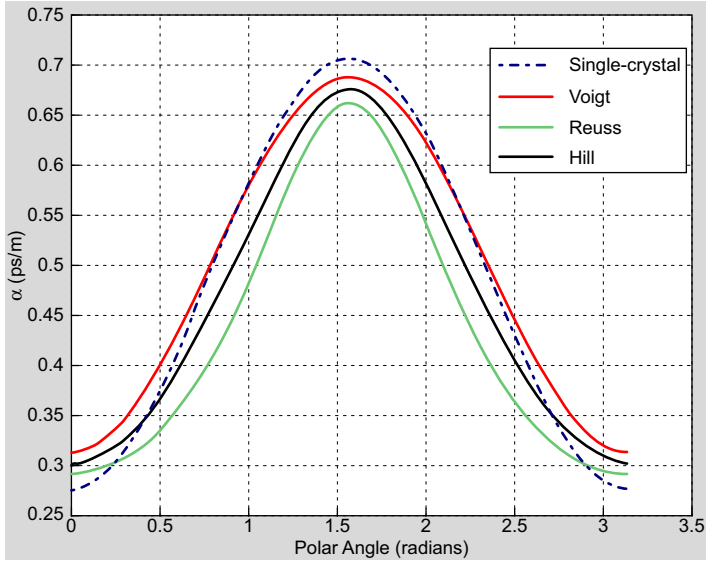

FIGURE 32(b) Magnetoelectric longitudinal modulus for Cr_2O_3 single- and sharp-textured polycrystal. Calculations performed by SAMZ. The values at polar angle $\phi = 0$ and $\pi/2$ represent, respectively, α_{33} and α_{11}. Compare with Figure 5 and with the given matrices.

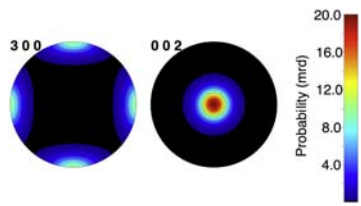

FIGURE 33 Cr_2O_3 polycrystal (0,0,0) spherical texture component with 30° Gaussian FWHM.

FWHM = 30° (Figure 32(a)). Tensor averaging gives the same values as for the fiber case.

This interesting result is due to the axially symmetric tensor character. Practically speaking, this would mean that, for example, epitaxial-like relationships in thin film elaboration would not be required from the orientation point of view only.

Inclining the Cr_2O_3 crystals **c**-axis by 45° from both 1 and 3 sample axes (Figure 34), a clear tendency to isotropization of the tensor is observed. This same effect would also be produced by randomization of part of the

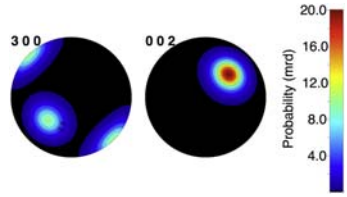

FIGURE 34 Cr_2O_3 polycrystal off-centered texture pole figures.

crystals in the sample volume and/or enlargement of the FWHM of the distribution of orientations.

Cr_2O_3 off-centered texture magnetoelectric matrices (MAUD).

$$\text{Voigt average} \begin{bmatrix} 0.6 & -0.1 & -0.1 \\ -0.1 & 0.6 & -0.15 \\ -0.15 & -0.15 & 0.49 \end{bmatrix} \quad \text{Geometric average} \begin{bmatrix} 0.58 & -0.1 & -0.15 \\ -0.1 & 0.58 & -0.15 \\ -0.15 & -0.15 & 0.47 \end{bmatrix}$$

Our second case study refers to $K_2[FeCl_5(H_2O)]$, a material also presented in the MPOD section, above. We first consider fiber textures. Figure 35 and accompanying matrices represent the evolution of the magnetoelectric tensor of this material as the orientation distribution width increases. Calculations, in the Voigt approximation, were performed with program SAMZ.

As expected, for all fiber textures the property surface shows axial symmetry.

It is worth noting that for the sharp axial texture (FWHM = 10°):

$\langle \alpha_{11} \rangle = \langle \alpha_{22} \rangle = 0.398 \approx 0.5(\alpha_{11} + \alpha_{22})$

$\langle \alpha_{33} \rangle \approx \alpha_{33}$.

When the width of the orientation distribution grows significantly, all the elements in the magnetoelectric matrix tend to the arithmetic average of the three diagonal elements.

The pole figures in Figure 36 represent a $K_2[FeCl_5(H_2O)]$ polycrystal with (0,0,0) spherical Lorentzian texture, 50° FWHM.

For this hypothetical polycrystal, the output from program MAUD is the following set of magnetoelectric matrices.

$$\text{Single crystal} \begin{bmatrix} 0.71 & 0 & 0 \\ 0 & 0.08 & 0 \\ 0 & 0 & 1.17 \end{bmatrix} \quad \text{Voigt average} \begin{bmatrix} 0.69 & 0 & 0 \\ 0 & 0.29 & 0 \\ 0 & 0 & 0.98 \end{bmatrix} \quad \text{Geometric average} \begin{bmatrix} 0.58 & 0 & 0 \\ 0 & 0.14 & 0 \\ 0 & 0 & 0.80 \end{bmatrix}$$

The polycrystal property preserves the single crystal orthorhombic symmetry. The difference between the Voigt and the geometric averages is noticeable. This is an expression of the importance of sample's stereography.

(a) Single crystal

$$\propto = \begin{bmatrix} 0.71 & 0 & 0 \\ 0 & 0.08 & 0 \\ 0 & 0 & 1.17 \end{bmatrix}$$

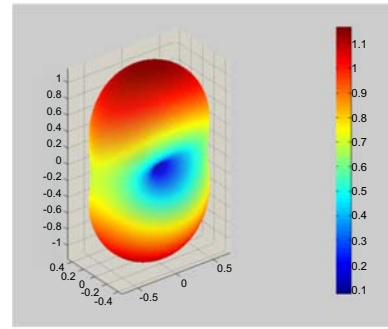

(b) Sharp fibre texture, FWHM = 10°

$$\langle \propto \rangle = \begin{bmatrix} 0.398 & 0 & 0 \\ 0 & 0.398 & 0 \\ 0 & 0 & 1.17 \end{bmatrix}$$

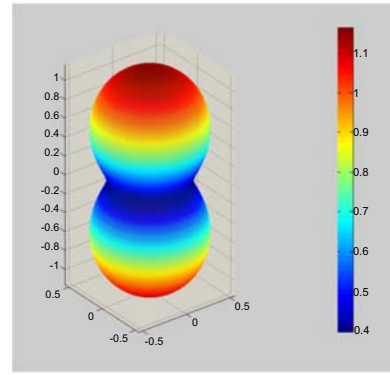

(c) Broad fibre texture, FWHM = 90°

$$\langle \propto \rangle = \begin{bmatrix} 0.58 & 0 & 0 \\ 0 & 0.58 & 0 \\ 0 & 0 & 0.81 \end{bmatrix}$$

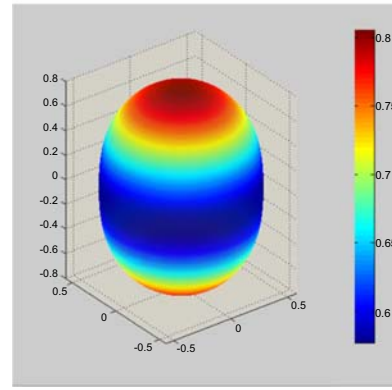

FIGURE 35 Magnetoelectricity in fiber textures of $K_2[FeCl_5(H_2O)]$. Values in ps/m. Crystal magnetic point group $m'm'm'$.

In the considered case the effect is highly visible because the crystals are extremely anisotropic.

Our last case study focuses on $LiCoPO_4$. Figure 37 above shows the single-crystal magnetoelectric longitudinal surface. The magnetic point group mmm' (significantly different from $m'm'm'$ of $K_2[FeCl_5(H_2O)]$) leads to interesting features for this system.

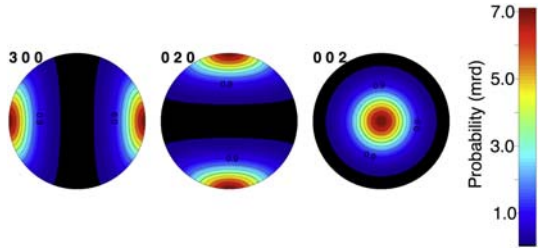

FIGURE 36 Pole figures of a $K_2[FeCl_5(H_2O)]$ polycrystal. Crystal **a-**, **b-**, and **c**-axes preferentially oriented along the 1, 2 and 3 sample axes, respectively. Lorentzian texture with FWHM = 50°.

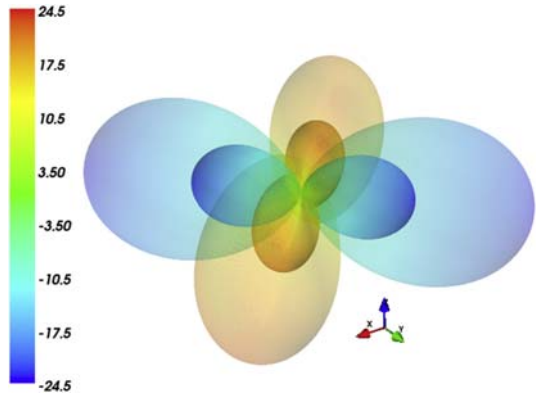

FIGURE 37 Single- and polycrystal longitudinal magnetoelectric surfaces for $LiCoPO_4$. The external surface corresponds to the single crystal. The considered ODF is composed by a Gaussian component at the origin of the Euler space, with an FWHM of 30°.

The magnetoelectric matrix is as follows:

$$\propto = \begin{bmatrix} 0 & 18.4 & 0 \\ 30.6 & 0 & 0 \\ 0 & 0 & 0 \end{bmatrix} \quad \text{ps/m} \quad T = 4.2 \text{ K}$$

Qualitatively, as well as mathematically, one finds that fiber textures of the types previously considered show no magnetoelectric effect.

Sharp orthorhombic textures exhibit magnetoelectricity, with tensor and surface figures that weaken and tend to collapse as the orientation distribution broadens. This kind of polycrystal magnetoelectrics has been analyzed in detail by Fuentes (1998) and Fuentes et al. (2006). Figure 37 shows representative magnetoelectric longitudinal surfaces for $LiCoPO_4$ single crystal and a virtual textured polycrystal.

The question of magnetoelectricity in textured polycrystals, in order to beneficiate of maximum tensor coefficients, strongly depends on types and widths of the texture components, and of the initial, single crystal ME tensor. This last factor depends in a significant manner on crystal magnetic symmetry. Texture and single crystal property measurements are the prerequisite keys for a good estimate of sample's macroscopic ME properties.

5. COMPOSITE MAGNETOELECTRICS

5.1 General Issues on Magnetoelectric Composites

At present, the research area of magnetoelectric composites involves (1) particulate, (2) laminate, and (3) thin films systems of piezoelectric and magnetostrictive materials. Although laminated magnetoelectric composites exhibit larger magnetoelectric response, powder technology provides advantages such as cost effectiveness, easy fabrication process, better control of the process parameters, and fabrication of large volumes (Brosseau et al., 2010). From the point of view of the dynamics of the applied electric and magnetic fields, three frequency ranges are of interest: low frequencies, tens and hundreds of kHz, and RF and microwave frequencies. In laminates with dimensions in the order of a few mm, the electromechanical resonance is exploited, in the range of tens to hundreds of kHz, to increase the magnetoelectric coefficients, while in the RF and microwave range of frequencies, ferromagnetic resonance is exploited to increase the magnetoelectric coefficients. In single crystal films with nanometric dimensions, the magnetoacoustic resonance is exploited to increase the magnetoelectric coefficients. In this latter case, the small dimensions of the films and devices allow to tune the electromechanical resonance frequency with the ferromagnetic resonance frequency in the GHz region, that is, in the system, two resonance phenomena operate simultaneously, and this enables, in principle, to obtain a giant magnetoelectric effect.

The values of the magnetoelectric coefficients, obtained with the help of the electromechanical resonance, are always greater than the values obtained at low frequencies. In the electromechanical resonance, a longitudinal orientation is used when the applied magnetic field is parallel to the electrical poling direction, or a transverse orientation is used when the applied magnetic field is perpendicular to the electrical poling direction. The magnetoelectric coefficients are higher for the transverse orientation than for the longitudinal orientation, which is due to two factors: 1) higher energy losses for magnetic fields with longitudinal orientation due to eddy currents appearing at the plated electrodes, 2) influence of the demagnetizing field in the longitudinal orientation, which reduces the magnetic piezo-module.

From the viewpoint of the measurements, the magnetoelectric effect can be measured by applying a magnetic (electric) field and measuring the electric

polarization (magnetization). Moreover, some researchers extracted the magnetoelectric coefficients from measurements of the dielectric permittivity and/or magnetic permeability, and on theoretical considerations (Bartkowska, 2015). In this last case, it is assumed that the magnetoelectric effect is somehow implicit in the behavior of the dielectric permittivity and the magnetic permeability with temperature, frequency, and so on.

The phenomenon of magnetostriction is present in most of the known magnetically ordered materials. As the magnetostriction property is described by a fourth rank polar tensor, it must be exhibited by all crystal classes. On the other side, as the piezomagnetic effect is described by a third rank axial tensor, then, by symmetry considerations, the piezomagnetic effect is not required to be present in all crystal classes and its property matrix can become null by the action of specific symmetry operations. As the most prevalent form of magnetoelastic coupling is magnetostriction, the strains (ε_{ij}) induced by an external magnetic field (H) most frequently depend quadratically on the field strength, rather than linearly. This is the definition of magnetostriction, that is, $\varepsilon_{ij} = Q_{ijkl}H_kH_l$, where Q_{ijkl} are the magnetostriction coefficients (Bichurin and Petrov, 2014). This fact makes the product property, the magnetoelectric effect, in the piezoelectric−magnetostrictive composites, a nonlinear effect unlike the single-phase materials where the magnetoelectric effect is a linear effect over a wide range of values of the magnetic or electric field. Also the magnetoelectric effect in these composites shows a hysteretic behavior. This makes the applications of such composites difficult in linear devices. Linearity in such composites is achieved by applying a bias magnetic field across them so that the magnetoelectric effect over a short range around this bias field can be approximated as a linear effect. The hysteretic nature of this effect can be made use of in memory devices, for which there is no necessity of a bias magnetic field (Ryu, 2002).

In magnetoelectric nanocomposites, two key issues have been hotly debated in the field: the strength of the coupling between polarization and magnetization mechanisms and the role of interface. There has been an ongoing interest in the nature of structural transformations in nanoparticles (of typical size below 100 nm) systems under high pressure. Indeed, pressure offers the opportunity to drastically modify the electronic, magnetic, or thermomechanical properties of magnetoelectric nanocomposites. In experiments on multiferroic materials, it has been observed that the anomalies in the permittivity that occur at the onset or with changes in the magnetic order are generally associated with lattice distortions. This suggests that the magnetoelectric coupling proceeds via the lattice atomic displacements. For example, varying the degree of strain can be realized by choosing different orientations of the substrate which yields different phase morphologies in self-assembled epitaxial nanocomposite films. Related to this effect, the question of the role of compaction pressure as a mechanism to modify the magnetoelectric properties via the microstructure has not been addressed in detail. The difficulty in

controlling the bulk magnetoelectric property of granular nanocomposites is rooted in the complexity of the electric and magnetic dipoles properties of interfaces of these strongly correlated materials (Brosseau et al., 2010; Espinosa-Almeyda et al., 2011, 2014).

Finally, in Fuentes-Cobas et al. (2011) several experimental results about magnetoelectric composites, particularly different structures of laminate composites and magnetoelectric enhancement by resonance were reviewed, and readers are advised to review it.

5.2 Magnetoelectric Coefficients Measurement Methods

In Fuentes-Cobas et al. (2011) the measurement of the magnetoelectric coupling coefficients by the static, quasistatic, dynamic, and pulsed dynamic methods, as well as the theories of measurement by in-dynamic and pulsed dynamic methods were described, and readers interested in these topics are referred to this earlier review article.

The debate over the origin of the magnetoelectric effect continues today, with some researchers suggesting to probe the magnetoelastic coupling between the magnetostrictive and piezoelectric phases from the measurement of the effective complex permittivity ε and magnetic permeability μ since these quantities are the standard source of information on the response to external electric and magnetic fields (Brosseau et al., 2010).

In Bartkowska (2015), based on measurements of the temperature dependence of the dielectric permittivity and on theoretical considerations, the values of the magnetoelectric coupling coefficient (g) were calculated. In this article measurements are presented of temperature dependence of the dielectric response of multiferroic composites as a function of temperature, in the range from 300 to 780 K, for different frequencies of an applied electric field, for the multiferroic ceramics PSZTC−NiZn and PBZTN−NiZ, where PBZTN = $Pb_{0.90}Ba_{0.10}(Zr_{0.53}Ti_{0.47})O_3$ + 2 at % Nb_2O_5 and PSZTC = $Pb_{0.94}Sr_{0.06}(Zr_{0.46}Ti_{0.54})O_3$ + 0.25 at% Cr_2O_3 and NiZ = nickel−zinc ferrite. For the determination of the magnetoelectric coupling coefficient, two order parameters were imposed on each subsystem (piezoelectric and magnetostrictive): S_i and u_i, where S_i represents the classical Heisenberg spin for magnetic interaction and u_i is the electrical displacement for an electrical polar. The displacement u_i is proportional to the local spontaneous polarization p perpendicular to electronic spin S_i. In addition, Bartkowska also took into account the coupling interaction between the ferroelectric and magnetic subsystems. He concluded that the ferroelectric−ferromagnetic composite PSZTC−NiZn showed greater values of magnetoelectric coupling coefficient, than the composite PBZTN−NiZn and that this means that the composition of the ferroelectric part of the multiferroic composite influences the interaction among ferroelectric and ferromagnetic subsystems.

Magnetostrictive strain and magnetization curves of trilayered composites were experimentally determined by the quasi-static and the dynamic methods respectively at 1 and 1000 Hz (Zhang and Gao, 2015). They investigated the influence of hysteresis and temperature on the magnetoelectric effect of the trilayered composites, using a nonlinear dynamic hysteretic model they simulated by Finite Element Method including the elastic, magnetostrictive, and thermal strain in the magnetostrictive layers. The increment of temperature due to the magnetic hysteresis loss was also investigated. The effect of the temperature, the AC magnetic field and the bias field on the induced electric field, and the magnetoelectric effect were studied. The author concluded that the bigger the magnetic frequency, the larger the energy loss of the ME composites, while the initial temperature has little effect on the induced electric field at low magnetic field region, but significant effect on the induced electric field at high magnetic field region. Figure 38 shows the comparisons of magnetostrictive strain and magnetization hysteresis loops between the theoretical results and the experimental data from (Slaughter et al., 2000) for measurements at 1 and 1000 Hz by the quasistatic and the dynamic methods, respectively.

5.3 Magnetoelectric Effect Enhancement in Composites by Resonances

Electromechanical, ferromagnetic, and magnetoacoustic resonances allow the magnetoelectric coefficients to increase in orders of magnitude with respect to the static and low frequency values. Additionally, the high frequency applied electric and magnetic fields allow a faster response in applications. In Fuentes-Cobas et al. (2011) electromechanical resonance in laminate composites is discussed, and readers are advised to review it.

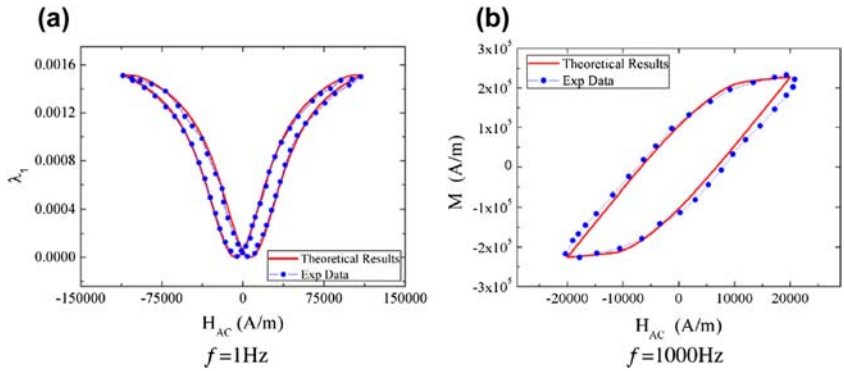

FIGURE 38 Comparison of magnetostrictive strain and magnetization curves between experimental data (Slaughter et al., 2000) and theoretical prediction (Zhang and Gao, 2015) in quasistatic and dynamic cases. *Reprinted from Zhang and Gao (2015). Copyright 2015, with permission from Elsevier.*

5.4 Electromechanical Resonance

Because the magnetoelectric effect in composites is due to mechanically coupled piezoelectric and magnetostrictive phases, it sharply increases in the vicinity of the electromechanical resonance frequency. Therefore, a resonance enhancement of magnetoelectric interactions is observed at frequencies corresponding to electromechanical resonance and the magnetoelectric coefficient value in the electromechanical resonance region exceeds the low frequency value by more than an order of magnitude. The peak transverse magnetoelectric coefficient at electromechanical resonance is larger than the longitudinal one due to eddy current losses and demagnetization fields. The mechanical oscillations of a magnetoelectric composite can be induced either by alternating magnetic or electric fields. If the length of the electromagnetic wave exceeds the spatial size of the composite by some orders of magnitude, then it is possible to neglect gradients of the electric and magnetic fields within the sample volume. The resonance enhancement of magnetoelectric effect in the vicinity of the electromechanical resonance frequency depends on the composite shape and on the orientation of applied electric and magnetic fields. Figure 39(a) and (b) shows the frequency dependence of the magnetoelectric voltage coefficients for the transverse and longitudinal orientation of the electric and magnetic fields, respectively, for a bilayer of nickel ferrite and lead zirconate titanate for the longitudinal mode of a narrow plate of 7.3 mm in length, Q = 105, and a lead zirconate titanate volume fraction of 0.6. Q is a factor determined experimentally. It can be seen that there is a good agreement between calculation (solid line) and data

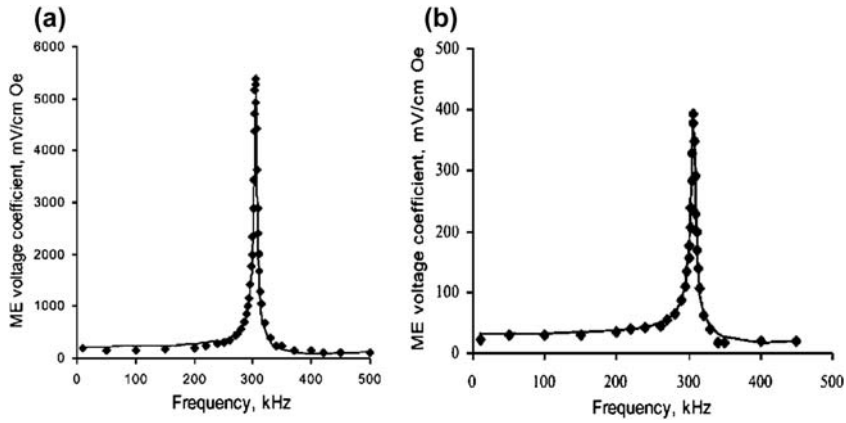

FIGURE 39 Frequency dependence of magnetoelectric voltage coefficients for (a) the transverse and (b) the longitudinal orientation for a bilayer of nickel ferrite and lead zirconate titanate. *Reprinted with kind permission from Springer Science and Business Media (Bichurin and Petrov, 2014). Copyright 2014.*

(points). High resonance frequency in the range of hundreds of kHz is observed. A similar behavior can be observed for the longitudinal mode in the radial direction for a disc-shaped bilayer. A key drawback for magnetoelectric effect at longitudinal modes is that the frequencies are quite high, on the order of hundreds of kHz, for nominal sample dimensions. In these cases the eddy current losses for the magnetostrictive phase can be quite high at such frequencies, in particular for transition metals and alloys and earth rare alloys such as Terfenol-D, resulting in an inefficient magnetoelectric energy conversion. In order to reduce the operating frequency, one must therefore increase the laminate size which is inconvenient for any applications. An alternative for getting a strong magnetoelectric coupling is the resonance enhancement at bending modes of the composite. For the bending mode, the resonance frequency of the applied ac field can be reduced to tens of kHz, and so the eddy current losses are also reduced. The lowest resonance frequency is expected for the bilayer clamped at one end. One expects bending motion to occur at decreasing frequencies with increasing bilayer length or decreasing thickness. Recent investigations have showed a giant magnetoelectric effect at bending modes in several layered structures (Bichurin and Petrov, 2014).

In Chen et al. (2015a) bending oscillations were excited in an FeNi-PZT-FeCuNiSiB trilayered composite with asymmetric magnetic layers, taking advantage of the flexural deformation caused by the asymmetric stress distribution in the FeNi-PZT-FeCuNiSiB composite. For comparison, Figure 40 shows the measured ME voltage coefficients of symmetric FeNi-PZT-FeNi trilayered composite (a), symmetric FeCuNiSiB-PZT-FeCuNiSiB trilayered composite (b), and asymmetric FeNi-PZT-FeCuNiSiB trilayered composite (c), as the function of frequency (f) in the range of 1−200 kHz at $H_{dc} = 46$ Oe. For

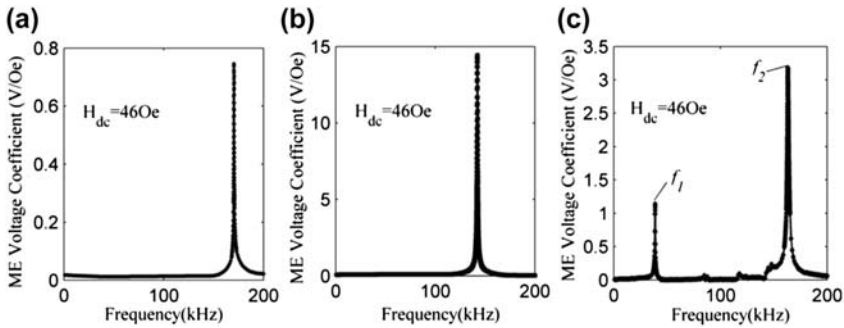

FIGURE 40 The dependence of the magnetoelectric voltage coefficient on the magnetic field frequency (f) at Hdc = 46 Oe for the FeNi-PZT-FeNi trilayer (a), FeCuNiSiB-PZT-FeCuNiSiB trilayer (b), and FeNi-PZT-FeCuNiSiB trilayer (c). f_1 and f_2 are the resonance frequencies of the FeNi-PZT-FeCuNiSiB trilayer. *Reprinted from Chen et al. (2015a). Copyright 2015, with permission from Elsevier.*

the symmetric FeNi-PZT-FeNi and FeCuNiSiB-PZT-FeCuNiSiB trilayers, only one resonance peak appears at a longitudinal frequency higher than 100 kHz. However, for the asymmetric FeNi-PZT-FeCuNiSiB trilayer two remarkable resonance peaks are observed: one at the bending resonance frequency $f_1 = 38.8$ kHz and the other at the longitudinal resonance frequency $f_2 = 163.2$ kHz, respectively. The magnetic field frequency dependence of ME voltage coefficient of the FeNi-PZT-FeCuNiSiB trilayer is distinct from those of FeNi-PZT-FeNi and FeCuNiSiB-PZT-FeCuNiSiB trilayers. This can be attributed to the fact that the different magnetostriction properties of FeCuNiSiB and FeNi lead to the asymmetric stress distribution in the FeNi-PZT-FeCuNiSiB composite. Correspondingly, the additional bending resonance mode appears. The result provides the possibility of implementing FeNi-PZTeF-CuNiSiB trilayers in multifunctional devices with multifrequency operation.

It is also possible to achieve an enhancement of the magnetoelectric effect using electromechanical shear modes. In this case the strength of the magnetoelectric interactions in a magnetostrictive-piezoelectric film on a substrate, in the electromechanical region, is weaker than for thick film bilayers due to the strong clamping effects of the substrate.

5.5 Magnetic Resonance

Magnetoelectric composites also offer important applications in the microwave range, as electrically tunable microwave phase shifters, devices based on ferromagnetic resonance, magnetically controlled electro−optical and/or piezoelectric devices, and electrically readable magnetic (ME) memories (Bichurin and Petrov, 2014). In this frequency range, the magnetoelectric effect reveals itself as a change in the magnetic permeability under an external electric field. In a magnetoelectric composite of ferrite and piezoelectric phases, the electric field can induce a shift of the ferromagnetic resonance field, when using frequencies corresponding to ferromagnetic resonance range (GHz). Figure 41 shows the calculated electric-field dependence of the magnetic susceptibility at 9.3 GHz for bilayers of lithium ferrite−lead zirconate titanate (LFO-PZT), nickel ferrite−lead zirconate titanate (NFO-PZT), and yttrium iron garnet−lead zirconate titanate (YIG-PZT). The static magnetic field H corresponds to the resonance field for $E = 0$ (Bichurin et al., 2002).

5.6 Magnetoacoustic Resonance

Very strong magnetoelectric interactions occur in a single-crystal ferrite−piezoelectric bilayer when the electromechanical and ferromagnetic resonances overlap. In such bilayers, the magnetoelectric interactions are mediated by mechanical strain, and the theory predicts efficient transfer of energy

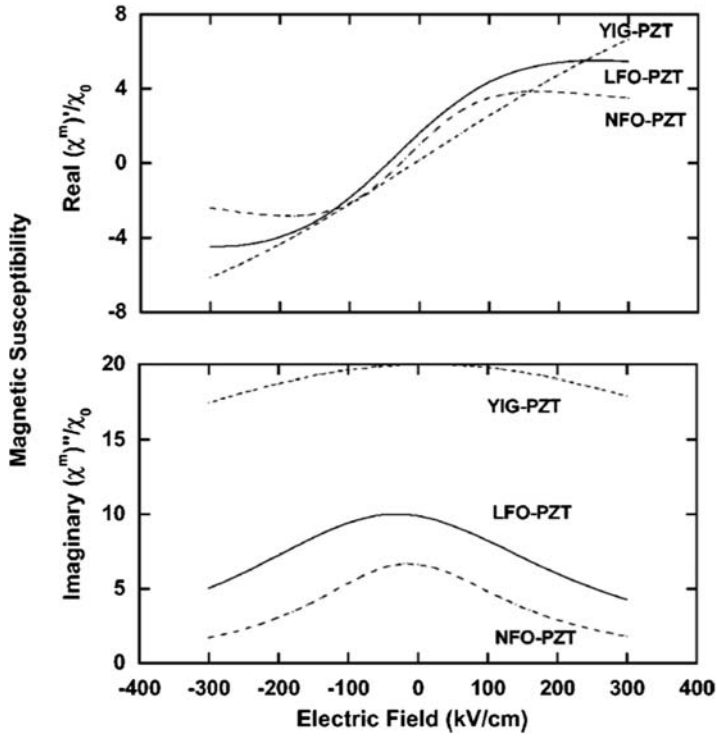

FIGURE 41 Calculated electric-field dependence of the real and imaginary parts of magnetic susceptibility at 9.3 GHz for bilayers of lithium ferrite–lead zirconate titanate (LFO-PZT), nickel ferrite–lead zirconate titanate (NFO-PZT), and yttrium iron garnet–lead zirconate titanate (YIG-PZT). The static magnetic field H corresponds to the resonance field for $E = 0$. *Reprinted with permission from Bichurin et al. (2002). Copyright 2002 by the American Physical Society.*

between phonons, spin waves, and electric and magnetic fields at magnetoacoustic resonance. According to the theory, ultrahigh magnetoelectric coefficients, on the order of 80–480 V/cm Oe at 5–10 GHz, are expected for nickel ferrite–PZT and yttrium–iron garnet–PZT bilayers. The effects of exchange interactions on magnetoacoustic resonance are included. Both the direct magnetoelectric effects and electric field-induced magnetic excitations are important. The magnetoacoustic resonance is also of importance for the realization of multifunctional magnetoelectric nanosensors/transducers operating at microwave frequencies. The bilayer composite is schematically shown in Figure 42, with ferrite and piezoelectric single crystal layers. The ferrite layer is supposed to be in a saturated single-domain state. The bias field is assumed to be applied perpendicular to the sample plane. This state has two important advantages. First, when domains are absent, acoustic losses are minimal. Second, the single-domain state under ferromagnetic resonance

FIGURE 42 Two-layer structure on the basis of single crystal phases.

provides the conditions necessary for achieving a large effective susceptibility (Bichurin and Petrov, 2014).

Due to a microwave electric field and to magnetoelectric interactions in a ferrite–piezoelectric bilayer magnetic excitations can occur and the magnetic response can be described in terms of magnetoelectric susceptibility. A novel technique has been proposed for determining these magnetic excitations in an yttrium iron garnet (YIG)–lead zirconate titanate (PZT) nano-bilayer, where it is assumed that the sample is positioned at the maximum of the microwave electric field (Bichurin and Petrov, 2014)

From the magnetoelectric interactions, an induced microwave magnetic field (parallel to the electric field) will result and, therefore, it will lead to magnetic excitations in the bilayer. Such magnetic excitations originate from the elastic modes in the piezoelectric component. These acoustic modes would, in turn, excite coupled magnetoelastic modes in the ferrite due to the magnetoelectric coupling. The excitations are standing waves along the thickness of the sample and the wavelength is determined by the thickness of the PZT and the YIG, and also by materials parameters. These coupled magnon–phonon modes will be in the microwave region of the electromagnetic spectrum for YIG. Thus the focus here is high frequency magnetic excitations, including ferromagnetic resonance and magnetoelectric susceptibility in a ferrite–ferroelectric bilayer. Traditional ferromagnetic resonance at high powers in a ferrite will lead to nonlinear effects such as saturation of the main resonance and subsidiary absorption. The idea here is to eliminate those effects by locating a bilayer at the position of the maximum of the radiofrequency electric field (Bichurin and Petrov, 2014).

5.7 Influence of Type of Connectivity and Electrical Resistance on the Magnetoelectric Effect

In Fuentes-Cobas et al. (2011), a brief discussion of connectivity in laminate, particulate, fibrous, and interpenetrating composites was carried out, and readers are advised to review it.

The type of connectivity and the electrical resistance of the composite component phases can impact on the strength of the magnetoelectric effect. As an example, cobalt ferrite ($CoFe_2O_4$)–barium titanate ($BaTiO_3$) biphasic

composites with (3−0) connectivity ($BaTiO_3$ grains in a $CoFe_2O_4$ matrix), prepared by a combination of spark plasma sintering and annealing, were compared with a conventionally sintered sample with the traditional (0−3) connectivity ($CoFe_2O_4$ grains in a $BaTiO_3$ matrix). An improvement of the magnetic properties in comparison to the conventionally sintered ceramics was achieved, while the good ferroelectric characteristics were retained. However, the converse magnetoelectric effect was weaker in the SPS sample than in the conventionally sintered one. This was mainly related to the larger leakage current in the former sample preventing efficient electrical poling of the piezoelectric component in the composite (Etier et al., 2015).

Even if the connectivity type does not change, the magnetoelectric effect can be enhanced by only increasing the electrical resistivity in the magnetostrictive phase, because a high electrical resistance in the composite components can decrease the leakage currents, which allows a better polarization of the piezoelectric component. So, in Dipti et al. (2015) an enhancement in the value of the magnetoelectric coupling coefficient, α, was observed in lead zirconate titanate (PZT)−cobalt ferrite (CFO) particulate composites, prepared by a solid state reaction method, when using a small amount of high resistive nickel-substituted cobalt ferrite (CNFO) instead of pure cobalt ferrite (CFO) (see Figure 43). The ferroelectric material was near the morphotropic phase boundary (MPB). The value of α was found to be 3 times (855 μV/(cm·Oe)) in composites of PZT and CNFO as compared to composites of PZT and pure cobalt ferrite (298 μV/(cm·Oe)). This enhancement in α was correlated with an increased electrical resistivity of CFO due to substitution of Ni at Co-site.

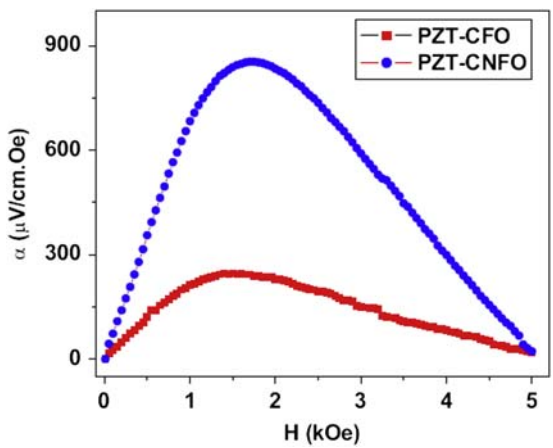

FIGURE 43 Comparison of magnetoelectric coupling in PZT−CFO and PZT−CNFO composites. *Reprinted from Dipti et al. (2015). Copyright 2015, with permission from Elsevier.*

6. APPLICATIONS OF MAGNETOELECTRICITY

6.1 Microwave and Millimeter-Wave Applications of Magnetoelectric Composites

A new family of dual E- and H-tunable microwave and millimeter-wave signal processing devices is based on the strain-mediated high-frequency ME coupling and on the hybrid spin-electromagnetic modes in ferromagnetic/ferroelectric composites. In these high frequency devices the ferromagnetic phases are, in general, low-loss ferrites, such as single-crystals or liquid phase epitaxy (LPE) grown films of yttrium iron garnet (YIG) and single-crystal nickel ferrite (NFO), lithium ferrite (LFO), Y-type hexagonal ferrites, and M-type hexagonal barium–aluminum and strontium–aluminum ferrites, and the ferroelectric phases are lead zirconate titanate (PZT), lead magnesium niobate–lead titanate (PMN-PT), and lead zinc niobate–lead titanate (PZN-PT). Most of these devices are based on ferromagnetic resonance (FMR) in a layered ferrite–ferroelectric composite. For studies on the converse magnetoelectric effects in multiferroic composites the FMR is a powerful tool: an electric field E applied to a ferrite–ferroelectric composite produces a mechanical deformation in the ferroelectric phase, which in turn is coupled to the ferrite, resulting in a shift in the resonance field. From data on the resonance field shift dH_E or frequency shift df_E versus E, information could therefore be obtained on the nature of the converse magnetoelectric coupling. The effect also opens up the possibility of novel voltage-tunable ferrite signal-processing devices. The converse magnetoelectric effect takes place in ferrite–ferroelectric layered structures when the phases are tightly bound, that is, when the mechanical stress created in one is transferred to the second. There are, however, other ME phenomena that do not require bonding between the layers and take place simply due to the proximity of two materials having different dielectric and magnetic properties. An example of such a phenomenon is the formation of hybrid spin-electromagnetic waves in the layered structures. Theoretical models for wave propagation in ferromagnetic–ferroelectric slabs predict intensive hybridization between the electromagnetic waves propagating in the ferroelectric film and the spin waves propagating in the ferromagnetic film. Also, the theory shows that the dispersion characteristics of the hybrid waves can be tuned with an electric field or a magnetic field. Both, the converse magnetoelectric effect at FMR and the hybrid waves in multiferroic composites are of importance for dual E- and H-tunable microwave and millimeter-wave devices (Srinivasan et al., 2015).

Tunable microwave devices are widely used in radar, telecommunication, and RF devices. One class of such devices is based on ferrites. In particular, resonators fabricated from yttrium iron garnet (YIG) films are attractive due to their planar geometry, small size (area on the order of several square

millimeter), and high Q-factor (up to 4000). Their resonance frequency could be tuned over a wide frequency range (0.5−12 GHz) through changes in the magnetic permeability by varying the bias magnetic field created by an electromagnet. But such "magnetic" tuning is relatively slow and is associated with large power consumption. Another class of tunable microwave devices is based on ferroelectric materials. The tuning of such devices is realized by applying an electric field that reduces the dielectric permittivity of the ferroelectric material. Advantages of this "electrical" tuning are fast resonant frequency adjustment and low power consumption because ferroelectric elements, essentially, draw zero static current. But ferroelectric devices in general have low Q and high insertion loss. The multiferroic composites provide a new promising technology for tunable microwave and millimeter-wave devices, which combines the advantages of ferrite and ferroelectric devices. The devices are based on converse magnetoelectric effect or the excitations of hybrid spin-electromagnetic waves in ferrite−ferroelectric layered structures. Such devices are dual tunable, with electrical tuning realized through the application of an electric field to the ferroelectric layer, while the magnetic tuning is realized through the application of a bias magnetic field (Srinivasan et al., 2015).

An electric field-tunable microwave resonator based on yttrium iron garnet (YIG)−lead zirconate titanate (PZT) is described in Fetisov and Srinivasan (2006). This device is based on ferromagnetic resonance for YIG and the tunability is accomplished through magnetoelectric interactions (Fetisov and Srinivasan, 2006). The device is schematically shown in Figure 44.

A 15-μm-thick liquid phase epitaxy grown yttrium iron garnet (YIG) film on a (111) GGG substrate having lateral dimensions 1 × 2.2 mm was bonded to a ceramic PZT plate (4 × 4 × 0.5 mm) coated with 5-μm-thick silver electrodes on both sides, using fast-dry epoxy. The YIG film had a saturation magnetization of 1750 G and a ferromagnetic resonance line width of ∼0.6 Oe at 5 GHz. The bilayer was placed on a microstrip transducer (50 μm × 3 mm) fabricated on an alumina substrate from the gadolinium gallium garnet (GGG) substrate side (Özgür et al., 2009). Microwave measurements were carried out using a vector network analyzer. A standard calibration procedure was performed before measurements. A continuous wave input signal with $f = 2-10$ GHz and power $P\text{in} = 0.1$ mW was applied to the microstrip transducer. Low input power was chosen to prevent heating of the sample due to power absorption at FMR. Profiles of reflected power $P_{\text{ref}}(f)$ versus f were recorded for a series of H and E (Fetisov and Srinivasan, 2006). For an electric field of ±10 kV/cm applied across the PZT plate, the ferromagnetic resonance peak shifted by up to 18 and 25 MHz for a magnetic field bias parallel and perpendicular, respectively, to the bilayer plane, an order of magnitude higher than the absorption width of the resonator (3.4 MHz at

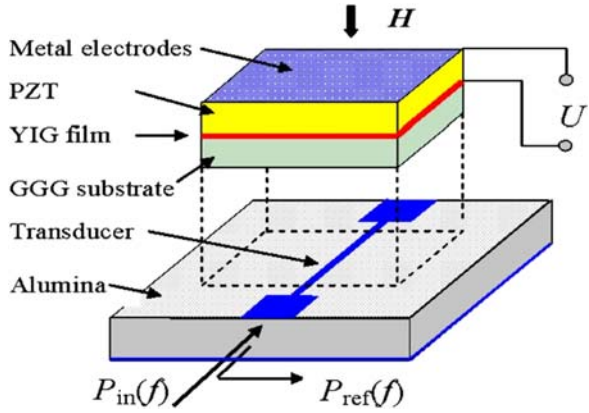

FIGURE 44 Diagram showing a microstripline resonator with a bilayer of lead zirconate titanate (PZT) bonded to (111) yttrium iron garnet (YIG) film on gadolinium gallium garnet (GGG) substrate. *Reprinted with permission from Fetisov and Srinivasan (2006). Copyright 2006, AIP Publishing LLC.*

3 dB). The YIG-PZT bilayer structures could form the basis for rapid, electric field tunable, passive microwave resonators, and filters (Fetisov and Srinivasan, 2006; Özgür et al., 2009).

6.2 Sensor Applications of Magnetoelectric Composites

Figure 45 shows the evolution of magnetoelectric materials in the past century from single-phase compounds to particulate composites, to laminated composites, and finally to micro-/nano-thin films (Wang et al., 2014).

Applications in information storage and spintronics have been the driving force in research in single-phase magnetoelectric materials. However, a high inherent magnetoelectric coupling, especially above room temperature, has not yet been found in single-phase materials as most of them have low Curie temperatures. These difficulties have been circumvented by forming multiphase ME composites of ferromagnetic and ferroelectric components that can be electromagnetically coupled by stress mediation. But the relatively low magnetoelectric coefficients and high dielectric losses make particulate composites technologically challenging for sensor and other applications. These limitations were finally overcome in 2001 by using laminate, instead of particulate composites. Several kinds of magnetoelectric laminate composites have been experimentally and theoretically investigated. The value of the magnetoelectric coupling in laminated composites is determined by three issues: (i) the basic material parameters of the constituent phases (dielectric constant, magnetic permeability, elastic stiffness, and the piezoelectric and piezomagnetic coefficients); (ii) the volume/thickness ratio of the constituent

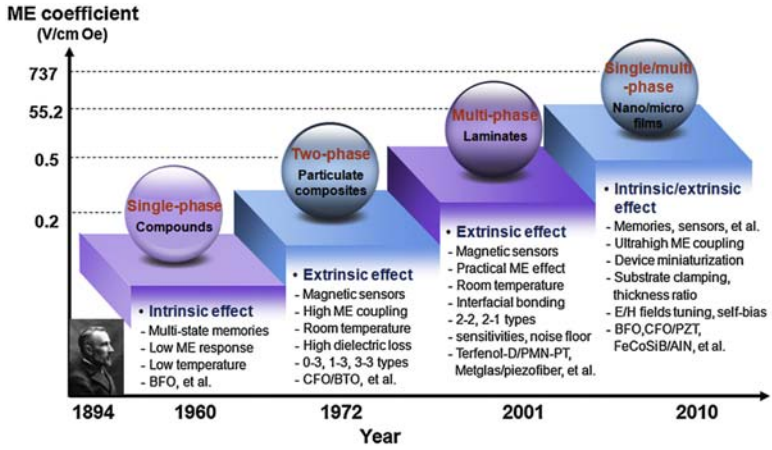

FIGURE 45 Evolution on the development of ME materials: from single-phase compounds to multiphase ferromagnetic/ferroelectric composites and from bulk laminates to micro-/nano-thin films. The main applications, advantages and/or disadvantages, research emphasis, or challenges of each generation are also summarized in this figure. *Reproduced from Wang et al. (2014) under a Creative Commons license, Copyright 2014 Elsevier. http://dx.doi.org/10.1016/j.mattod.2014.05.004.*

layers; and (iii) the operation mode (i.e., orientation of the constituent phases and an applied magnetic field). To date, the largest magnetoelectric coefficients and the highest sensitivity to magnetic field variations correspond to the multi-push−pull configuration of magnetoelectric laminates, consisting of magnetostrictive Metglas alloys and piezofibers with ID-electrodes. It can be considered a milestone in the development of magnetoelectric materials for magnetic sensor applications. Device miniaturization and component connectivity at the atomic level have stimulated the development of magnetoelectric micro-/nano-thin based in advanced thin-film growth techniques. Most of the research activity in magnetoelectric thin films is motivated by promising applications in electric-write/magnetic-read memories and spintronics. The sensing capabilities of a magnetoelectric sensor to magnetic field variations are determined by both the output magnetoelectric signal in response to an incident magnetic field and the intrinsic/extrinsic noise generated in the absence of an incident field. Moreover, the equivalent magnetic noise floor is influenced by the properties of the magnetoelectric laminates and the parameters of the detection circuits. Accordingly, the noise sources and their corresponding contributions to the total equivalent magnetic noise must be considered. Based on these results, the detection circuitry and laminate design can be optimized to reduce the equivalent magnetic noise floor (Wang et al., 2014).

6.3 Current Sensors

A current sensor is a system or device that can measure the magnitude of an electrical current in a cable/wire under either AC or DC conditions. Usually the current sensors encompass many aspects of physics and electronics. Based on their working mechanism, there are mainly four types of electrical current sensing techniques: 1) Hall effect, 2) induction transformer, 3) resistive shunt, and 4) Rogowski coil sensor. In Table 4 a comparison of these different current sensing technologies is given (Zhou and Priya, 2015)

Driven by the need for improved sensitivity, smaller size, and compatibility with electronic systems, the technology for sensing current has evolved. However, none of the abovementioned current sensors satisfy all the needs related to self-powered, miniature size, high performance, low detection limits, reliability, and cost-effectiveness. The development of a compact, low-noise, and low-cost passive current sensor is technologically important and much needed for a variety of electronic systems. Magnetoelectricity (ME) composites can directly generate an electric signal in response to the external magnetic field, leading to a passive nature without the need of external power sources. In addition, by optimizing the composite materials and configurations, it can produce significantly large voltage and sensitivity over a wide range of frequency. Therefore, the development of ME composites and devices for current/magnetic field sensing applications is technologically important. The development of ME current sensors can be characterized by the following aspects: (1) sensing mechanisms, sensor designs, and challenges of typical ME-sensing elements; (2) development of novel self-biased ME composites that can be used as ME passive current sensors in the absence of a DC magnetic field; (3) development of ME transformers that can be used over a wide frequency range of magnetic signals based on their tunable features; and (4) classification of magnetic noises and corresponding noise-reduction methods. ME composites

TABLE 4 Comparison between Different Current Sensing Technologies

Sensing Type	Hall Sensor	Inductive Sensor	Resistance Shunt	Rogowski Coil
Cost	High	Medium	Very low	Low
Linearity	Poor	Fair	Very good	Very good
High current capacity	Good	Good	Very poor	Very good
Power consumption	Medium	Low	High	Low
Output variation with temperature	High	Low	Medium	Very low

as magnetic field detection sensors have attracted lots of attention due to their simple implementation mechanism. Operation of conventional ME composites requires two input components: a magnetic DC bias and a magnetic AC field. Either of these two components can be detected by providing one of the components, leading to a magnetic sensor for detecting AC or DC fields. Since the strength of the magnetic field depends on the current I in the wire, the electric current can be monitored by detecting the corresponding magnetic flux. Typical conventional ME composites-based current sensors can be of rectangular-shaped, ring-type, and polymer-based flexible types. Although these current sensors, based on conventional ME composites, provide great potential for practical sensing application, most of them require an external DC magnetic bias field to obtain an optimum ME response and high current sensitivity. Considering the composition variation and geometry change, one can tune the optimum DC bias as low as several Oe. However, it is still a requirement to use a permanent magnet or electromagnet to provide DC magnetic bias, which, in turn, is a disadvantage for sensor implementation and miniaturization. Therefore, it is necessary to eliminate these limitations from DC bias. Novel designs of self-biased ME composites can provide a giant ME coefficient with large tunable ME coefficients at zero bias (Srinivasan et al., 2015)

6.4 Energy Harvesting Applications of Magnetoelectric Composites

The performance, capabilities, and deployment of wireless sensor networks and remote monitoring devices have been rising. This rapid proliferation of wireless sensor networks is related to the significant progress being made in complementary metal-oxide-semiconductor (CMOS) electronics that has brought down the power requirements considerably. Energy harvesters are being developed to meet the power requirements of the wireless sensor networks and remote monitoring devices in order to enhance the lifetime and limitations of conventional batteries. There are many different sources available for energy harvesting, including solar radiations, thermal gradients, vibrations, magnetic fields, ocean waves, and wind. Vibration energy harvesting has been pursued both as an alternative and as a supplement to the batteries, and between 2000 and 2010, there has been a surge in the number of publications in this area. In order for vibration energy harvesting to become practical, the size and weight of the harvester should be compatible with the mm-scale electronics and sensors, and the resonance characteristics of the harvester must be tailored to match the low natural frequencies and accelerations inherent in most vibration sources. Further, the performance of vibration energy harvesting devices could be improved by simultaneously harvesting the surrounding magnetic fields available that can be converted into electricity through magnetoelectric (ME) material/devices, that is, ME energy harvesters

that operate in dual mode, converting vibrations and magnetic field into electricity (Srinivasan et al., 2015).

In Dai et al. (2009) an energy harvester is described that converts ambient mechanical vibration into electrical energy employing a Terfenol-D/PZT/Terfenol-D laminate magnetoelectric transducer. As shown in Figure 46, the harvester uses four magnets arranged on the free end of a cantilever beam. The magnets produce a concentrated flux gradient in the air gap, and the magnetoelectric transducer is placed in the air gap between the magnets. When the harvester is excited, the magnetic circuit moves relative to the magnetoelectric transducer. The ME transducer undergoes magnetic field variations and produces a power output. Dai et al. have also developed an analytical model to analyze the nonlinear vibration and electrical-output performances of the harvester.

Figure 47 shows theoretical and experimental power versus load resistance when the prototype is excited by the shaker at 1 g acceleration and at resonant frequency. It can be seen from Figure 47 that the theoretical maximum output power reaches 1102.6 μW across a 823.5 kΩ resistor, and the experimental maximum output power reaches 1055.1 μW across a 564.7 kΩ resistor. The output power density of the prototype is 0.472 mW/cm^3 when only the volume of the cantilever beam, magnetic circuit, and transducer are considered, and is 6.13 mW/cm^3 when only the volume of the ME transducer is calculated.

6.5 Spintronic Applications of Magnetoelectric Composites

Multiferroic materials and devices have attracted interests due to the strong magnetoelectric (ME) coupling with unique functionalities and superior

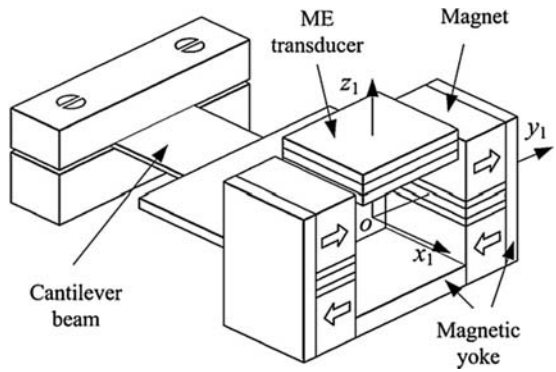

FIGURE 46 Schematic diagram of the proposed vibration energy harvester. Hollow arrows represent the magnetic directions of magnets. *Reprinted from Dai et al. (2009). Copyright 2009, with permission from Elsevier.*

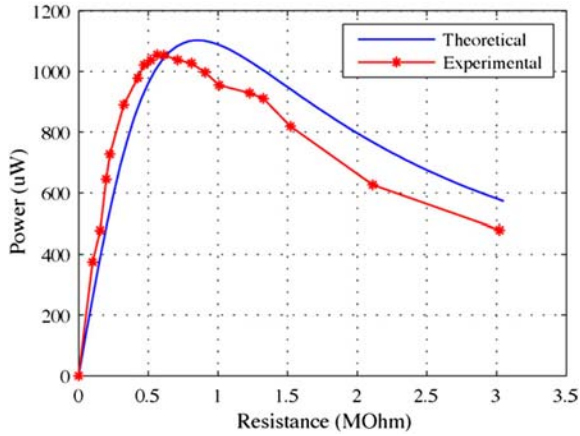

FIGURE 47 Theoretical and experimental power versus load resistance. *Reprinted from Dai et al. (2009). Copyright 2009, with permission from Elsevier.*

performance characteristics. Strong ME coupling has been demonstrated in a variety of multiferroic heterostructures, including bulk magnetic slab on ferro/piezoelectric, magnetic thin film on ferro/piezoelectric slab, thin film multiferroic heterostructures, and so on. The strong ME coupling offers great opportunities for achieving voltage control of spintronics devices with low energy consumption. In traditional magnetic materials-based magnetic random access memories (MRAM) devices, the binary information is stored as magnetization. The high coercivity of the hard ferromagnetic element requires a large magnetic field for switching the magnetic states, which consumes large amount of energy. In the modern MRAM information writing process, spin-torque technique is utilized by passing through a spin polarized current directly to the magnets to minimize the large energy for generating the magnetic field. However, either method is able to decrease the energy consumption to a decent level. With the presence of multiferroic or ME materials, spin is controlled by the electric field, which opens new opportunities for voltage control of spintronic devices with ultralow energy consumption. For artificial multiferroic or ME heterostructure, different coupling mechanisms are utilized for the demonstration of the voltage control of magnetism in spintronics: (1) strain-mediated ME coupling on the ferroelectric−ferromagnetic interface, where the magnetism is modified by the piezostrain induced by ferroelectric slab or thin film due to its piezoelectricity; (2) charge-mediated ME coupling on the ferroelectric−ferromagnetic or dielectric−ferromagnetic interface; and (3) exchange coupling between antiferromagnetic, ferroelectric, and ferromagnetic phases (Srinivasan et al., 2015).

6.6 Magnetoelectric Composites for Medical Application

The underlying principle behind the magnetoelectric (ME) laminate sensors is the magnetic−mechanical−electrical coupling, where a voltage proportional to the applied magnetic field arises due to a giant elastic or mechanical coupling. When a magnetic field H is applied to the magnetostrictive layer, a mechanical strain is generated in that layer and then, this strain is transferred to the piezoelectric layer, thus producing an electric field E via piezoelectricity. This phenomenon could be utilized in a variety of ways to address some of the challenges and needs in the medical applications.

In wireless endoscopy and brain-imaging applications, ME composites have important potential applications. Endoscopy of the upper and lower gastrointestinal tract is considered to be a routine diagnostic and therapeutic outpatient procedure. Endoscopes are utilized for closer and noninvasive examination of the gastrointestinal tract. They provide diagnosis and therapy of a wide variety of pathologies that originate in the epithelial tissue. Classical gastrointestinal endoscopy involves the insertion of a flexible tube that contains the illumination component, lens/camera visual system, and an additional tube that enables the introduction of medical instruments or manipulators. Nevertheless, the reach and maneuverability of tethered endoscopes is limited. Comprehensive endoscopy of the organs in the digestive system, such as the esophagus, stomach, and small and large intestines is difficult. Only a decade ago, wireless capsule endoscopies were introduced. This innovation leveraged the advances in telemetry, miniature optics, and microelectronics. Patients are far more receptive to undergo a wireless capsule endoscopies procedure compared to conventional endoscopes since they are far less invasive. Nonetheless, wireless capsule endoscopes come with a major disadvantage over conventional endoscopes because of their passive nature. They cannot be controlled or conduct biopsy. Images are acquired at random locations and orientations as the capsule moves along the gastrointestinal tract. In order to be able to locate where the images of specific lesions are being taken, a high fidelity tracking of the wireless capsule endoscopies is required. ME composites can be potentially tailored for meeting the requirements of the localization of wireless capsule endoscopy. To generate energy on demand, one can also envision incorporating a magnetic field energy harvesting component into the capsule that can be used to recharge the battery. Thus, if power in the system is less than the threshold, then one can just apply the AC magnetic field from outside the body (as simple as shaking a magnet by hand) and recharge the internal battery (Srinivasan et al., 2015).

Another important development taking place is the improvement in the tools that can be used to understand the structure and function of the brain. Advances in magnetometers and signal processing have allowed imaging of

the brain with significantly high resolution. The brain performs several bodily functions, such as maintaining body temperature, blood pressure, heart rate, and breathing, collection and processing of information around the person using various sensing organs (eyes, ears, nose, etc.), coordination of the physical motion during walking, talking, standing, or sitting, emotions, reasoning, and imagination. The brain is made of approximately 100 billion nerve cells called neurons, which gather and transmit electrochemical signals. Neurons within the brain may extend up to few millimeters and have different shapes depending on the function. For example, motor neurons that control muscle contractions have a cell body on one end, a long axon in the middle, and dendrites on the other end; sensory neurons have dendrites on both ends, connected by a long axon with a cell body in the middle. The structure of the neurons controls the intraneuronal electric currents that generate the extracranial magnetic fields. Thus, detection of brain magnetic fields can allow us to investigate the neuronal activity in healthy and diseased brains. The key requirements for magnetic field sensors in this application are (1) sensitivity of $\sim fT/\sqrt{Hz}$ at low frequencies (10^{-3} Hz); (2) ambient temperature and wide bandwidth operation; and (3) small size, to promote portable imaging array systems. These requirements can be met by the advances being made in the synthesis and optimization of the ME composites (Srinivasan et al., 2015).

Magnetoelectric composites have also shown the capability as ultrasensitive magnetic field sensors in the picotesla regime and the possibility of vector-field measurement. These features make them interesting candidates for noninvasive, high spatial resolution, and deep region medical imaging like magneto-encephalography or -cardiography (MEG, MCG). Though state-of-the-art ME sensors are centimeter-sized and are not suitable for dense arrays needed for MEG or MCG measurements, micromachined resonant ME sensors promise miniaturized devices with high sensitivity. For the first time, MEMS sensors based on magnetoelectric composites with vacuum encapsulation using wafer-level packaging technology were presented in Marauska et al. (2013). The presented micro magnetoelectric sensor showed the highest magnetoelectric coefficient of 2380 (V/m)/(A/m) measured so far with a corresponding sensitivity of 3800 V/T. This is competitive with state-of the art, nonencapsulated, centimeter-sized magnetoelectric sensors. The measured resolution of 30 pT and the noise floor of $27pT/\sqrt{Hz}27$ show the capability for sensitive biomagnetic sensing. Improvement of the device vacuum should result in a significantly higher Q-factor and ultralow noise levels. Compared to other micro vector-field magnetic sensors, the magnetoelectric composites in micromachined devices act as ultrasensitive magnetic field sensors. Figure 48 shows photographs of diced wafer pair and single sensor element with, ME cantilever, etch groove, bond frame, and bond pads (Marauska et al., 2013).

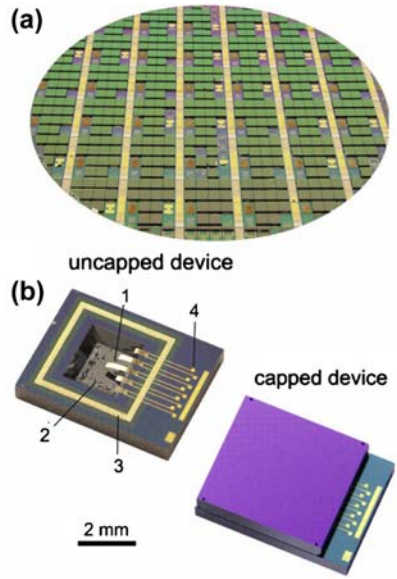

FIGURE 48 Photographs of diced wafer pair (a) and single sensor element (b) with (1) ME cantilever, (2) etch groove, (3) bond frame, and (4) bond pads. *Reprinted from Marauska et al. (2013). Copyright 2013, with permission from Elsevier.*

6.7 Magnetoelectric Nanoparticles to Enable Field-Controlled High-Specificity Drug Delivery to Eradicate Ovarian Cancer Cells

The cell membrane is electrically polarizable. Thus, its properties can be modified by the action of an external electric field. This makes possible the manipulations of its pores by an electric field. This phenomenon is known as *electroporation* (Guduru et al., 2013).

There is a difference between the electrical properties of the membranes of healthy cells and cancer cells: the latter require a lesser electric field to open its pores. This property can be used to carry specialized drugs through the membrane into the cancer cells (without affecting the healthy ones).

The way to control the release of drugs is by using magnetoelectric nanoparticles (MEN) made of nanocomposites of $CoFe_2O_4/BaTiO_3$ with a drug within them (core−shell arrangement).

For this purpose, externally from a certain distance, a magnetic field is used to control the electrical properties of the particle. Thus, the MENs can generate localized electric fields strong enough to open the pores of the cancer cell's membrane and let them in, permitting the releasing of the drug inside the target (Guduru et al., 2013) (Figure 49).

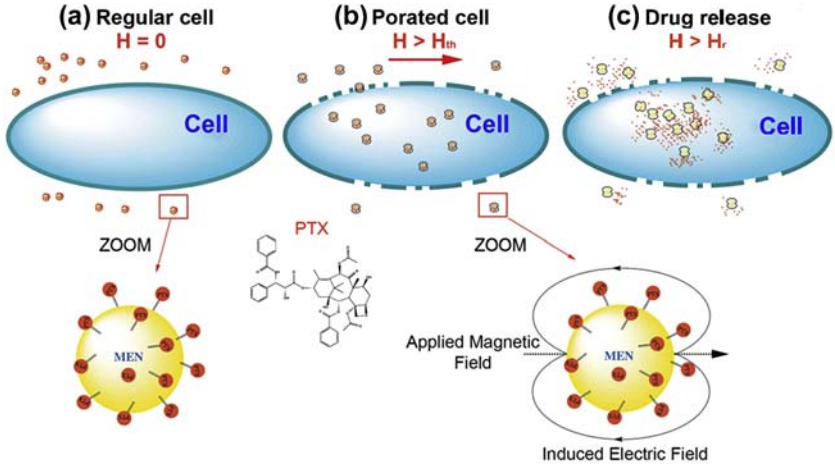

FIGURE 49 MENs as field-controlled nano-electroporation sites to let the drug through the cancer cell membranes. *Reproduced from Guduru et al. (2013) under a Creative Commons license. Copyright 2013 Nature Publishing Group. http://dx.doi.org/10.1038/srep02953.*

6.8 Externally Controlled On-Demand Release of Anti-HIV Drug Using Magnetoelectric Nanoparticles as Carriers

Antiretroviral therapy has had great results fighting the HIV virus in general, but has been limited due to the fact that there are areas of the body that cannot be reached by the drugs. Such is the case of brain cells where, due to the inability to cross the blood−brain barrier (BBB), the virus persists (Nair et al., 2013).

To carry a polar-active molecule through this barrier a new idea is to implement a type of material that has not been used before to transport and deliver drugs: MENs, which seek to replace the normally used nanostructured magnetic materials (MN). The difference lies in the fact that, as MENs have the electron spin and the dipole moment intrinsically coupled, the mechanism is energetically more efficient. Better yet, the charge distribution can be regulated by MENs via a magnetic field and, using this same principle, the bonding between the drug (molecule of interest) and the MEN can be controlled.

While transporting the drug, the MEN and the active molecule must be strongly bond; whereas, when liberation is necessary, a stronger magnetic field is applied to break this same bond.

Figure 50 schematically shows how an a.c. magnetic field can generate an electric dipole which debilitates the chemical bond, liberating the drug (Nair et al., 2013).

Figure 51, also from Nair et al. (2013), is a sequence of atomic force microscope images taken during a drug delivery process.

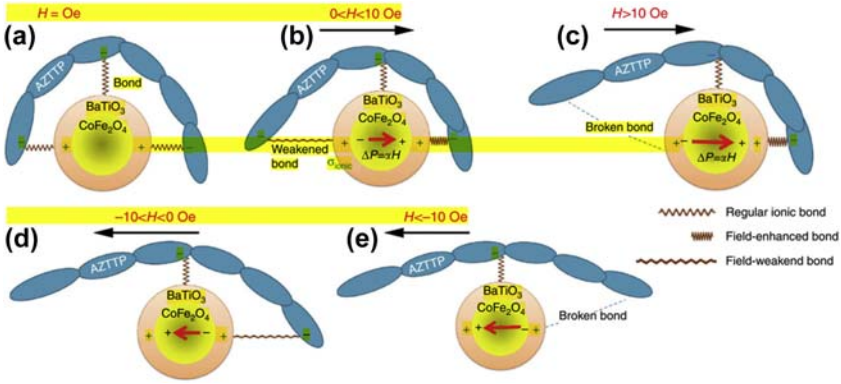

FIGURE 50 Release of a drug by a MEN. *Reprinted with permission from Macmillan Publishers Ltd: Nature Communications (Nair et al., 2013). Copyright 2013.*

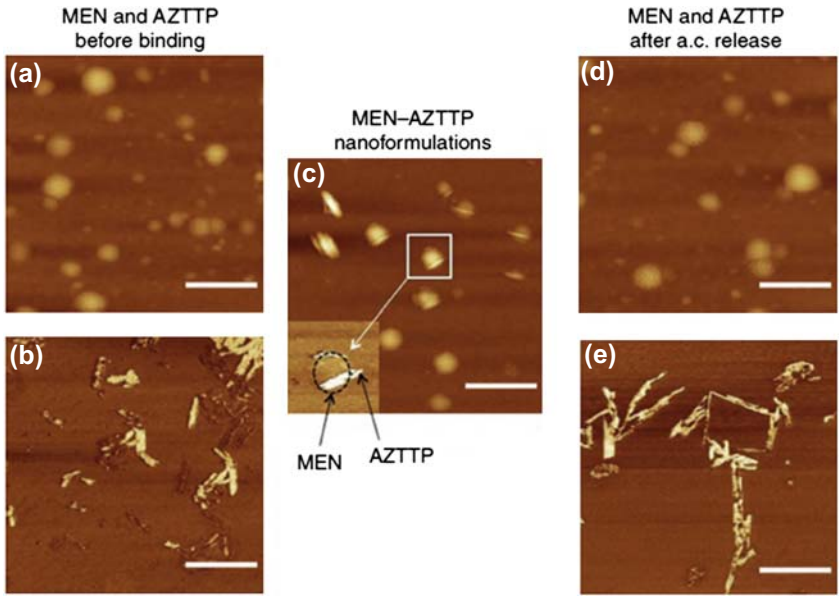

FIGURE 51 Atomic force microscopy of the drug release kinetics. AFM images at the different stages of the release process: (a) MENs and (b) AZTTP chains before the loading (binding) step; (c) AZTTP-MEN nano-formulations after the loading process; (d) MENS and (e) AZTTP after the drug release by a 44-Oe a.c. field at 1000 Hz. Scale bar, 100 nm. *Reprinted with permission from Macmillan Publishers Ltd: Nature Communications (Nair et al., 2013). Copyright 2013.*

APPENDIX: TEXTURE AND PHYSICAL PROPERTIES

Crystallographic Texture

Crystallographic texture refers to the nonrandom distribution of the orientations of crystallites in a polycrystal. The quantitative characterization of texture and the effect of texture on the physical properties of polycrystals are summarized in the present Appendix. For detailed discussions, see Bunge (2013), Kocks et al. (2000), Chateigner (2013), Lutterotti et al. (2004), Fuentes-Cobas and Fuentes-Montero (2008). A number of considerations applicable to properties in general will be given, but focus will be put on the magnetoelectric effect.

The most important statistical descriptor of crystallographic texture is the Orientation Distribution Function (ODF), or $f(g)$, in which g is a crystallite orientation defined in the sample reference frame by three Euler angles: $g = (\phi_1, \Phi, \phi_2)$. The three successive rotations in g bring a given crystallite reference frame K_C colinear to the sample reference frame K_S, that is, $K_S = g \cdot K_C$. The ODF, $f(g)$, is then a function which represents the distribution density of orientations of all crystallites in the sample volume:

$$\frac{dV}{V} = f(g)dg \quad \oint f(g)dg = 1\,, \tag{A1}$$

that is, the density of crystallites whose volume fraction is oriented within the orientation element dg and is normalized to 100% of the volume.

$f(g)$ is not directly measurable. Diffraction experiments (using X-rays, neutrons, electrons) can only access the so-called pole figures (PF), $P_{\mathrm{h}}(\mathbf{y})$, representing the distribution of given crystallographic directions $\mathbf{h} = [hkl]^*$, normal to (hkl) crystallographic planes, and defined by:

$$\frac{dV(\mathbf{y})}{V} = P_h(\mathbf{y})d\mathbf{y} \quad \oint P_h(\mathbf{y})d\mathbf{y} = 4\pi \tag{A2}$$

The pole figures are consequently the volume fraction of crystallites oriented with their normals $\mathbf{h}$ within d$\mathbf{y}$ and are also normalized.

An alternative representation of textures is given by the inverse pole figures (IPF), $R_{\mathbf{y}}(\mathbf{h})$, defined by the relative population of crystal directions $\mathbf{h}$ in a given sample direction $\mathbf{y}$:

$$\frac{dV(\mathbf{h})}{V} = R_y(\mathbf{h})d\mathbf{h} \quad \oint R_y(\mathbf{h})d\mathbf{h} = 4\pi \tag{A3}$$

The following is the Fundamental Equation of Quantitative Texture Analysis:

$$P_h(\mathbf{y}) = \frac{1}{2\pi} \int\limits_{\mathbf{h}//\mathrm{y}} f(g)d\tilde{\varphi}. \tag{A4}$$

This equation represents the fact that each PF (a 2D object) is a projection along a certain path $\tilde{\varphi}$ of the ODF (a 3D object), which of course depends on the crystal and texture symmetry. Standard methods for determining the ODF are based on the measurement of a set of pole figures and the subsequent inversion of Eqn (A4).

A particular sample configuration that is relatively frequent in magnetoelectric materials is the so-called fiber texture. It shows axial symmetry in the orientation distribution. In fiber textures, the IPF corresponding to the polycrystal symmetry axis plays the role of the ODF. Equation (A4) simplifies to the following, known as the Fundamental Equation of Fiber Textures:

$$P_{\mathrm{h}}(\varphi) = \frac{1}{2\pi} \int_0^{2\pi} R_z(\varphi, \psi) d\psi \tag{A5}$$

where φ is the polar angle of the P_{h} PF and ψ is the integrating angle in a reference sphere. For details, see (Fuentes-Montero et al., 2010).

FDO, FP, and FIP are statistical descriptors, with high cognitive and practical value. They provide a global characterization of texture and help to understand the physics of processes and properties. On the other hand, the development of electron microscopy and computer techniques allow today to measure, process, store, and present alternative texture characterizations that are worth to be mentioned.

In particular, scanning electron microscopy has established the method known as orientation image microscopy (IOM) (Lebensohn et al., 2008). This technique is based on electron diffraction and allows the determination of the so-called ***aggregate function*** (Bunge et al., 2000) This descriptor, denoted $g(\mathbf{r})$, specifies the orientation g of the crystallite at each point $\mathbf{r} = (x, y, z)$ in the sample volume. The dependent variable g is defined by the Euler angles $g = (\phi_1, \Phi, \phi_2)$. The aggregate function contains point-by-point information of the size, shape, and orientation of all the crystals in a sample. From it one is able to calculate several texture descriptors such as the size distribution, the ODF, and the misorientation distribution function (Schwartz et al., 2009).

Polycrystal Physical Properties. Voigt, Reuss, and Hill Approximations

By "physical property" we understand the magnitude that links an external action with the response of a given crystal. In symbols:

$$\mathbf{Y} = \mathbf{K} \cdot \mathbf{X} \tag{A6}$$

X represents the applied action, **Y** is the material response, and **K** is the considered property. In general, **X** and **Y** are tensors with respective ranks m and n. The property tensor rank is $r = m + n$. Magnetoelectricity is a second rank, axial tensor, linking polar time-independent electric polarization **P** with axial time-reversible magnetic field intensity **H** and magnetization **M** with electric field intensity **E**.

In a polycrystal, "mean" or "average" action, response and property are given by

$$\langle \mathbf{X} \rangle = \frac{1}{V} \int_{V} \mathbf{X}\, dV \quad \langle \mathbf{Y} \rangle = \frac{1}{V} \int_{V} \mathbf{Y}\, dV \quad \langle \mathbf{K} \rangle = \frac{1}{V} \int_{V} \mathbf{K}\, dV \tag{A7}$$

The weighting factor in (A7) is the ODF:

$$\langle \mathbf{K} \rangle = \int \mathbf{K}(g) f(g) dg \tag{A8}$$

And the ***effective macroscopic polycrystal property*** is the magnitude $\mathbf{K^M}$ that satisfies the following condition:

$$\langle \mathbf{Y} \rangle = \mathbf{K^M} \cdot \langle \mathbf{X} \rangle \tag{A9}$$

Mathematically, the following relationship can be proven (Bunge, 2013)

$$\langle \mathbf{Y} \rangle = \langle \mathbf{K} \rangle \cdot \langle \mathbf{X} \rangle + \frac{1}{V} \int_{V} \Delta\mathbf{K} \cdot \Delta\mathbf{X}\, dV \tag{A10}$$

The *mean* $\langle \mathbf{K} \rangle$, Eqn (A7), represents the *effective macroscopic* property only if the independent variable remains invariant in the sample volume ($\Delta\mathbf{X} \equiv 0$).

Equation (A10) deserves a somewhat detailed analysis. The following considerations illustrate the scenario.

Two different samples may possess the same ODF and exhibit, in an experiment, different macroscopic effective properties. Intercrystalline interactions and macroscopic properties not only depend on the distribution of orientations, but also on crystallites' shapes, sizes, and relative positioning, that is, on sample's *stereography*.

The influence of sample stereography has been treated extensively for elasticity. Figure A.1 (Bunge et al., 2000) illustrates the so-called "*problem of averaging*."

For a polycrystal with a series configuration, the stress can be considered as constant in the sample volume. For this geometry, known as *Reuss* (Reuss, 1929) case, it is advisable to apply the constitutive equation $\boldsymbol{\varepsilon} = \mathbf{s} \cdot \boldsymbol{\sigma}$ ($\mathbf{Y} \rightarrow \boldsymbol{\varepsilon}$ = strain; $\mathbf{K} \rightarrow \mathbf{s}$ = compliance; $\mathbf{X} \rightarrow \boldsymbol{\sigma}$ = stress). As $\Delta\boldsymbol{\sigma} = 0$, the integral in Eqn (A10) vanishes and this leads to Eqn (A9), with $\mathbf{S^M} = \langle \mathbf{S} \rangle$.

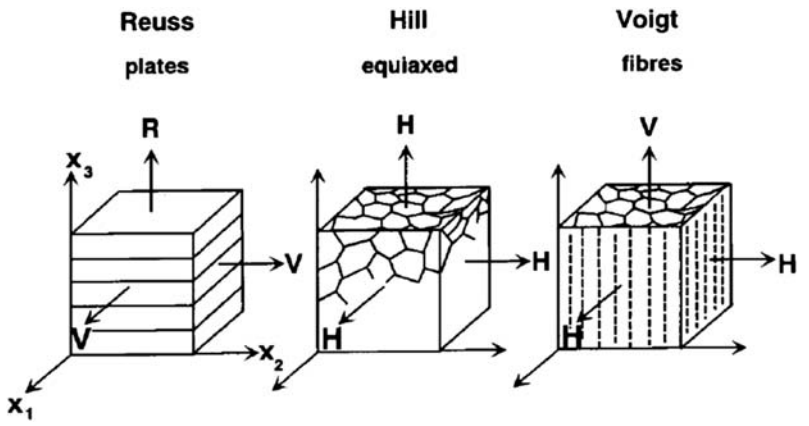

FIGURE A.1 Polycrystal samples with the same ODF can show different macroscopic properties. Reuss case: plates piled in a "series" configuration. Voigt case: columns in "parallel" association. Case Hill: equiaxed crystallites. *Reprinted from (Bunge et al., 2000), Copyright 2000, with permission from Elsevier.*

For parallel configuration, *Voigt* (Voigt, 1928) case, the suitable constitutive equation is $\boldsymbol{\sigma} = \mathbf{c}\cdot\boldsymbol{\varepsilon}$ ($\mathbf{c} = \mathbf{s}^{-1}$ = stiffness). Finally, the so-called *Hill approximation* (Hill, 1952) for $\mathbf{s}$ is:

$$\mathbf{s}^{\mathbf{M}}_{\text{Hill}} \cong \frac{1}{2}\left[\langle \mathbf{s} \rangle + \langle \mathbf{c} \rangle^{-1}\right] \tag{A11}$$

The Voight–Reuss–Hill considerations may be extended to electromagnetic phenomena. The cases of series and parallel combinations of resistors (properties: conductivity and conductivity^{-1} = resistivity) and capacitors (properties: dielectric constant and dielectric constant^{-1} = impermittivity) are well known and the significant observed differences between "series" and "parallel" values coincide with theoretical calculations.

The selection of independent–dependent variables in electromagnetic coupling properties (piezoelectricity, magnetoelectricity, and so on) has been analyzed by Fuentes-Cobas et al. (2013). Coupling properties require an additional consideration, in comparison with elasticity. Moving from Voigt (parallel) to Reuss (series) in elasticity implies permuting the roles of one independent and one dependent variable. Magnetoelectricity (as a coupling property) requires permuting two independent and two dependent variables. It is not as simple as changing compliance to its inverse stiffness. The case of magnetoelectricity, as may be derived from the Maxwell equations, leads to the summary of conditions described in Table A1:

TABLE A1 Invariant Magnitudes in Series and Parallel Configurations

Configuration	Elasticity	Electricity	Magnetism
Series (Reuss)	Stress ($\boldsymbol{\sigma}$)	Electric displacement (**D**)	Magnetic induction (**B**)
Parallel (Voigt)	Strain ($\boldsymbol{\varepsilon}$)	Field intensity (**E**)	Field intensity (**H**)

For a polycrystal with a near-to-Voigt (piled plates) configuration, averaging magnetoelectric tensor $\langle \alpha_{ij} \rangle = \langle dD_i/dH_j \rangle = \langle dB_i/dE_j \rangle$ is a good approximation for $\boldsymbol{\alpha}^{\mathbf{M}}$ ($\boldsymbol{\alpha}^{\mathbf{M}} \approx \langle \boldsymbol{\alpha} \rangle$).

For a Reuss polycrystal (parallel columns) the recommended quantity to be averaged is the *inverse* $\alpha \equiv \boldsymbol{\alpha}'$, $\langle \alpha'_{ij} \rangle = \langle dE_i/dB_j \rangle = \langle dH_i/dD_j \rangle$; $\boldsymbol{\alpha}^{\mathbf{M}} \approx \langle \boldsymbol{\alpha}' \rangle$.

Voigt and Reuss cases represent special situations. In given cases these approximations may be appropriate. In a Voigt polycrystal, if one is interested in the value of the effective $\boldsymbol{\alpha}'^{\mathbf{M}}$, one must calculate $\boldsymbol{\alpha}^{\mathbf{M}}$ and then define $\boldsymbol{\alpha}'^{\mathbf{M}} \equiv (\boldsymbol{\alpha}^{\mathbf{M}})^{-1}$. The average (Eqn (A7)) of $\boldsymbol{\alpha}'$, without calculating the second term on the right side of Eqn (A10) (say, by use of the aggregate function $g(\mathbf{r})$) would not be a correct choice.

The Hill average maybe a good guess in case the researcher ignores the sample stereography (or he knows it is far from series or parallel). One important issue that must be taken into account is the self-consistency of the proposed effective property. The product $\boldsymbol{\alpha}^{\mathbf{M}} \cdot \boldsymbol{\alpha}'^{\mathbf{M}}$ must be equal to the identity matrix. The simple Voigt, Reuss, and Hill averages do not fulfill this condition. As proposed by Bunge et al. (2000), an iterative procedure based on the Hill approximation leads to self-consistency. A mathematical procedure that systematically leads to the required consistency is that of the *geometric mean*, established by Matthies and Humbert (1995). We now present this method.

Geometric Average

Scalars

A zero-order tensor, or scalar b, can always be decomposed into a linear combination of all its N possible values b_k, each of them being associated to a given probability, or weight, w_k. Its arithmetic average is then:

$$\langle b \rangle = \sum_{k=1}^{N} b_k w_k, \quad \text{with} \sum_{k=1}^{N} w_k = 1 \tag{A12}$$

The corresponding geometric mean of this scalar takes the form:

$$\lceil b \rceil = \prod_{k=1}^{N} b_k^{w_k} = \exp(\langle \ln b \rangle), \quad \text{with} \tag{A13}$$

$$\langle \ln b \rangle = \sum_{k=1}^{N} \ln b_k w_k \tag{A14}$$

Second Order Tensor: The Case of Magnetoelectricity

Considering matrices, the previous approach of the geometric mean is not straightforward. For the eigenvalues λ_I of a given matrix α_{ij}, the averaging procedure can be written as the geometric mean:

$$\lceil \lambda_I \rceil = \prod_{k=1}^{N} \lambda_k^{w_{i,k}} \tag{A15}$$

which ensures that $\lceil \lambda_I \rceil = 1/\lceil 1/\lambda_I \rceil = \lceil \lambda_I^{-1} \rceil^{-1}$. For the matrix α_{ij} represented in its orthonormal basis of eigenvectors, it can be shown (Matthies and Humbert, 1995) that:

$$\lceil \alpha \rceil_{ij} = \exp(\langle \ln \alpha \rangle_{i'j'}) \tag{A16}$$

$$= \exp(\langle \Theta \rangle_{ij,i'j'} \ln \alpha_{i'j'}) \tag{A17}$$

In this equation, Θ stands for the transformation applied to α_{ij}, which represents the ME property of a given crystal with orientation g, to bring it coincident to the sample reference frame. Θ then depends on the tensor order, and its average is composed of elements $<\Theta>_{ij}$ given by:

$$\langle \Theta \rangle_{ij,i'j'} = \int_g \Theta_i^{i'}(g) \Theta_j^{j'}(g) f(g) dg \tag{A18}$$

However, except for specific crystal and texture symmetries, neither α_{ij} nor $(\alpha_{ij})^{-1}$ are diagonal, and Eqn (A17) cannot be used in its actual state. In general, one should first diagonalize α_{ij} using an orthonormal basis of eigenvectors $\mathbf{b}_i^{(\lambda)}$, for instance with the ME tensor eigenvalues $\alpha^{(\lambda)}$:

$$\left(\left(bi^{(\lambda)} \right)^{-1} \alpha_{ij} \mathbf{b}_j^{(\lambda)} \right) = \alpha(\lambda) \quad \text{and} \tag{A19}$$

$$\alpha_{ij} = \sum_{\lambda=1}^{3} \alpha^{(\lambda)} \mathbf{b}_i^{(\lambda)} \mathbf{b}_j^{(\lambda)} \text{which extends to} \tag{A20}$$

$$(\ln \alpha)_{ij} = \sum_{\lambda=1}^{3} \ln\left(\alpha^{(\lambda)}\right) \mathbf{b}_i^{(\lambda)} \mathbf{b}_j^{(\lambda)} = \ln \left[\prod_{\lambda=1}^{3} \left(\alpha^{(\lambda)}\right)^{\mathbf{b}_i^{(\lambda)} \mathbf{b}_j^{(\lambda)}} \right] \tag{A21}$$

Now applying the geometric average over orientations (Eq A17 and A18), the macroscopic ME tensor of the polycrystal can be calculated from:

$$\alpha_{ij}^{M} = \lceil \alpha \rceil_{ij} \tag{A22}$$

and $(\ln\alpha)_{i'j'}$ is given by Eqn (A21). However, before calculating the wanted value $\lceil \alpha \rceil_{ij}$, one has to first diagonalize $<\ln\alpha>_{i'j'}$ in order to extract the new eigenvalues and eigenvectors for the oriented polycrystal. The two successive tensor transformations relate to the second order ME tensor character.

The factorial entering the calculation explains the term "geometric mean", in the sense that the oriented polycrystal macroscopic ME tensor is obtained by the mean averaging of the single crystal ME eigenvalues. Similar expressions can be obtained for the macroscopic inverse ME tensor ($\boldsymbol{\alpha}'^{\mathbf{M}}$) which admits as eigenvalues the reciprocal $1/\alpha^{(\lambda)}$. This warrants that the same macroscopic ME properties are obtained using either α_{ij} or its inverse in the geometric mean approach. In other words, the average of the inverse macroscopic property is consistent with the inverse of the average macroscopic property. This may be the reason why this modeling gives rather very good estimates of the elastic properties (Matthies et Humbert, 1995), comparable to ones obtained by more sophisticated models which require larger calculation times.

However we should state here that diagonalization is not always possible dealing with ME tensors. For instance, in the mmm′ magnetic point group, with nonzero components only off diagonal ($LiCoPO_4$ example above), diagonalization is not possible.

ACKNOWLEDGMENTS

Support from Consejo Nacional de Ciencia y Tecnología, México, Projects CONACYT 174391 and 257912, is gratefully acknowledged. Thanks to L. Fuentes-Montero (Diamond Lightsource) for advice in computer-aided representation of magnetoelectric surfaces.

REFERENCES

Ackermann, M.; Lorenz, T.; Becker, P.; Bohaty, L. Magnetoelectric Properties of $A_2[FeCl_5(H_2O)]$ with A = K, Rb, Cs. *J. Phys. Condens. Matter* **2014,** *26,* 506002.

Ahmed, A. A. A.; Talib, Z. A.; Hussein, M. Z. Influence of Sodium Dodecyl Sulfate Concentration on the Photocatalytic Activity and Dielectric Properties of Intercalated Sodium Dodecyl Sulfate into Zn−Cd−Al Layered Double Hydroxide. *Mater. Res. Bull.* **2015,** *62,* 122−131.

Bartkowska, J. A. The Magnetoelectric Coupling Effect in Multiferroic Composites Based on PZT−ferrite. *J. Magn. Magn. Mater.* **2015,** *374,* 703−706.

Behera, D.; Mohanta, A.; Mishra, N. C.; Panigrahi, S. *Intergranular Percolation in Granular YBCO/BaTiO3 Composites,* 2015.

Bichurin, M.; Petrov, V. *Magnetoelectric Effect in Electromechanical Resonance Region. Modeling of Magnetoelectric Effects in Composites;* Springer, 2014.

Bichurin, M. I.; Petrov, V. M.; Kiliba, Y. V.; Srinivasan, G. Magnetic and Magnetoelectric Susceptibilities of a Ferroelectric/Ferromagnetic Composite at Microwave Frequencies. *Phys. Rev. B* **2002,** *66*.

Bichurin, M. I.; Viehland, D. *Magnetoelectricity in Composites;* Pan Stanford Publishing Pte. Ltd, 2011.

Borovik-Romanov, A.; Grimmer, H. *Magnetic Properties. International Tables for Crystallography Volume D: Physical Properties of Crystals;* Springer, 2003.

Brosseau, C.; Castel, V.; Potel, M. Controlled Extrinsic Magnetoelectric Coupling in $BaTiO_3$/Ni Nanocomposites: Effect of Compaction Pressure on Interfacial Anisotropy. *J. Appl. Phys.* **2010,** *108,* 024306.

Bunge, H.-J. *Texture Analysis in Materials Science: Mathematical Methods;* Elsevier, 2013.

Bunge, H.; Kiewel, R.; Reinert, T.; Fritsche, L. Elastic Properties of Polycrystals—Influence of Texture and Stereology. *Journal Mech. Phys. Solids* **2000,** *48,* 29−66.

Chateigner, D. *Combined Analysis;* John Wiley & Sons, 2013.

Chen, L.; Ping, L.; Yumei, W.; Yong, Z. Resonance Magnetoelectric Effect in an Asymmetric Magnetostrictive/Piezoelectric Trilayered Composite Structure. *J. Alloys Compd.* **2015a,** *646,* 1032−1035.

Chen, X.; Xue, Y.; Lu, Z.; Xiao, J.; Yao, J.; Kang, Z.; Su, P.; Yang, F.; Zeng, X.; Sun, H. Magnetodielectric Properties of Bi 4 NdTi 3 Fe 0.7 Co 0.3 O 15 Multiferroic System. *J. Alloys Compd.* **2015b,** *622,* 288−291.

Cheong, S.-W.; Mostovoy, M. Multiferroics: A Magnetic Twist for Ferroelectricity. *Nat. Mater.* **2007,** *6,* 13−20.

Chu, Y.-H.; Martin, L. W.; Holcomb, M. B.; Ramesh, R. Controlling Magnetism with Multiferroics. *Mater. Today* **2007,** *10,* 16−23.

Coey, J. M. D. *Magnetism and Magnetic Materials;* Cambridge University Press, 2009.

Dai, X.; Wen, Y.; Li, P.; Yang, J.; Zhang, G. Modeling, Characterization and Fabrication of Vibration Energy Harvester Using Terfenol-D/pzt/terfenol-D Composite Transducer. *Sens. Actuators A* **2009,** *156,* 350−358.

Dipti; Juneja, J. K.; Singh, S.; Raina, K. K.; Prakash, C. Enhancement in Magnetoelectric Coupling in PZT Based Composites. *Ceram. Int.* **2015,** *41,* 6108−6112.

Disseler, S.; Oh, Y. S.; Hu, R.; Luo, X.; Lynn, J.; Cheong, S.-W.; Ratcliff, W. Enhanced Multiferroicity in $LuFeO_3$ through Sc Doping. In *APS Meeting Abstracts;* 2015; p 32013.

Dzyaloshinskii, I. A Thermodynamic Theory of "weak" Ferromagnetism of Antiferromagnetics. *J. Phys. Chem. Solids* **1958,** *4,* 241−255.

Dzyaloshinskii, I. Theory of Helicoidal Structures in Antiferromagnets. 1. *Nonmetals. Sov. Phys. JETP* **1964,** *19,* 960−971.

Eckel, S.; Sushkov, A.; Lamoreaux, S. Limit on the Electron Electric Dipole Moment Using Paramagnetic Ferroelectric Eu 0.5 Ba 0.5 TiO 3. *Phys. Rev. Lett.* **2012,** *109,* 193003.

Espinosa-Almeyda, Y.; López-Realpozo, J.; Rodríguez-Ramos, R.; Bravo-Castillero, J.; Guinovart-Díaz, R.; Camacho-Montes, H.; Sabina, F. Effects of Interface Contacts on the Magneto Electro-elastic Coupling for Fiber Reinforced Composites. *Int. J. Solids Struct.* **2011,** *48,* 1525−1533.

Espinosa-Almeyda, Y.; Rodríguez-Ramos, R.; Guinovart-Díaz, R.; Bravo-Castillero, J.; López-Realpozo, J.; Camacho-Montes, H.; Sabina, F.; Lebon, F. Antiplane Magneto-Electro-Elastic Effective Properties of Three-phase Fiber Composites. *Int. J. Solids Struct.* **2014,** *51,* 3508−3521.

Etier, M.; Schmitz-Antoniak, C.; Salamon, S.; Trivedi, H.; Gao, Y.; Nazrabi, A.; Landers, J.; Gautam, D.; Winterer, M.; Schmitz, D.; et al. Magnetoelectric Coupling on Multiferroic Cobalt Ferrite−Barium Titanate Ceramic Composites with Different Connectivity Schemes. *Acta Mater.* **2015,** *90,* 1−9.

Fetisov, Y. K.; Srinivasan, G. Electric Field Tuning Characteristics of a Ferrite-Piezoelectric Microwave Resonator. *Appl. Phys. Lett.* **2006,** *88,* 143503.

Fuentes-Cobas, L.; Chateigner, D.; Pepponi, G.; Muñoz-Romero, A.; Ramírez-Amparan, G.; Templeton-Olivares, I.; Sánchez-Aroche, D.; Hernández-Montes, J.; De La Mora Núñez, A. M.; López-Carrasco, M. Implementing Graphic Outputs for the Material Properties Open Database (MPOD). *Acta Cryst* **2014,** *70,* C1039.

Fuentes-Cobas, L.; Fuentes-Montero, M. *La relación estructura-simetría-propiedades en cristales y policristales;* Reverté: Spain, 2008.

Fuentes-Cobas, L. E.; Matutes-Aquino, J. A.; Fuentes-Montero, M. E. *Magnetoelectricity* In: *Handbook of Magnetic Materials,* Vol. 19; Elsevier, 2011 (Chapter 3).

Fuentes-Cobas, L. E.; Muñoz-Romero, A.; Montero-Cabrera, M. E.; Fuentes-Montero, L.; Fuentes-Montero, M. E. Predicting the Coupling Properties of Axially-textured Materials. *Materials* **2013,** *6,* 4967−4984.

Fuentes-Montero, L.; Montero-Cabrera, M. E.; Fuentes-Cobas, L. The Software Package ANAELU for X-ray Diffraction Analysis Using Two-dimensional Patterns. *J. Appl. Crystallogr.* **2010,** *44,* 241−246.

Fuentes, L. Magnetic-coupling Properties in Polycrystals. *Textures Microstruct.* **1998,** *30,* 167−190.

Fuentes, L.; García, M.; Bueno, D.; Fuentes, M.; Muñoz, A. Magnetoelectric Effect in $Bi_5Ti_3FeO_{15}$ Ceramics Obtained by Molten Salts Synthesis. *Ferroelectrics* **2006,** *336,* 81−89.

Ghosh, A.; Masud, M. G.; Dey, K.; Chaudhuri, B. Antisymmetric Exchange Interaction, Magnetoelectric and Magnetodielectric Response in Structurally Distorted G-type Antiferromagnetic Perovskite: La 0.9 Gd 0.1 FeO 3. *J. Phys. Chem. Solids* **2014,** *75,* 374−378.

Gražulis, S.; Chateigner, D.; Downs, R. T.; Yokochi, A.; Quirós, M.; Lutterotti, L.; Manakova, E.; Butkus, J.; Moeck, P.; Le Bail, A. Crystallography Open Database−an Open-Access Collection of Crystal Structures. *J. Appl. Crystallogr.* **2009,** *42,* 726−729.

Guduru, R.; Liang, P.; Runowicz, C.; Nair, M.; Atluri, V.; Khizroev, S. Magneto-Electric Nanoparticles to Enable Field-Controlled High-Specificity Drug Delivery to Eradicate Ovarian Cancer Cells. *Sci. Rep.* **2013,** *3,* 2953.

Hall, S. R.; Allen, F. H.; Brown, I. D. The Crystallographic Information File (CIF): A New Standard Archive File for Crystallography. *Acta Crystallogr., Sect. A: Found. Crystallogr.* **1991,** *47,* 655−685.

Hill, R. The Elastic Behaviour of a Crystalline Aggregate. *Proc. Phys. Soc. Sect. A* **1952,** *65,* 349.

Huang, F.; Wang, Z.; Lu, X.; Zhang, J.; Min, K.; Lin, W.; Ti, R.; Xu, T.; He, J.; Yue, C.; et al. Peculiar magnetism of $BiFeO_3$ Nanoparticles with Size Approaching the Period of the Spiral Spin Structure. *Sci. Rep.* **2013,** *3*.

Jaffari, G. H.; Samad, A.; Iqbal, A. M.; Hussain, S.; Mumtaz, A.; Awan, M.; Siddique, M.; Shah, S. I. Effect of A and B-site Substitution with Pb, La and Ti on Phase Stabilization and Multiferroic Properties of BiFeO 3. *J. Alloys Compd.* **2015,** *644,* 893−899.

Kimura, T.; Goto, T.; Shintani, H.; Ishizaka, K.; Arima, T.; Tokura, Y. Magnetic Control of Ferroelectric Polarization. *Nature* **2003,** *426,* 55−58.

Kleemann, W.; Binek, C. *Multiferroic and Magnetoelectric Materials. Magnetic Nanostructures;* Springer, 2013.

Kocks, U. F.; Tomé, C. N.; Wenk, H.-R. *Texture and Anisotropy: Preferred Orientations in Polycrystals and Their Effect on Materials Properties;* Cambridge university press, 2000.

Landau, L. *Electrodynamics of Continuous Media* In: *Course of Theoretical Physics,* Vol. 8; Elsevier, 2009.

Lebensohn, R. A.; Brenner, R.; Castelnau, O.; Rollett, A. D. Orientation Image-Based Micromechanical Modelling of Subgrain Texture Evolution in Polycrystalline Copper. *Acta Mater.* **2008,** *56,* 3914−3926.

Lebeugle, D.; Colson, D.; Forget, A.; Viret, M.; Bataille, A. M.; Gukasov, A. Electric-Field-Induced Spin Flop in ${\mathrm{BiFeO}}_{3}$ Single Crystals at Room Temperature. *Phys. Rev. Lett.* **2008,** *100,* 227602.

Lee, S.; Fernandez-Diaz, M.; Kimura, H.; Noda, Y.; Adroja, D.; Lee, S.; Park, J.; Kiryukhin, V.; Cheong, S.-W.; Mostovoy, M. Negative Magnetostrictive Magnetoelectric Coupling of $BiFeO_3$. *Phys. Rev. B* **2013,** *88,* 060103.

Litvin, D. B.; Janovec, V. Spontaneous Tensor Properties for Multiferroic Phases. *Ferroelectrics* **2014,** *461,* 10−15.

Lu, C.; Hu, W.; Tian, Y.; Wu, T. Multiferroic Oxide Thin Films and Heterostructures. *Appl. Phys. Rev.* **2015,** *2,* 021304.

Lutterotti, L.; Chateigner, D.; Ferrari, S.; Ricote, J. Texture, Residual Stress and Structural Analysis of Thin Films Using a Combined X-ray Analysis. *Thin Solid Films* **2004,** *450,* 34−41.

Ma, J.; Hu, J.; Li, Z.; Nan, C. W. Recent Progress in Multiferroic Magnetoelectric Composites: from Bulk to Thin Films. *Adv. Mater.* **2011,** *23,* 1062−1087.

Marauska, S.; Jahns, R.; Kirchhof, C.; Claus, M.; Quandt, E.; Knöchel, R.; Wagner, B. Highly Sensitive Wafer-level Packaged MEMS Magnetic Field Sensor Based on Magnetoelectric Composites. *Sens. Actuators A Phys.* **2013,** *189,* 321−327.

Marzari, N.; Vanderbilt, D. Maximally Localized Generalized Wannier Functions for Composite Energy Bands. *Phys. Rev. B* **1997,** *56,* 12847.

Masud, M. G.; Dey, K.; Ghosh, A.; Majumdar, S.; Giri, S. Occurrence of Magnetoelectric Effect Correlated to the Dy Order in Dy_2NiMnO_6 Double Perovskite. *J. Appl. Phys.* **2015,** *118,* 064104.

Matsukura, F.; Tokura, Y.; Ohno, H. Control of Magnetism by Electric Fields. *Nat. Nanotechnol.* **2015,** *10,* 209−220.

Matthies, S.; Humbert, M. On the Principle of a Geometric Mean of Even-rank Symmetric Tensors for Textured Polycrystals. *J. Appl. Crystallogr.* **1995,** *28,* 254−266.

Matthies, S.; Vinel, G. W.; Helming, K. *Standard Distributions in Texture Analysis: Maps for the Case of Cubic-Orthorhomic Symmetry;* Akademie-Verlag, 1987.

Moriya, T. Anisotropic Superexchange Interaction and Weak Ferromagnetism. *Phys. Rev.* **1960,** *120,* 91.

Naik, V.; Mahendiran, R. Magnetic and Magnetoelectric Studies in Pure and Cation Doped. *Solid State Commun.* **2009,** *149,* 754−758.

Nair, M.; Guduru, R.; Liang, P.; Hong, J.; Sagar, V.; Khizroev, S. Externally Controlled On-demand Release of Anti-HIV Drug Using Magneto-electric Nanoparticles as Carriers. *Nat. Commun.* **2013,** *4,* 1707.

Newham, R. *Properties of Materials: Anisotropy, Symmetry, Structure;* Oxford University Press: Oxford, 2005.

Nye, J. F. *Physical Properties of Crystals: Their Representation by Tensors and Matrices;* Oxford university press, 1985.

Özgür, Ü.; Alivov, Y.; Morkoç, H. Microwave Ferrites, Part 2: Passive Components and Electrical Tuning. *J. Mater. Sci. Mater. Electron.* **2009,** *20,* 911−952.

Pepponi, G.; Gražulis, S.; Chateigner, D. MPOD: A Material Property Open Database Linked to Structural Information. *Nucl. Instrum. Methods Phys. Res.* **2012,** *284,* 10−14.

Petit, S. Viewpoint: Subtle Atomic Shifts. *Physics* **2013,** *6,* 93.

Purcell, E. M.; Morin, D. J. *Electricity and Magnetism;* Cambridge University Press, 2013.

Ramesh, R. Electric Field Control of Ferromagnetism Using Multi-ferroics: The Bismuth Ferrite Story. *Philos. Trans. R. Soc. Lond. A Math. Phys. Eng. Sci.* **2014,** *372,* 20120437.

Raymond, O.; Ostos, C.; Font, R.; Curiel, M.; Bueno-Baques, D.; Machorro, R.; Mestres, L.; Portelles, J.; Siqueiros, J. M. Multiferroic Properties and Magnetoelectric Coupling in Highly Textured Pb (Fe 0.5 Nb 0.5) O 3 Thin Films Obtained by RF Sputtering. *Acta Mater.* **2014,** *66,* 184−191.

Resta, R. Macroscopic Electric Polarization as a Geometric Quantum Phase. *EPL (Europhys. Lett.)* **1993,** *22,* 133.

Resta, R.; Vanderbilt, D. *Theory of Polarization: A Modern Approach. Physics of Ferroelectrics;* Springer, 2007.

Reuss, A. Berechnung der Fließgrenze von Mischkristallen auf Grund der Plastizitätsbedingung für Einkristalle. *ZAMM-Journal Appl. Math. Mechanics/Zeitschrift für Angewandte Math. and Mech.* **1929,** *9,* 49−58.

Reyes, A.; De La Vega, C.; Fuentes, M. E.; Fuentes, L. $BiFeO_3$: Synchrotron Radiation Structure Refinement and Magnetoelectric Geometry. *J. Eur. Ceram. Soc.* **2007,** *27,* 3709−3711.

Rivera, J.-P. The Linear Magnetoelectric Effect in $LiCoPO_4$ Revisited. *Ferroelectrics* **1994,** *161,* 147−164.

Rivera, J.-P. A Short Review of the Magnetoelectric Effect and Related Experimental Techniques on Single Phase (Multi-) Ferroics. *Eur. Phys. J. B* **2009,** *71,* 299−313.

Rojas-George, G.; Concha-Balderrama, A.; Silva, J.; Fuentes, L.; Reyes-Rojas, A. Elucidating the Real Effect of Ba and Co Doping on the Magnetic and Optical Properties of $BiFeO_3$. *Ceram. Int.* **2015,** *41,* 9140−9145.

Rushchanskii, K. Z.; Kamba, S.; Goian, V.; Vaněk, P.; Savinov, M.; Prokleška, J.; Nuzhnyy, D.; Knížek, K.; Laufek, F.; Eckel, S.; et al. A Multiferroic Material to Search for the Permanent Electric Dipole Moment of the Electron. *Nat. Mater.* **2010,** *9,* 649−654.

Ryu, J. Magnetoelectric Effect in Composites of Magnetostrictive and Piezoelectric Materials. *J. Electroceram.* **2002,** *8,* 13.

Sando, D.; Agbelele, A.; Rahmedov, D.; Liu, J.; Rovillain, P.; Toulouse, C.; Infante, I.; Pyatakov, A.; Fusil, S.; Jacquet, E. Crafting the Magnonic and Spintronic Response of $BiFeO_3$ Films by Epitaxial Strain. *Nat. Mater.* **2013,** *12,* 641−646.

Scott, J. F. Room-temperature Multiferroic Magnetoelectrics. *NPG Asia Mater.* **2013,** *5,* e72.

Schmid, H. Some Symmetry Aspects of Ferroics and Single Phase Multiferroics. *J. Phys. Condens. Matter* **2008,** *20,* 434201.

Schwartz, A. J.; Kumar, M.; Adams, B. L.; Field, D. P. *Electron Backscatter Diffraction in Materials Science;* Springer, 2009.

Sharma, N.; Gaur, A.; Kumar, V.; Kotnala, R. Multiferroicity and Magnetoelectric Coupling in Doped ZnO. *Superlattices Microstruct.* **2014,** *65,* 299−308.

Silva, J.; Reyes, A.; Castañeda, R.; Esparza, H.; Camacho, H.; Matutes, J.; Fuentes, L. Structure and Electromagnetic Properties of Bi1-xYxFe0. 95Mn0. 05O3 (X = 0.05, 0.075 and 0.10). *Ferroelectrics* **2012,** *426,* 103−111.

Silva, J.; Reyes, A.; Esparza, H.; Camacho, H.; Fuentes, L. $BiFeO_3$: A Review on Synthesis, Doping and Crystal Structure. *Integr. Ferroelectr.* **2011,** *126,* 47−59.

Slaughter, J. C.; Dapino, M. J.; Smith, R. C.; Flatau, A. B. Modeling of a Terfenol-D Ultrasonic Transducer. In *Proc. SPIE 3985, Smart Structures and Materials 2000: Smart Structures and Integrated Systems;* 2000; pp 366−377.

Spaldin, N. A. A Beginner's Guide to the Modern Theory of Polarization. *J. Solid State Chem.* **2012,** *195,* 2−10.

Srinivasan, G.; Priya, S.; Sun, N. *Composite Magnetoelectrics. Materials, Structures and Applications;* Elsevier: Cambridge, 2015.

Sui, Y.; Xin, C.; Zhang, X.; Wang, Y.; Wang, Y.; Wang, X.; Liu, Z.; Li, B.; Liu, X. Enhancement of Multiferroic in $BiFeO_3$ by Co Doping. *J. Alloys Compd.* **2015,** *645,* 78−84.

Ti, R.; Huang, F.; Zhu, W.; He, J.; Xu, T.; Yue, C.; Zhao, J.; Lu, X.; Zhu, J. Multiferroic and Dielectric Properties of Bi 4 LaTi 3 FeO 15 Ceramics. *Ceram. Int.* **2015**.

Van Aken, B. B.; Palstra, T. T.; Filippetti, A.; Spaldin, N. A. The Origin of Ferroelectricity in Magnetoelectric $YMnO_3$. *Nat. Mater.* **2004,** *3,* 164−170.

Vanderbilt, D.; King-Smith, R. Electric Polarization as a Bulk Quantity and its Relation to Surface Charge. *Phys. Rev. B* **1993,** *48,* 4442.

Vegte, M. A. V. D. *Competing Interactions in Multiferroics and Low-dimensional Systems;* University of Groningen, 2010. Ph.D. thesis.

Voigt, W. *Lehrbuch der kristallphysik (mit ausschluss der kristalloptik);* Teubner Verlag: Leipzig, 1928.

Wang, X.; Chai, Y.; Zhou, L.; Cao, H.; Cruz, C.-D.; Yang, J.; Dai, J.; Yin, Y.; Yuan, Z.; Zhang, S. Observation of Magnetoelectric Multiferroicity in a Cubic Perovskite System: $LaMn_3Cr_4O_{12}$. *Phys. Rev. Lett.* **2015,** *115,* 087601.

Wang, Y.; Li, J.; Viehland, D. Magnetoelectrics for Magnetic Sensor Applications: Status, Challenges and Perspectives. *Mater. Today* **2014,** *17,* 269−275.

Welzel, U.; Ligot, J.; Lamparter, P.; Vermeulen, A.; Mittemeijer, E. Stress Analysis of Polycrystalline Thin Films and Surface Regions by X-ray Diffraction. *J. Appl. Crystallogr.* **2005,** *38,* 1−29.

Wenk, H.; Van Houtte, P. Texture and Anisotropy. *Rep. Prog. Phys.* **2004,** *67,* 1367.

Wiegelmann, H.; Jansen, A.; Wyder, P.; Rivera, J.-P.; Schmid, H. Magnetoelectric Effect of Cr_2O_3 in Strong Static Magnetic Fields. *Ferroelectrics* **1994,** *162,* 141−146.

Yáñez-Vilar, S.; Mun, E. D.; Zapf, V. S.; Ueland, B. G.; Gardner, J. S.; Thompson, J. D.; Singleton, J.; Sánchez-Andújar, M.; Mira, J.; Biskup, N.; et al. Multiferroic Behavior in the Double-perovskite Lu_2MnCoO_6. *Phys. Rev. B* **2011,** *84*.

Ye, M.; Vanderbilt, D. Magnetic Charge and Magnetoelectricity in Hexagonal Manganites and Ferrites. In *APS March Meeting Abstracts;* 2015; p 6002.

Yi, W.; Princep, A. J.; Guo, Y.; Johnson, R. D.; Khalyavin, D.; Manuel, P.; Senyshyn, A.; Presniakov, I. A.; Sobolev, A. V.; Matsushita, Y. Sc_2NiMnO_6: A Double-perovskite with a Magnetodielectric Response Driven by Multiple Magnetic Orders. *Inorg. Chem.* **2015,** *54* (16), 8012−8021.

Yoshinori, T.; Shinichiro, S.; Naoto, N. Multiferroics of Spin Origin. *Rep. Prog. Phys.* **2014,** *77,* 076501.

Zhang, D.; Yang, S.; Chen, Z.; Feng, L.; Huang, W.; Zhao, W.; Dong, S.; Li, X. Multiferroic Properties of Neodymium and Cobalt Co-doped Four-layer Aurivillius Compounds. In *Magnetics Conference (INTERMAG), 2015 IEEE;* IEEE, 2015; p 1.

Zhang, J.; Gao, Y. Effects of Hysteresis and Temperature on Magnetoelectric Effect in Giant Magnetostrictive/piezoelectric Composites. *Int. J. Solids Struct.* **2015,** *69,* 291−304.

Zhou, Y.; Priya, S. Magnetoelectric Current Sensor Chapter 8. In *Composite Magnetoelectrics: Materials, Structures, and Applications;* Srinivas, A., Priya, S., Sun, N., Eds.; Elsevier: Cambridge, 2015.